Université Paris-Sud XI
Laboratoire de Physique des Gaz et des Plasmas
Orsay, France
&
Masaryk University in Brno
Department of Physical Electronics
Brno, Czech Republic

Plasma diagnostics focused on new magnetron sputtering devices for thin film deposition

PhD Thesis

Petr Vašina

Defended 4. 11. 2005 at Orsay, members of commission

Mrs	C. Boisse - Laporte	Supervisor
Mr	M. Ganciu	Examinator
Mr	J. Janča	Supervisor
Mrs	A.-M. Pointu	President
Mr	A. Ricard	Reporter
Mr	J. Vlček	Reporter

Acknowledgement

Abstract

You are about to start reading my PhD thesis entitled Plasma diagnostics focused on new magnetron sputtering devices for thin film deposition. It deals with processes concerning sputtered particles in a deposition reactor. A magnetron cathode is sputtered and acts as a source of metal particles. These particles are ionized either by a microwave plasma located between the magnetron cathode and the substrate or by a magnetized plasma itself working in preionized high power pulse regime. To describe and understand these two different concepts of sputtered particles ionization, different approaches to plasma diagnostics are needed. The microwave assisted PVD reactor consists of a magnetron cathode excited by a direct current and two microwaves antennas located perpendicularly to magnetron substrate holder axis. While a sputtered particle diffuses toward the substrate, it can be ionized anywhere between the magnetron cathode and the substrate. In this case, it is suitable to perform the spatially resolved plasma diagnostics. The role of various elementary processes which may influence the densities of species in magnetron and microwave plasma are discussed. Particular attention is given to the estimation and the role of gas temperature. In the high power pulsed PVD, sputtered particles are ionized in the magnetized region and after that, they can leave it and continue towards the substrate. These processes are time dependent and it is suitable in this case to perform time resolved measurements. Plasma dynamics, time evolution of plasma compositions and particularly the extremely fast transition to stable self-sputtering regime is discussed. Simultaneously with the creation processes of ions, their transport was studied too. Because we intended to work in a reactive magnetron sputtering too, I spent a time studying the plasma ignited by surfatron in nitrogen gas, oxygen gas and their mixtures. We started with moderate pressure microwave discharge. To detect the reactive radicals, such as N and O atoms, electron paramagnetic resonance and NO titration was used. The second mentioned method was advanced and permits now to obtain simultaneously N and O atom density without a calibration. My thesis consists of an introduction, 5 chapters and a summary. These 5 chapters are independent and can be red in any order. However, if you are not interested only in a particular topic, I advice you to follow the order, which I proposed.

I wish you a pleasant reading.

Petr Vašina

Contents

Chapter 1

Introduction

In numerous technological applications, it is necessary to perform high quality thin film deposition on certain objects. As an example, microelectronics technology is based on a precise and progressive thin film deposition. Various function structures are created within the silicon surface by piling dielectric and conductive thin layers. These function structures are contacted together locally to form specific function (memory cell, logic gates) and then interconnected together globally to form a fully functioning integrated circuit on the chip. Shrinking of critical dimensions of components and rapidly increasing number of devices per chip each year is astounding.

Magnetron sputtering falls to a group of Physical Vapour Deposition techniques (PVD), in which films are deposited from single atoms or very small clusters and any reactions that occur (such as oxidation or nitridization) occur at the film surface. This differs PVD from Chemical Vapour Deposition (CVD) techniques, in which molecular species in the gas phase chemically react at a film surface, resulting in the formation of a condensed film as well as the emission of volatile by-products. In magnetron sputtering, a magnetron cathode is sputtered and acts as a source of atoms which condensate on the wafer and form growing film.

Ionized physical vapour deposition (IPVD) is an advance in PVD technology that achieves directional deposition of metals by ionizing the sputtered atoms and collimating these ions with a plasma sheath adjacent to the wafer. Moreover, IPVD makes possible to form films under new physical condition, particularly at high ion flux on the wafer. Ion assisted grow of thin films usually improves film density, mechanical properties etc.

Sputtered particles are usually ionized by a high electron density, inert gas plasma between the target and the wafer. This plasma is mainly inductively coupled plasma created by a radio frequency coil introduced to the deposition reactor. A promising pulsed IPVD technique was developed in 1999, which combines a

powerful power supplies with a conventional planar magnetrons. For a short time (some tens of microseconds) a very dense plasma is sustained near the magnetron cathode, which induces simultaneous target sputtering and efficient ionization of sputtered vapour. The general overview of the magnetron sputtering physics, principles of PVD and IPVD techniques can be found in chapter 2 of my thesis.

My thesis deals with a characterisation of two different concepts of IPVD. Sputtered particles are ionized either by a microwave plasma located between the magnetron cathode and the substrate or by the magnetized plasma itself working in preionized high power pulse regime. The differences between our systems and other IPVD reactors described in literature are following. In the first system, two microwaves antennas are used instead of the RF coil to create the ionizing plasma between the magnetron cathode and substrate. In the second system, high power pulsed sputtering was intentionally preionized by low-current DC preionization.

To describe and understand these two different concepts of sputtered particles ionization, different approaches to plasma diagnostics are needed. In microwave assisted PVD, a sputtered particle diffusing toward the substrate can be ionized anywhere between the magnetron cathode and the substrate. In this case, it is suitable to perform the spatially resolved plasma diagnostics. Results of plasma diagnostics in microwave assisted PVD reactor are shown and discussed in chapter 3. In the high power pulsed PVD, sputtered particles are ionized in the magnetized region which they can leave and continue towards the substrate. In this case, magnetized plasma ensures simultaneously sputtering of neutral species and their ionization. This processes are time dependent and it is suitable in this case to perform time resolved measurements. Study of preionized high power pulse magnetron plasma, time evolution of plasma composition and discharge dynamics is a subject of chapter 4. Transport of sputtered particles created during the pulse and a test of industrial potential of our system in trench filling is shown in chapter 5.

Because we intended to work in a reactive magnetron sputtering too, I spent my time studying the plasma ignited in nitrogen, oxygen and their mixtures. We started with moderate pressure microwave discharge and this study was very interesting. To detect the reactive radicals, such as N and O atoms, electron paramagnetic resonance and NO titration was used. The second mentioned method was advanced and permits now to obtain simultaneously N and O atom density without a calibration. More details can be found in chapter 6 of my thesis.

Chapter 2

Physics of magnetron sputtering

2.1   Introduction

The physical process that we now call sputtering was first reported in 1852 by
Sir William Robert Grove [1], who described the effect as cathode disintegration.
Grove's apparatus utilized a cathode made of silver-coated copper, but his manu-
ally pumped vacuum was insufficient that the world's first sputter deposited film
was probably not silver, but silver oxide.

In 1921, Sir. John Thomson renamed this phenomenon which refers to the
rapid ejection of small particles from a cathode as 'frying bacon splutters fat'
to spluttering. In a scientific paper two years later, Thomson dropped 'l' from
spluttering in favour of a less common variation and it has been sputtering even
since.

Subsequent investigation led to an understanding of the basic physics of the
sputtering and resulted in a variety of industrial coating application as metal films
for mirror (1875) or gold film deposition on wax photograph masters (1930).
When sputtering was nearly 100 years old, the first microelectronics device - the
solid state transistor - was demonstrated publicly in 1948 and since that time thin
film deposited by sputtering - i.e. by physical vapour deposition (PVD) has be-
come an essential part of integrated circuit fabrication technology.

In the 1970s, sputtering began to displace hot filament evaporation because
DC magnetrons were capable to deposit high quality aluminium alloys at de-
posited rates and costs comparable to evaporation together with better control of
film composition and better step coverage. There are number of reasons why PVD
has been so successful for wide range of industrial application. Sputtering can be
used to deposit all of conducting films including low melting point metals such
as Al (t_{melt}=660 $^\circ$C) and refractory metals as Ti (t_{melt}=1670 $^\circ$C). Sputtering of
important multicomponent alloys can be deposited from a single alloy sputter tar-

get, which was problematic with evaporation since the deposition rate of the alloy constituent depends on their individual vapour pressures. In the reactive regime, oxides and nitrides can be sputtered too. Sputtering is done from an extended area target and not from a point source as in evaporation which is another reason for the success of PVD keeping global film uniformity from properly designed magnetrons. Since PVD utilises non-toxic targets and low pressure of inert gas, PVD satisfies increasing environmental demands about the use of hazardous materials.

In this chapter, a general overview of basic physical principles of sputtering is given. A possibility to increase process efficiency by using a magnetron configuration will be shown. Sputtering is predominantly a neutral emission process. Ionizing the sputtered particle flux makes possible to form films under new physical conditions, such as enhanced ion assisted grown of films and deposition directionality. Sputtered particle flux can be ionized by a secondary plasma located between the magnetron target and the substrate of directly by a magnetized plasma operated in high power pulsed regime. Both so called IPVD processes are explained without great details. The following interesting book [2] and these great review articles [3] and [4] have been used as a very helpful base for this chapter.

2.2   Physics of Sputtering

2.2.1   Physical vapour deposition, sputter yield

Vacuum based deposition technologies fall into two basic categories: physical vapour deposition (PVD) and chemical vapour deposition (CVD). The PVD techniques include physical sputtering, thermal evaporation and arc-based deposition, which are all generally atomic in nature. Films are deposited from single atoms or small clusters and any reaction that occur (such as oxidation or nitridization) occur at the film surface. This differ PVD from CVD techniques, in which molecular species in the gas phase chemically react at a film surface, resulting in the formation of a condensed film as well as the emission of volatile by-products.

Sputtering is relatively simple process in which an energetic particle bombards a target surface with sufficient energy to eject one or more atoms from the target. The most commonly used incident species are inert gas ions (e.g. Ar^+, Kr^+, Xe^+), but sputtering can also result from the bombardment of other energetic ions, neutrals, electrons and even photons. In general, the physical effect caused by bombardment with a neutral or an ion of the same species and energy will be identical. The ion is usually neutralized by pulling an electron from the near-surface region just prior to impact, and so it impacts the surface as a neutral. Because it is quite easy to generate large fluxes of ions at controlled energies all applications of sputtering use ions as the bombarding particles. The sputtering
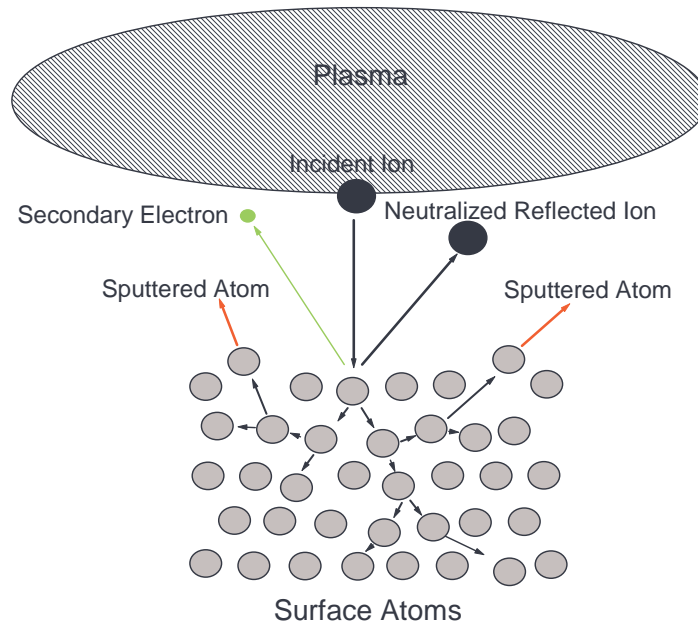
Figure 2.1: Schematic illustration of physical sputtering process

yield γ is simply defined as the ratio of the number of emitted to the number of bombarding particles.

$$\gamma = \frac{\text{number of ejected particles}}{\text{number of incident particles}} \tag{2.1}$$

2.2.2 From sputtering to implanting

The sputtering process is one of relatively violent. Collisions, first between the incident energetic particle and one or two substrate atoms, and then subsequent collisions between multiple atoms as the part of incident energy and momentum are distributed among many atoms. Depending on the kinetic energy E of the incident ion, four different physical results can occur.

1. Low energy (E < 20 - 50 eV) This region is known classically and somewhat inaccurately as the sub threshold region. In this regime, it was thought that an incident ion had too little energy to dislodge and to eject a target atom and that the resultant yield was assumed to be zero until a threshold of about 4 times the binding energy of the target material. Experimentally, in high density plasma, such as those formed using ECR techniques, sputtering and film deposition at ion energies of bellow 15 eV are routinely observed. The required sputtering yield is in 10^{-6} range which contradicts the threshold theories and show dramatic fall-off in the
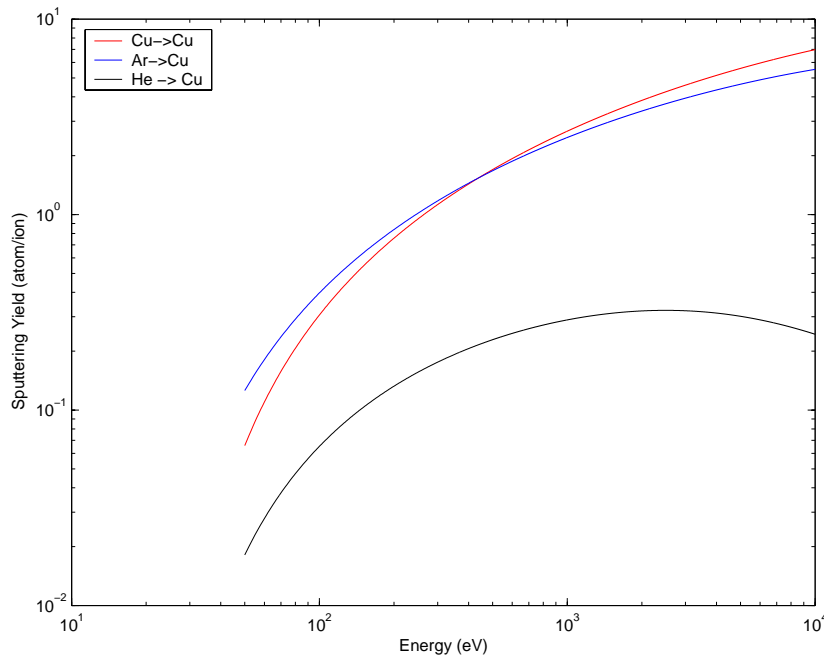
Figure 2.2: Sputter yield as a function of ion energy for Ar^+, Cu^+ and He^+ bombarding the Cu target

yield as the ion energy decreases. However, since the ion current in ECR tools may be many tens of amperes even these very tiny yields can be quite significant. 2. Moderate energy (50 eV < E < 1 keV) This range, sometimes known as the knock-on regime, covers most of the practical range of energy used in PVD. In this range, the incident ion impact a target atom, which recoils and strikes one or more atoms, which each recoil and the process continues much like in Figure 2.1. This is difficult process to predict and measure because the sequence of collisions will be completely different for each bombarding particle because each particle will hit in a different place with regard to the location of the surrounding atoms. This process must be evaluated practically by simply looking at the average of a large number of impacting particles. For such case, using of previously defined sputtering yield is very helpful. Sputtering yield depends strongly on the incident particle's mass and kinetic energy as well as the substrate mass and orientation. Sputtering yield as a function of ion energy for Ar^+, Cu^+ and He^+ bombarding the Cu target is presented in Figure 2.2. It was shown that unless the temperature of target was very close to the melting point, target temperature is not relevant to sputtering process. It would not make sense that energies on the thermal scale (0.1 eV) would have influence on sputtering events, which contains energies in the hundreds of eV.

3. High energy (1 keV $<$ E $<$ 50 keV) This region, which is not relevant to PVD processes, is nevertheless the more well understood region. At these energies, the incident ion causes a dense cascade of secondary particles after the impact. Within this cascade, almost all of bonds between the atoms are broken and the region can by treated with a statistical mechanic-like approach.

4. Very high energy (E $>$ 50 eV) At these high energies, the incident ion can penetrate down into the target lattice many layers through before causing a significant number of collision. As a result, the affected volume is well below the surface and only few atoms can by emitted. The incident ion is effectively implanted into the bulk of target changing the electrical properties of the material, which is quite important for atom implanting into semiconductor, but it is mostly irrelevant for physical sputtering.

2.2.3 Sputtering, self-sputtering and evaporation

Since sputtering is mostly a momentum and energy transfer process between the incident particle and the target atoms, the particular species used are very important. The sputter yield is different for different target materials using the same ion species and energy. There are two reasons for these differences. First, the binding energy will be different for each target material. There is general trend toward higher sputtering yield for materials with lower binding energy, and there is a general correlation between low melting point and low binding energy. However, sputtering is not a thermal process, so these correlations should not be taken too strongly. A second reason for differences in yields is the efficiency of the momentum transfer process between the incident ion and target atom. It has a maximum value for two equal mass species, which implies that the highest sputtering yield should be for cases of target being bombarded by an ion of the same species. This situation in named self-sputtering. An example, sputtering yield as a function of ion energy for Ar^+, Cu^+ and He^+ bombarding the Cu target is shown in Figure 2.2. It suggest that the sputtering process will be rather inefficient and the yield relatively low for cases of a large differences between the incident and target masses.

Probably the most interesting aspect of copper or silver PVD is the possibility of using self-sputtering to completely avoid the argon working gas and associated gas-atom scattering collisions and Ar incorporation in to the growing film.

The term self-sputtering describes the sputtering of metal target using ions of the same element. A fraction of the ionized sputtered atoms arrives at the sheath edge near the substrate, but another fraction can be redirected and diffuse back to the sheath of the target. Those ions will be accelerated in the sheath of the magnetron target and cause sputtering of more target material. If the sputtering yield exceeds unity, sustained self-sputtering is possible, implying that the gas
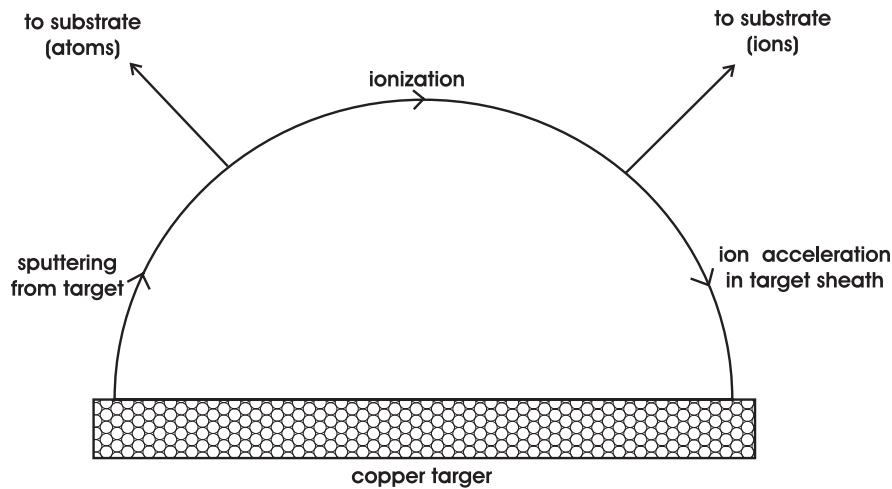
Figure 2.3: Schematic picture of the sustained self-sputtering cycle

flow could be switched off after the process is set in. The buffer gas only initiates the process which continues itself. The condition of sustained self-sputtering can be written as [5]

$$\alpha\beta\gamma_s > 1 \qquad\qquad (2.2)$$

where α is the probability that a sputtered atom will be ionized, β is the probability, that the ionized atom is redirected to the cathode and γ_s is the self-sputtering yield. The whole cycle is schematically shown in Figure 2.3. Because $\alpha < 1$ and $\beta < 1$, it is clear that the sustained self-sputtering is achieved only for materials with $\gamma_s > 1$.

Sputtering differs from evaporation in that the atoms are physically ejected from the target surface and such can have significantly more kinetic energy. An example of this, Cu atoms evaporated at 1500 K leave the surface with velocity describes by very narrow distribution function with maximum around 1 km/s. However Cu atoms sputtered by 500 eV Ar ions have much more broader velocity distribution with maximum around 5 km/s. The shape of the distribution differs for each ion-target system but is only slightly dependent on the incident ion kinetic energy. While the sputtering of small clusters of atoms is relatively rare, such clusters should be expected to follow nominally similar emission characteristics in their energy spectrum as single atoms, perhaps adjusted for the larger mass. More important than the exact distribution is the avarage kinetic energy of emitted atoms. This is a major component of the net energy arriving at the film surface during deposition.

There is another aspects of sputtering that may lead to significant effects on the film deposition - reflected, energetic neutrals. Reflected, energetic neutrals are the result of energetic ion bombardment of the target. There is some probability
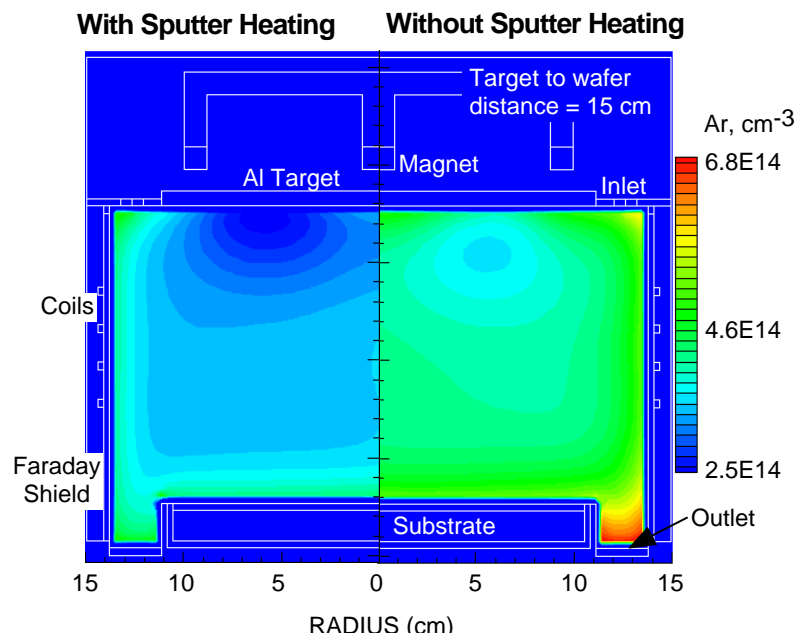
Figure 2.4: Example of the gas rarefaction due to sputter heating, simulation taken from [9] was performed for 1 kW of magnetron power and 4 Pa of Ar buffer gas pressure

that shortly before the impact neutralized ion will be reflected by the surface. As neutral, it is unaffected by sheath. Usually reflected neutral can carry significant kinetic energy, often in the order of tens percent of the incident ion energy and can deposit considerable energy to the film surface and influence physical properties as the film microstructure and stress [6, 7].

2.2.4 Ballistic and diffusive transport, gas rarefaction

Sputtered atoms must travel some distance before they can impact a sample surface to form a growing film. At low pressures, typically below 0.1 Pa, the sputtered atoms travel with few if any collision. This can be described as ballistic or collision-free transport. Ballistic transport is directional, atoms arrive at the film surface with a angular distribution function and an energy originated from the sputtering process. They can be deposited in the top layer or two of the film surface and form defects. As the pressure is increased, it becomes more likely that a sputtered atom may have a gas-phase collision with a background gas atom during transport. This starts to become significant at pressures above 1 Pa. In these conditions, significant kinetic energy of the sputtered atom can be shared with the gas atoms, resulting in both cooling of the sputtered atom and heating of

the background gas. In addition since the momentum and energy transfer cross-sections are strongly energy dependent [8], as the sputtered atom slows down due to collisions, it becomes larger. Sputtered atoms are after first collision quickly thermalized and undergo diffusive transport.

Thermalized deposition can be much different from ballistic deposition because the film grows from atoms with almost no kinetic energy. In parallel to the cooling of sputtered atoms, the gas temperature can increase significantly. Since sputtering chambers are fairly open and have only modest gas flow, significant gas heating results in a local rarefaction of the gas density, as the hot gas atoms leave the near-target region faster than cooler gas atoms arrive from a perimeter. Example of calculated spatial distribution of Ar atoms in deposition reactor for two cases, sputter heating is and is not taken into account is presented in Figure 2.4. Simulation was performed for 1 kW of magnetron power and 4 Pa of Ar buffer gas pressure. The minimum Ar density decreases by 30 percent and occurs below target due to gas rarefaction [9].

Gas rarefaction effects were first observed as the sputtering wind by [10]. Generally gas rarefaction increases with magnetron power, sputtering yield or collision cross section between buffer gas and sputtered atom.

Gas rarefaction may be important in scaling issues, in that high-rate sputtering and as a result more rarefaction may have similar characteristics to low pressure sputtering. This effect will also affect reactive sputtering due to unequal cross section for collisions like sputtered atom - buffer gas atom, sputtered atom - reactive gas molecule, sputtered atom - reactive atom [11].

2.3   The Planar Magnetron

2.3.1   Plasma confinement by magnetic field

Magnetron-based sputter tools deposit thin films at much higher rates than diodes and operate at lower pressures, where gas-phase scattering and gas-phase impurities are minimal. DC magnetron is basically a magnetically enhanced diode in which the spatial relationship of electric and magnetic field is engineered to confirm secondary electrons produced by ions bombardment of the target. Restricting these electrons to remain close to the target surface increases their probability of ionizing the working gas, which results in a more intense plasma discharge that can be sustained at a lower pressure. Since the ions are heavier than electrons, they are not affected by the confining magnetic field and may sputter much as in a diode type configuration.

The electron confinement is based on the Lorentz force given by the vector cress product of two field $\vec{E}$ and $\vec{B}$. Since $\vec{E}$ is perpendicular to the target surface,
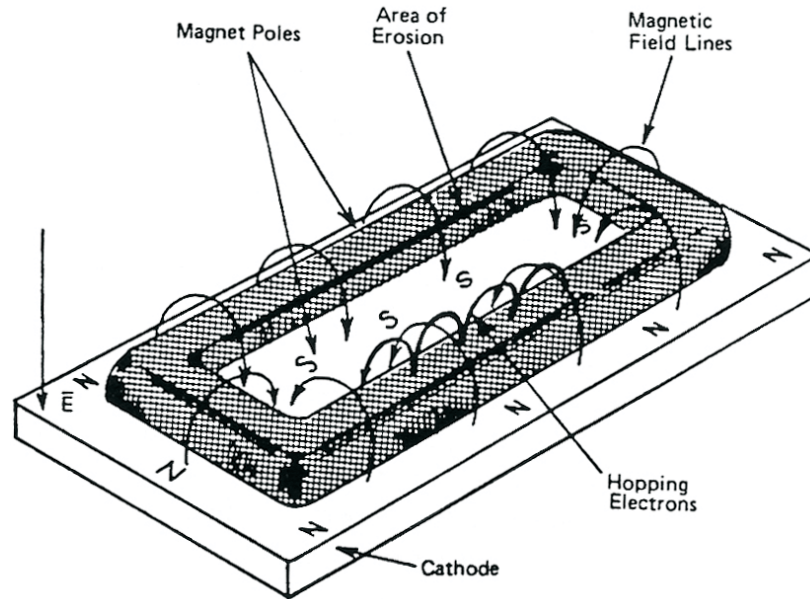
Figure 2.5: An example of rectangular planar balance magnetron configuration.

application of a $\vec{B}$ field tangential to the surface gives the electron a component of velocity parallel to the target. Forcing the electrons in a plasma to move in helical path results in a great increase in a probability that an electron will have a collision with a gas atom, leading to either exciting or ionizing the atom before being scattered out of the plasma region. This effect can be used to form a very dense, low-impedance plasma. A single electron from the target can generate at least 10 electron-ion pairs in the volume of magnetized plasma.

The formation of the closed-loop path for the $\vec{E} \times \vec{B}$ drifting secondary electrons is what defines a magnetron. The simplest geometrical design is circular planar magnetron. As the example of the trapping efficiency of the 15 cm cathode, it was shown that generally the electrons can be considered to go around the $\vec{E} \times \vec{B}$ loop from 3 to 8 times before they are lost to the walls of the system. The circular planar magnetron is the most widely used example. Since the overall requirement is simply that the $\vec{E} \times \vec{B}$ drift path form, there are many other geometrical perturbation. A common example is the rectangular planar magnetron shown in Figure 2.5. This geometry is similar to the circular planar one, but is simply stretched in one direction, forming an $\vec{E} \times \vec{B}$ drift path somewhat like a racetrack oval. Dimensionally, there is no real limit to the length of the rectangular cathode, and sources have been constructed several meters in length for the systems, where samples pass by the long sides of the cathode.
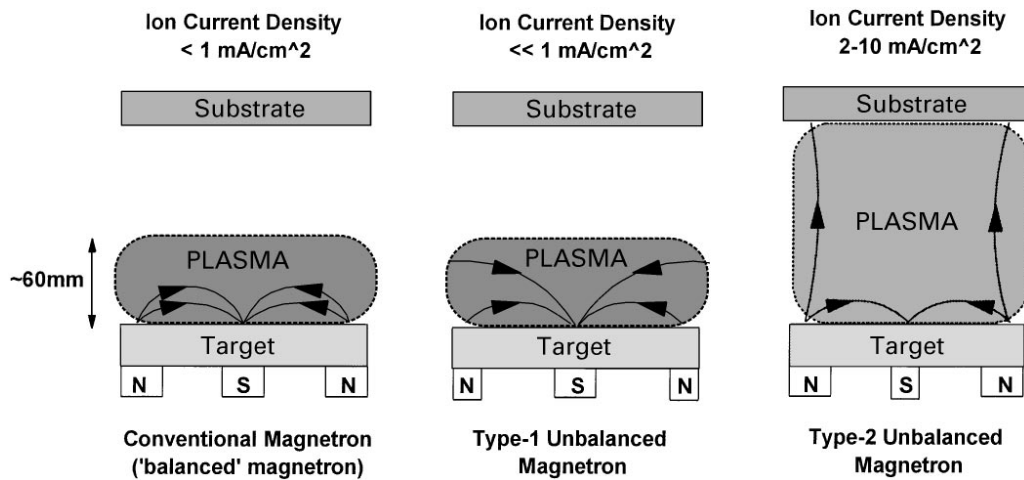
Figure 2.6: Schematic representation of the plasma confinement observed in conventional and unbalanced magnetrons [3].

2.3.2 Balanced and unbalanced magnetron

In the conventional balanced magnetrons the plasma is strongly confined to the target region. A region of dense plasma typically does not extend more than few centimetres from the target. Films grown on substrates positioned within this region will be subjected to strong ion bombardment which can strongly influence the structure and properties of the growing film. Substrates placed outside this region will lie in the area of low plasma density. Consequently, the ion substrate current is generally insufficient to modify the structure of the film. The energy of the bombarding ions can be increased by increasing the negative bias applied to the surface, however, this leads to defects in the film and increased film stress. To deposit dense films without introducing excessive stresses, a high flux of relatively low energy ions is generally preferred. These condition are readily provided by unbalanced magnetrons, ionized physical vapour deposition (IPVD) techniques using a secondary plasma to ionize the sputtered particles and recently by high power pulsed magnetron sputtering.

In an unbalanced magnetron the outer ring of magnets is strengthened (or weakened) relative to the central pole. Schematic representation of the plasma confinement observed in conventional and unbalanced magnetrons is presented in Figure 2.6. In the case of unbalanced magnetron, not all the field lines are closed between the central and outer poles in the magnetron, but some are directed toward the substrate and some secondary electrons are able to follow these field line. Consequently, the plasma is no longer strongly confined to the target region, but is allowed to flow out toward the substrate. Thus relatively high ion current
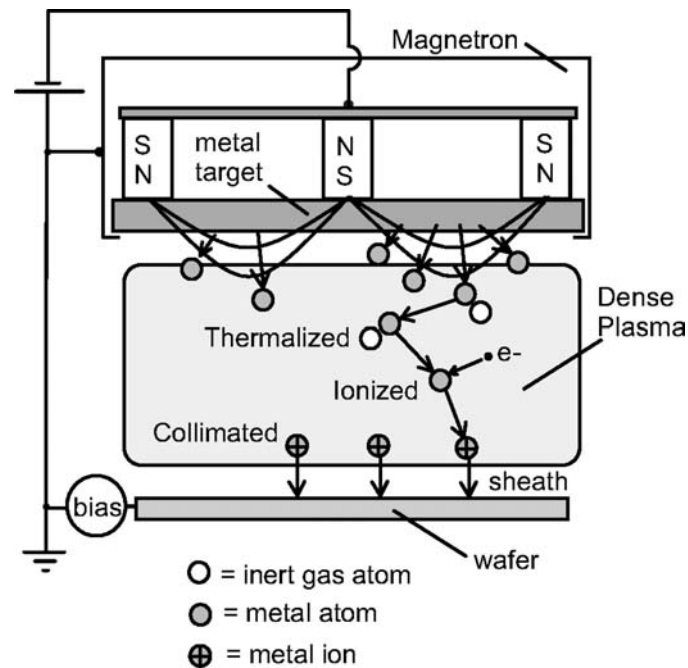
Figure 2.7: In a typical IPVD reactor metal atoms are sputtered into a high density plasma. Once thermalized, the atoms are ionized and diffuse to the wafer region where they are directionally deposited. Picture taken from [13].

can be extracted from the plasma without the need to externally bias the substrate. By unbalanced magnetron, substrate ion current densities approximately an order of magnitude higher than for a conventional balanced magnetron can be routinely generated. Unlike other ion-plating processes, in unbalanced magnetrons the ion to neutral atom ratio at the substrate remains almost constant with increasing deposition rate [12], which is almost directly proportional to target current.

2.4 Ionized Physical Vapour Deposition

2.4.1 Idea and basic principles of IPVD

Physical sputtering is predominantly a neutral atom emission process. The filtering techniques such as collimated sputtering are all subtractive: atom which are not moving in the correct trajectory are trapped on other surfaces, either the chamber wall or the sidewalls of the collimator. Since the sputtered atoms are neutrals, it is not possible to redirect their trajectory once they are ejected from the cathode.

Ionized physical vapour deposition (IPVD) is a advance in PVD technology that achieves directional deposition of metal by ionizing the sputtered or evapo-
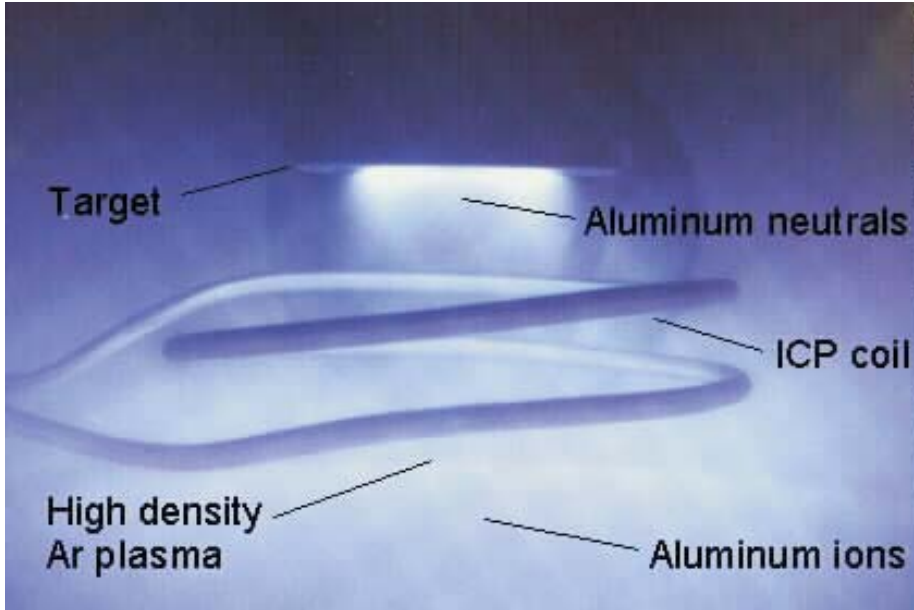
Figure 2.8: The photo shows a IPVD system in operation. The blue glow is an inductively coupled plasma that is excited by a coil antenna. Aluminium atoms are sputtered from target at the top of the photo and then ionized as they move toward the lower part of plasma. Picture taken from [13].

rated metal atoms and collimating these ions with the plasma sheath adjacent to the wafer as shown schematically in Figure 2.7. A high electron density, inert gas plasma between the target and the wafer is needed to ionize the sputtered metal vapour in typical IPVD reactor. Strong ionization of the metal occurs since the electron temperature depends primarily on the ionization potential of the inert gas (15.7 eV for argon) which is much greater than for metals (6.0 and 7.7 eV for Al and Cu). The plasma source is commonly an electron cyclotron resonance plasma or inductively coupled plasma. An example of IPVD systems in operation is shown in Figure 2.8. In the Figure 2.9, there are three photos showing the circular magnetron in operation (top left photo), a RF plasma created by an internal coil in an IPVD reactor (top right photo) and the circular magnetron assisted by the RF plasma (bottom photo). These photos show the IPVD reactor, whose study is a PhD project of my colleague from LPGP Mr. J-C. Imbert.

The average distance that a sputtered neutral will travel before being ionized dictates the design of IPVD reactor. Simple analysis of a sputtered neutral going through a high density plasma gives the ionization mean free path

$$\lambda_{iz} = \frac{v_s}{K_i n_e} \qquad (2.3)$$
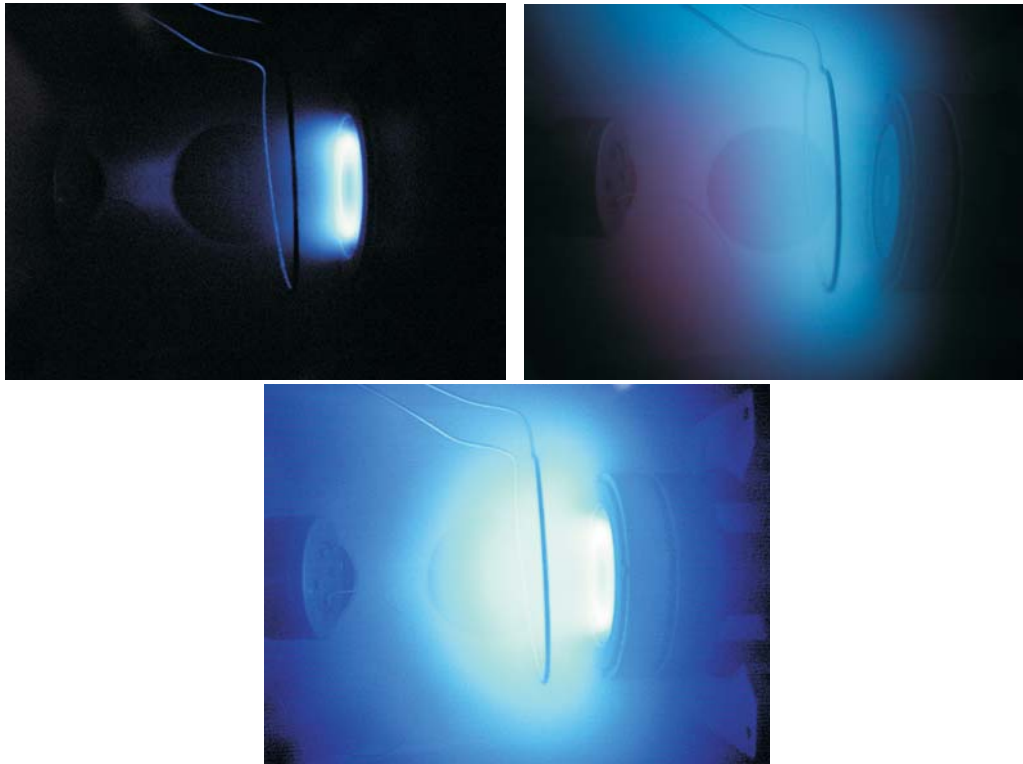
Figure 2.9: Examples of a circular magnetron in operation (top left photo), a RF plasma created by an internal coil in an IPVD reactor (top right photo) and the circular magnetron assisted by the RF plasma (bottom photo).

where v_s is the velocity of the sputtered neutral, K_i is ionization rate constant and n_e is plasma density. Atoms sputtered from a target exhibit a Thomson distribution where the most probable energy is about one half of the surface binding energy. As an example, aluminium atoms are sputtered with energy ~ 1.5 eV and therefore λ_{iz} is ~ 60 cm for typical Ar plasma where $T_e \sim 3$ eV and $n_e \sim 10^{11} \text{cm}^{-3}$. This analysis suggests two methods of generating a highly ionized flux. First, if the inert gas pressure is quite low, the target to substrate distance must be quite long. The second alternative is to increase the pressure such that the sputtered atoms are thermalized by collisions with the inert background gas. If the metal is thermalized, it goes through the plasma much slowly and the ionization path length decreases to about 10 cm. The second method is more convenient because shorter plasma needs less energy to be sustained and big experimental set-ups are more expensive, difficult to pump etc. Schema of a typical IPVD processes: sputtering, thermalization, ionization and collimation is shown in Figure 2.7.

The film coverage of trench and via structures used in microelectronic appli-

cation depends on many factors including resputtering of the surface by ions, re-deposition of resputtered surface material, mobility of surface atoms but the most obvious factor is the fractional ionization of the metal flux incident on the wafer. Since metal ions are accelerated to the Bohm velocity by the plasma presheath, the ion flux at the wafer is

$$\Gamma_i = 0.61[M^+]\sqrt{\frac{kT_e}{m_i}}, \tag{2.4}$$

where $[M^+]$ is the metal ion density, m_i is the ion mass and T_e is the electron temperature. In contrast, the flux of thermalized neutral metal atoms is

$$\Gamma_n = \frac{1}{4}[M]v_{th}, \quad v_{th} = \sqrt{\frac{8kT_{gas}}{\pi m}}, \tag{2.5}$$

where $[M]$ is the metal neutral atom density, m is the atom mass and T_{gas} is the buffer gas temperature. Since $T_e \gg T_{gas}$, the ionized fraction of sputtered particle flux to a wafer is much larger than the ionized fraction of sputtered particle density in the plasma. For example, if metal ionization degree in the plasma is 0.3, the fraction of ionized metal flux is about 0.8. This means that it is not necessary to completely ionize the sputtered metal to create a highly ionized flux to the wafer. To understand and optimise the IPVD method, it is necessary to characterize the degree of metal ionization and understand the ionization channels in the plasma.

The global zero-dimensional model was developed by [4]. It assumes that the sputtered metal is thermalized by collisions with the argon background gas. The three most important collisions responsible for the generation of metal ions in an secondary plasma are electron impact ionization of the metal neutral in the ground state, electron impact ionization of the metal neutral in the excited state, and Penning ionization by collision of metal atom with electronically excited buffer gas atom. Corresponding rate constant are K_i, K_i^* K_P for electron impact collisions and Penning ionization.

For the typical gas pressure of few Pa, the main loss mechanism of metal ions is ambipolar diffusion with the characteristic time constant τ_i depending on the chamber dimensions and the mobility of metal ion.

Assuming that the rates for loss and creation of metal ions equal, the metal ion fraction in plasma (e. g. ionization degree of sputtered metallic species) can be written in following form

$$\frac{[M^+]}{[M] + [M^+]} = \frac{(K_i + K_P K_e \tau[Ar])\tau_i[e]}{1 + K_i + K_P K_e \tau[Ar])\tau_i[e]}. \tag{2.6}$$

where $[M^+]$ is metal ion density, $[M]$ is metal atom density, $[Ar]$ is density of buffer gas, K_e is rate constant for excitation of Ar metastable from Ar ground state
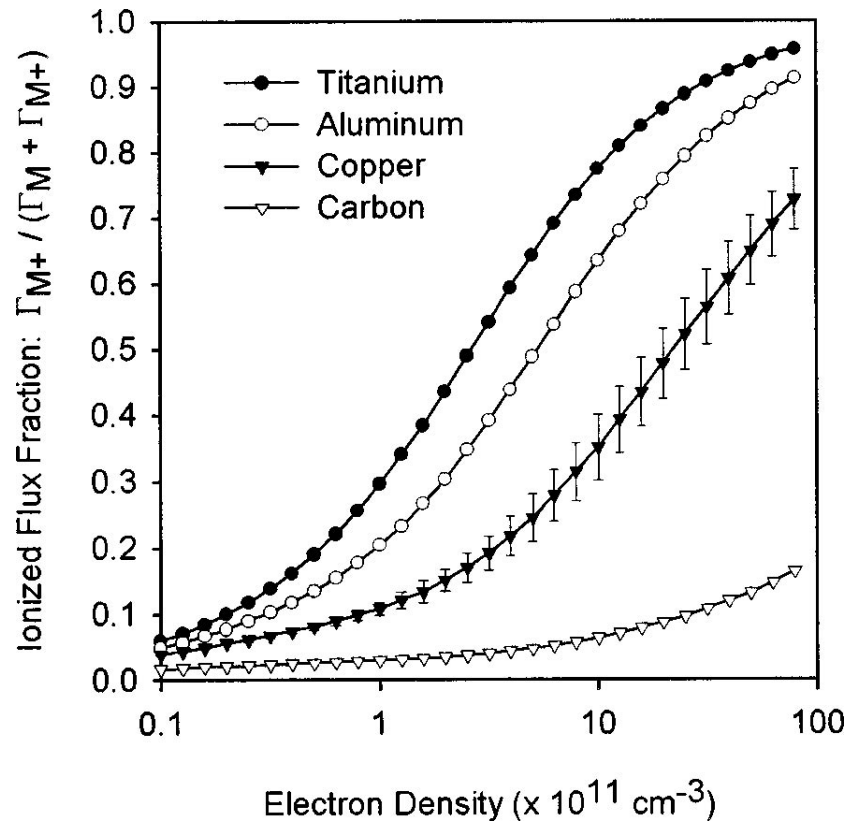
Figure 2.10: Comparison of the modelled ionized flux fraction for several metals. Metals with a large ionization cross section, low ionization potential, and low ion mobility are the most highly ionized. Picture taken from [4].

and τ is loss rate of metastable argon atoms. For detailed step by step derivation of the Equation 2.6 see [4]

Figure 2.10 shows the modelled ionization of various metals [4]. Notice that the ion flux fraction is a few percent when the electron density is the order of 10^{10}cm^{-3}. This is a typical ionization level for DC conventional sputtering and is primarily due to the Penning ionization. At higher electron density, however, electron impact ionization dominates the Penning ionization of metal species. At electron densities greater than $\sim 10^{11}$cm^{-3}, the important parameters that determine how completely a metal flux will be ionized in an IPVD reactor are the electron impact ionization cross section, the ionization potential of the metal, and the mobility of metal ion in a buffer gas. The first two factors relate to the generation of metal ions and the mobility sets the loss rate. For example, although Ti has a higher ionization threshold than Al, the relative ionization of Ti atoms is higher since the cross section is twice that of Al while the mobility of Ti^{+} is

somewhat lower. Copper, on the other hand, has a much lower cross section and a higher ionization potential than Ti or Al. These factor make Cu more difficult to ionize. Finally, carbon ionization is included in the figure to demonstrate that atoms with high ionization potential (11.26 eV for carbon) and high ion nobilities are not significantly ionized in an argon plasma even at densities approaching 10^{13}cm^{-3}.

Although the global model presented above is useful for a basic understanding of IPVD, the model assumed a spatially homogeneous discharge. Experimental measurements of the axial variation of the Al and Al^{+} densities was presented in [14, 4, 15]. The neutral Al density is the greatest near the target and decreases nearly exponentially toward the substrate. The Al^{+} density, however, is sustained by electron impact throughout the plasma volume and remains relatively constant along the axis of the chamber. The high fraction of metal ionization are attained at the wafer by the combined effect of neutral density decay due to diffusive losses and approximately uniform volume generation of metal ions extending down to the region near the substrate. Notice that although the bulk ionization degree near substrate is only 0.3, the ionized flux fraction is about 0.8.

2.4.2   ECR based IPVD technique

In the late 1980s with the advent of high density plasmas such as ECR plasmas or inductively coupled RF plasma, it became apparent that these plasma could be readily contaminated by metal atoms from the chamber walls. These metal atoms were emitted by wall sputtering, unipolar arcs, or even evaporation from uncooled surfaces. Once in the plasma, these metal atoms were easily ionized and could be detected optically. This was originally viewed as a major problem, because the metal atoms and ions were then deposited on the various dielectric surfaces such as on the microwave window and shielded out and reflected the incident microwave power from entering the plasma chamber.

Taking this a step farther, metal atoms could be intentionally introduced into the high density plasma either by sputtering or evaporation. This require the plasma system to be carefully designed so that the subsequently deposited metal films did not block the incident microwave power.

In the ECR based tools, metal atom source must be shielded from the direct line of sight of the microwave window. Ideally, this eliminate any deposition from neutrals on the window.

First ECR based tool used the evaporation as the source of metal atoms. It was successful in demonstration deposition into high aspect ratio semiconductor features, but there was little enthusiasm for trying to reintroduce evaporation as a manufacturing deposition technology due to problems with alloy control, reliability, tool dimension, etc. Second generation ECR tool were all configured

for the use of physical sputtering as the means of introducing metal atoms into the plasma. The plasma density could approach the 10^{13}cm^{-3} at input powers of several kW and at very low operating pressures. These devices used a common plasma for the sputtering process as well as for the metal ionization process. In these conditions, it was not necessary that the metal sputtering cathode operates in the magnetron mode; the plasma densities as well as the ion currents were similar to magnetron plasmas.

In ECR tools mean free path for ionization is generally in the order of tens centimetres under typical operation conditions. It means that for a typical distances of about 10 centimetres the flux of sputtered species is only $\sim$ 30 % ionized. Increasing the pressure can results in a more sputtered atom scattering due to collisions with buffer gas, thermalization and in an increase in the relative ionization. However, at higher pressures the likehood of arcing in the microwave launcher region increases too since the plasma density in that region becomes very high. In general, ECR tools operate best in low pressure region which has only little if any gas scattering effect on the sputtered flux. However scattering of sputtered atoms and subsequent thermalization is the crucial condition for good IPVD reactor work and therefore ECR enhanced PVD technique was replaced by technique based on various types of inductively coupled plasma.

2.4.3 RF based IPVD technique

The RF based IPVD systems differ from the ECR tools in that the sputtering process uses conventional magnetron sources, running independently from the dense, inductively coupled plasma which is used for the metal ionization. That means, that sputtering and ionization can be handled separately. The dense RF plasma is formed by a metal coil antenna, typically larger in overall diameter than the magnetron cathode and located few centimetres from both the cathode and the sample. The number of turns has varied from one to about five, but in general smaller numbers of turns and larger diameter coil cross section are better at creating a more inductive plasma with higher plasma density. The most widely used driving frequency for the RF coil is 13.56 MHz primarily due to widespread power supply availability.

The RF coils in early work was constructed from Al or Cu tubing and was water cooled. More recent commercial tools have been developed with uncooled, single turn coil designated to operate with sufficient coil sputtering. To operate under appropriate conditions, there are at least three operating modes. One is to tune the coil such that the net erosion rate is equal to the deposition rate, or perhaps just slightly less. Because it is difficult to keep this condition same during a long process, sputtering of coil material into the plasma and contamination of deposited film may occur. This requires the coil to be constructed of high purity

material same as magnetron cathode. A second alternative is to operate the coil in a net deposition mode. This allows to use of any type of coil material, however it leads to eventual peeling and particle formation, requiring more frequent coil cleaning or replacement. A third alternative is to shild a coil behind a Faraday shield, which provides an unbiased surface for deposition in place of the coil. The Faraday shield must have several gaps to allow penetration of the applied field into the plasma.

The relative ionization at the sample location was found to be strongly dependent on the applied RF power and the operating pressure. Increase of applied power increases the plasma density. Increase of pressure results into more efficient thermalization and increase of plasma density coupled with general cooling of the electron temperature.

2.4.4   High power pulsed magnetron discharges

Physical sputtering is predominantly a neutral atom emission process. In a reactive sputtering of highly insulating materials, it is very difficult to maintain simultaneously a process stability and a high deposition rate. It is due to often presence of arcs. Arcing can be eliminated by not allowing a very high degree of positive charge accumulated on the target surface. In other words, arcing can be prevented by periodically discharging the charge build-up on the surface of the insulating layer, before breakdown occurs. This can be achieved by the employment of pulsing technique. In a unipolar pulsed magnetron, sputtering of target material occurs during the pulse-on time accompanied by charge accumulation on the target surface. During the pulse-off time, the accumulated charge is discharged through the plasma (for more detail see e. g. [17]).

A promising pulsed IPVD technique was developed in 1999 [18], which combines a powerful power supplies with a conventional planar magnetrons. In DC magnetrons, the target power density is limited by target overheating since most of the energy of positive ions accelerated to the cathode is transformed to the heat. In this novel technique, the discharge power is concentrated in short pulses keeping the average power at moderate few W/cm^2. Operating with a metal target in non reactive mode, it permits to increase the power applied during a pulse to the value of few kW/cm^2. For a short time (some tens of microseconds) a very dense plasma is sustained near the magnetron cathode, which induces simultaneous target sputtering and efficient ionization of sputtered vapour.

This recent sputtering process in now intensively studied and still improved e.g. a grooved target to enhance the discharge current at given magnetron voltage due to hollow cathode effect [19], combining the high power pulse sputtering with a secondary plasma between the target and the substrate (work in Mons and Orsay), preionization (chapter 4 and 5 of my manuscript) etc.

2.5 Conclusion

In this chapter, there is given an overview of the most important physical phenomena taking place during the magnetron sputtering together with the state of the art of PVD and IPVD techniques.

Sputtering is neutral atom emission process in which an energetic particle bombards a target surface with sufficient energy to eject one or more atoms from the target. One is interested in increasing of the ionization degree of sputtered particles. Ion assisted thin film grow generally improves quality of deposited thin film and directionality of the deposition process is needed particularly in microelectronics applications. In many IPVD reactors, an additional, high electron density, inert gas plasma between the target and the wafer is used to ionize the sputtered particles diffusing towards the substrate. The important parameters that determine how completely a metal flux will be ionized are the electron impact ionization cross section, the ionization potential of the metal, the mobility of metal ion in a buffer gas, the additional plasma density and the electron temperature. Another way, how to achieve significant ionization degree of sputtered particles is to pulse magnetron cathode by short and high power pulses. For a short time (some tens of microseconds) a very dense plasma is sustained near the magnetron cathode, which induces simultaneous target sputtering and efficient ionization of sputtered vapour.

The study of the IPVD techniques is still of the current interest. At the present time, the main goal of many studies is to optimize the deposition process in order to obtain thin films of better quality. Results of the plasma diagnostics can be used to identify the most important processes taking place in the plasma phase. Better understanding of these processes could help to find optimal conditions for thin film deposition in the studied reactor. Comparing these results with those already have been published could give general behavior of the plasma during the deposition process. This is the aim of my thesis.

Chapter 3

Microwave Assisted PVD

3.1 Introduction

As it has been pointed out in previous chapter, in most of IPVD reactors a RF coil is used to create a secondary discharge between a magnetron target and a substrate. At Orsay, an alternative technique has been developed combining DC magnetron sputtering device with secondary microwave plasma created by a pair of microwave antennas. Working in surface wave plasma excitation mode [20] this microwave device allows to obtain high electron density ($\sim 10^{12}$ cm^{-3}) along the very long antenna tubes. The potential advantage is the possibility to supply the industrial continuous linear processes which use a very long rectangular cathodes by a secondary plasma homogeneous along all the length of the cathode.

The goal of all IPVD reactors is to ionize sputtered particles. From the practical point of view, the most important is to find out how the secondary plasma influences the ion and neutral fluxes to the wafer. It is closely connected to the study of ionization degree of sputtered particles in the substrate area. To get this information, it is essential to carry out quantitative measurements near the substrate. However, I wanted to well understand this reactor as a complex system and hence the spatially resolved plasma diagnostics, not only near the substrate, but everywhere in the magnetron-substrate area were performed. Particularly, we focus on the optical absorption spectroscopy using a recently developed method for simultaneous determination of the sputtered species density and temperature [21].

At the beginning of this chapter, our experimental set-up and diagnostic methods which were used to characterise the plasma will be described. Principles of the optical absorption spectroscopy technique which was performed using pulsed hollow cathode lamp and a numerical procedure which allows to obtain from measured data atom and ion densities and temperature of sputtered species will be pre-
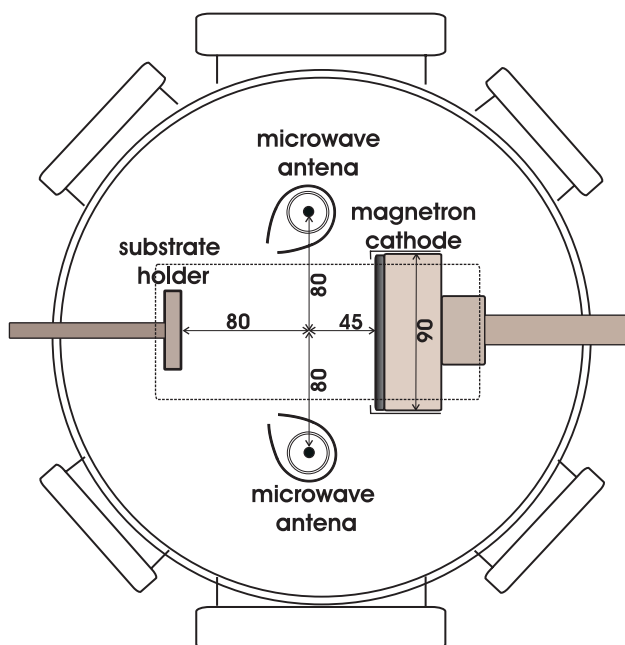
Figure 3.1: Schema of the IPVD reactor with a magnetron cathode, two microwave antennas to ionize the sputtered vapour and a substrate holder.

sented. After that, the main results of spatially resolved Langmuir probe, optical emission and absorption spectroscopy measurements will be shown. After that, discussion and interpretation of obtained results follow. The study is devoted to quantify the dominant effects induced by microwave plasma by a simple model. At the end, this chapter will be concluded and the main results will be pointed out.

3.2 Experimental set-up and diagnostic methods

3.2.1 Experimental set-up

The apparatus, shown in Figure 3.1, is a cylindrical metallic vessel, 50 cm in diameter and 45 cm in high. It consists of a planar rectangular titanium cathode, two coaxial-type microwave antennas and a substrate holder. The cathode supplied by a 1.5 kW DC generator is 21 cm long and 9 cm width. Microwave antennas are located perpendicularly to the magnetron-substrate axis, 4.5 cm from the magnetron cathode and 8 cm from the axis. They are supplied by 1.2 kW microwave generators operating at frequency of 2.45 GHz. The chamber was pumped prior to each measurements by a turbomolecular pump backed by a rotary pump down to the pressure of 10^{-3} Pa. Working pressure is measured by MKS baratron and

Figure 3.2: The side view photograph of our experimental set-up.

controlled by flow and exhaust throttle valve MKS type 655B. The argon working pressure was usually 4 Pa at argon flow of 200 sccm.

A side view photograph of our experimental vessel is shown in Figure 3.2 and a top view photograph of our microwave and magnetron discharge taken through a upper window is shown in Figure 3.3.

The drawing of the microwave alimentation is schematically shown in Figure 3.4. It consists of a copper tube with a diameter of 1 cm, centred in a quartz tube of 3 cm in diameter. For sufficiently high microwave power (in our case higher than 400 W), this configuration allows the surface wave propagation ensuring the high electron density along the whole length of the quartz tube. The wave propagation is reflected by a short circuit at the bottom of the reactor. To avoid the deposition of metallic films on the quartz tube, which will prevent the surface wave propagation, we placed a metallic protection around each of them. It limits the exposition of the quartz to the sputtered vapour. This metallic cover surrounds the quartz tube with a vertical opening through the entire length of the quartz tube. The shape of the protection and orientation of the opening is shown in Figure 3.1. Argon, the working gas, is introduced directly inwards the antenna protection to favour the plasma ignition and expansion by increasing pressure in-
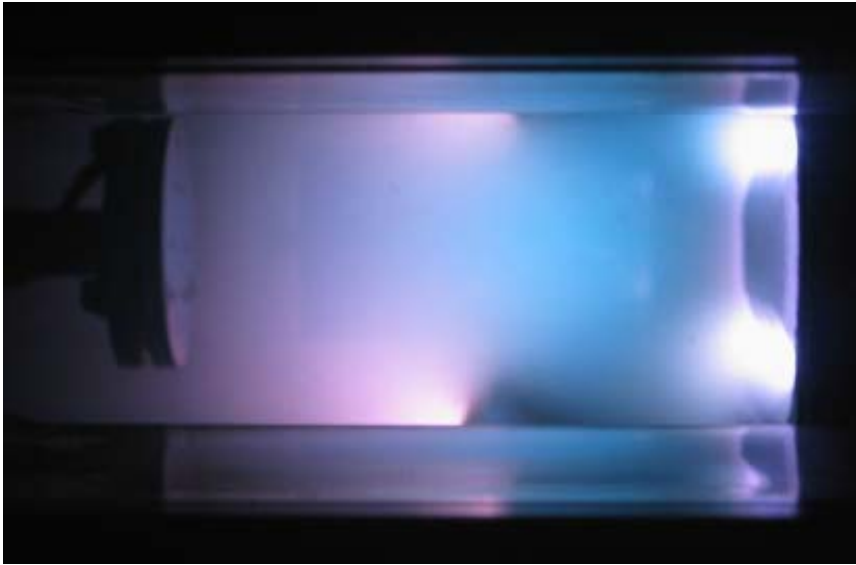
Figure 3.3: The photograph shows our IPVD system in operation. The red glow is the microwave plasma which is excited by two antennas. Titanium atoms are sputtered from target at the right side of the photograph and then ionized as they move toward the substrate holder located at the left side.

side (ideal pressure range to ignite a microwave discharge is few hundreds of Pa and in our case, we are significantly below).

The reactor is designed in order to allow optical diagnostic and Langmuir probe measurement. Spatially resolved optical emission spectroscopy has been performed in order to get qualitative information about densities of excited species together with a rude information about titanium ground state atom and ion spatial evolution using the actinometry method. Spatially resolved optical absorption spectroscopy allows us to get spatial evolution of absolute titanium atom, metastable and ion densities together with titanium ionization degree and titanium atom temperature. Langmuir probe measurement gives us electron density, plasma and floating potentials, electron distribution function or assuming Maxwell distribution the corresponding electron temperature.

Spatially resolved optical emission spectroscopy has been carried out through the upper window using a system of 13 collimators placed equidistantly with 1 cm step. The first was located 0.2 cm from magnetron cathode, the last one 0.2 cm from the substrate holder. They were designed to allow the spatial resolution better than 0.5 cm. The light emitted by the plasma is collected into 13 optical fibres guiding the light from the collimators and the entrance slit of ARC 500i imaging spectrometer equipped by a CCD camera, allowing to measure and record all 13 spectra at the same time. The signal was collected from entire high of the reactor
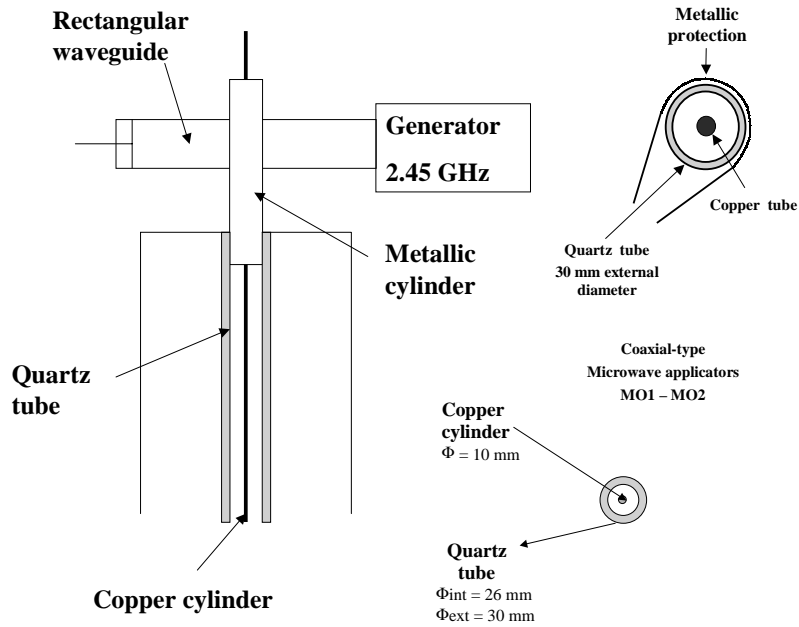
Figure 3.4: Top and side view on the microwave antenna allowing the surface wave propagation.

(45 cm).

The schema of a experimental configuration used to perform spatially resolved absorption spectroscopy measurement is shown in Figure 3.5. It has been carried out using a titanium hollow cathode lamp. Lens are used to transform the light coming from the lamp in a parallel beam. Along the magnetron-substrate axis a moving mirror is used to reflect the beam into the reactor through the upper window . The light crosses the plasma vertically, leave the reactor by lower window and is focused by another lens in an optical fibre. The light is then analysed by a Jobin-Yvon HR1000 spectrometer equipped by a photomultiplier tube. Signal from desired component is measured by Tektronix TDS 340A oscilloscope synchronized with the lamp excitation.

With commonly used DC lamp excitation, it was able to measure only the density of titanium ground state atoms. The titanium ion density was impossible to determine due to the lack of sufficiently high intensity of Ti ion line produced by continuously running hollow cathode lamp. In order to obtain sufficient Ti ion emission, a pulse excitation system of hollow cathode lamp was developed. An example of the hollow cathode lamp current and the titanium atom and ion lines production in continuous and pulse mode is demonstrated in Figure 3.6.

Figure 3.5: The schema of spatially resolved optical absorption spectroscopy measurement.

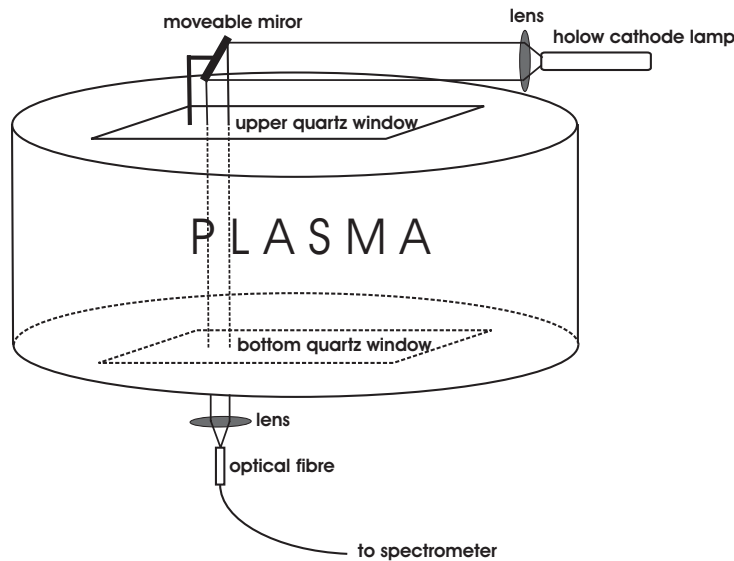The line intensities produces by the pulsed excited hollow cathode lamp has been modified by factor $1/\tau f$ (τ - pulse duration, f - repetition frequency). It allows to compare line intensities produced by DC excited hollow cathode lamp with them produced during a pulse on time. In the case of pulsed excitation titanium atom lines increase ~ 80 times and titanium ion lines ~ 230 times comparing to DC excitation.

3.2.2 Simultaneous determination of titanium atom density and temperature by optical absorption spectroscopy

To determine the absolute density of ground state or metastable state species in a plasma discharge or post-discharge, optical absorption spectroscopy is one of the diagnostic techniques widely used. It is complementary to atomic emission spectroscopy and became possible for a wide range of atoms since the 1950s. It is based on a resonant absorption of the light by the atomic species we want to analyse. The source of radiation is not a continuum, as would normally be used in absorption spectroscopy, but may come from a hollow cathode lamp. A lamp contains a anode, a cup-shape cathode, made from the element to be analysed and a buffer rare gas. When a voltage is applied, the radiation emitted, apart from that from a carrier gas, is from the atom to be observed in absorption. The radiation then passes through the plasma and a part of them is absorbed by the atoms in the plasma. The absorption coefficient A is determined by measuring the intensity I_0
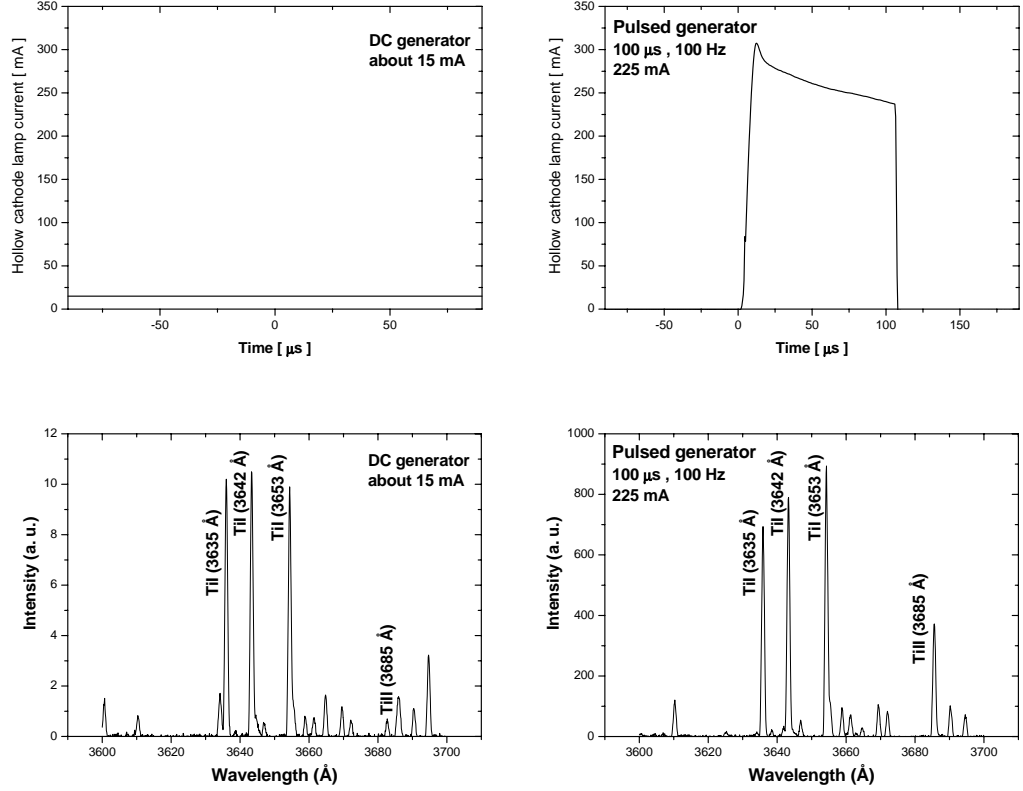
Figure 3.6: An example of the hollow cathode lamp current and the titanium atom and ion lines production in DC and pulsed excitation.

emitted by the lamp and the intensity I_t transmitted after crossing the plasma:

$$A = 1 - \frac{I_t}{I_0} \tag{3.1}$$

Then, the determination of the density of the absorbing species requires the knowledge of the spectral line profile of the line emitted by the hollow cathode lamp and of the absorbance in the plasma.

If a particle is travelling toward the detector with a velocity v_a, then the frequency v_a at which a transition between two quantum levels is observed to occur is shifted with respect to the transition frequency v of a stationary particle due to Doppler effect. They are related by

$$v_a = v \left(\frac{c}{c - v_a} \right) \tag{3.2}$$

where c is the speed of light. In the case of usually assumed Maxwell velocity distribution, the line broadening (in the case of emission) or absorbance broadening
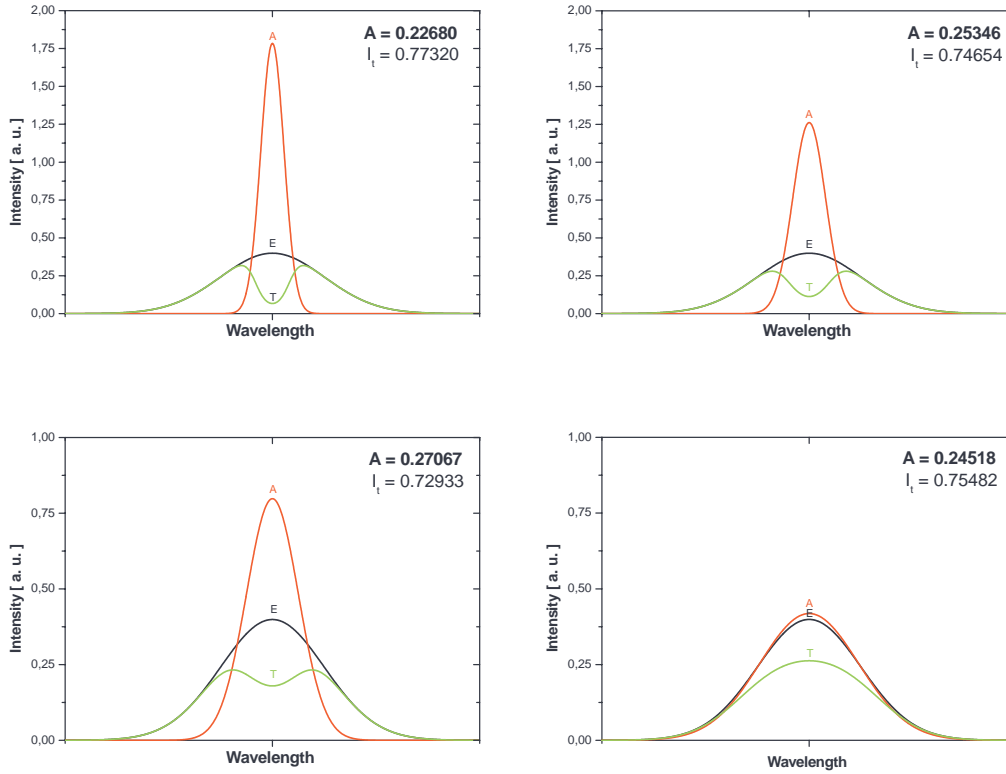
Figure 3.7: Simulation of the optical absorption spectroscopy experiment. Influence of the temperature of the absorbing species on the transmitted line shape. Black line (E) - emitted line shape, red line (A) - absorbance shape, green line (G) - transmitted line shape.

(in the case of absorption) due to Doppler effect leads to a characteristic gaussian shape with half-width at half-maximum $\Delta\nu$ given by

$$\Delta\nu = \frac{\nu}{c}\left(\frac{2kT\ln2}{m}\right)^{\frac{1}{2}} \tag{3.3}$$

where m and T are mass and temperature of an emitting or absorbing particles. In many types of low pressure, low temperature discharges, this broadening is more important than the natural line shape or pressure broadening which both contribute to different lorentzian profile. Line or absorbance in optical emission and absorption plasma spectroscopy can be describe by gaussian shapes.

The fact that absorption coefficient defines by Equation 3.1 depends on the line and absorbance shapes is illustrated in Figure 3.7. Let us assume that the

lamp emits the gaussian shape line of intensity $I_0(\lambda)$ (black line) which enters into the plasma. Because species in the plasma absorb at the wavelengths which are identical to them which they emit, plasma can be characterised by a gaussian shape absorbance $\sigma_a(\lambda)$ (red line). As the light pass through the plasma, it is absorbed inhomogenously. The line intensity at a given wavelength exponentially decreases in the plasma and intensity transmitted $I_t(\lambda)$ (green lines) after crossing the plasma of the length L follows

$$I_t(\lambda) = I_0(\lambda)e^{-\sigma_a(\lambda)L} \tag{3.4}$$

The intensities I_0 and I_t which are involved in the absorption coefficient (Equation 3.1) are the integrals of $I_0(\lambda)$ and $I_t(\lambda)$ over all wavelengths. In our example, we assumed

$$I_0 = \int\limits_0^\infty I_0(\lambda)\mathrm{d}\lambda = 1, \sigma_a = \int\limits_0^\infty \sigma_a(\lambda)\mathrm{d}\lambda = 1, L = 1 \tag{3.5}$$

Four different cases are studied here. In all of them, it was assumed that the temperature of studied plasma is lower than the temperature of the lamp. The top left figure shows the situation, when temperature of studied plasma is very low. The lamp line is absorbed strongly around the line centre and the tails are not modified. A characteristic dip is observed. As the temperature of the plasma increases, the line becomes more and more absorbed along all the profile, the dip is weaker, tails are affected too and the absorption coefficient A increases, until the highest A is obtained. Then, when temperature of the plasma overcomes some value, A starts to decrease. It is shown in the bottom figures. In the case of the bottom right figure, where the temperature of the plasma is only slightly lower than the temperature of the lamp but still higher than the plasma temperature in the bottom left figure, A is lower. Please note, that in an absorption experiment, where the gaussian shape line is absorbed in the medium described by gaussian shape absorbance, the final profile of the $I_t(\lambda)$ is never gaussian. Generally it excludes to get A in the analytic form.

According to [22], the absorption coefficient 3.1 can be written in a form of a convergent sum

$$A = \sum_{m=1}^\infty \frac{(-1)^{m+1}(k_0L)^m}{m!\sqrt{1+m\alpha^2}} \tag{3.6}$$

where L is absorption length, α is the ratio of emission Doppler width of the lamp and absorption Doppler width of the species in the plasma. Assuming the gas temperature in the lamp T_l and in the plasma T, α can be expressed as

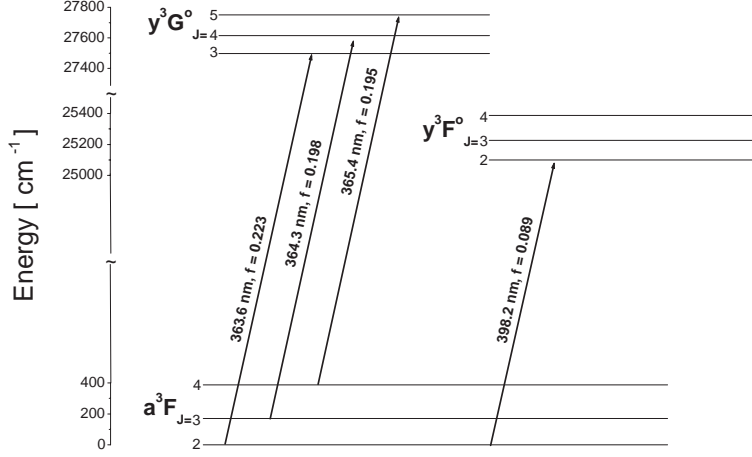$$\alpha = \left(\frac{T_l}{T}\right)^{\frac{1}{2}} \tag{3.7}$$

Figure 3.8: Schema of the titanium energy levels and transitions used to obtain simultaneously the titanium ground state density and titanium atom temperature by optical absorption spectroscopy.

The coeficient $k_0[\mathrm{cm}^{-1}]$ is given by

$$k_0 = 1.15 \cdot 10^{-6} \times f \times n \times \lambda \times \left(\frac{T}{M}\right)^{-\frac{1}{2}} \tag{3.8}$$

where f is the oscillator strength of observed transition, $n[\mathrm{cm}^{-3}]$ is the density of the absorbing species, $\lambda[\mathrm{cm}]$ is the wavelength of the transition and M is the atomic mass of the absorbing species. To obtain the density of absorbing species by optical absorption spectroscopy, transition oscillator strength f, which can be found in literature, temperature of the lamp T_l and of the absorbing species T in studied plasma must be known.

A procedure based on the absorption measurements on the titanium ground state sublevels has been developed in LPGP to obtain simultaneously the titanium ground state atom density and the titanium atom temperature [21]. The advantage of this technique is that the temperature of the absorbing species and of the lamp can be obtained additionally to the atom density. It extends the classical optical absorption techniques and the idea can be easily used for density and temperature determination in the case of other atoms with non singled or doubled ground state. This technique was used as a main plasma diagnostic tool. The basic principle, based on the work [21] is following.

The titanium ground a^3F state is a triplet state, it is composed of three sublevels with different J. Schema of energy levels used in optical absorption spectroscopy

method is demonstrated, in Figure 3.8. Three transitions are studied, involving the three sublevels:
- 363.6 nm, transition a^3F_2 - $y^3G^o_3$, oscillator strength $f = 0.223$
- 364.3 nm, transition a^3F_3 - $y^3G^o_4$, oscillator strength $f = 0.198$
- 365.4 nm, transition a^3F_4 - $y^3G^o_5$, oscillator strength $f = 0.185$
A fourth transition, involving the $J = 2$ sublevel of the ground state and having a different oscillator strength than the 363.6 nm is considered
- 398.2 nm, transition a^3F_2 - $y^3F^o_2$, oscillator strength $f = 0.089$
The absorption measurement on the first three transitions will enable us to determine the density of the titanium atoms in ground state. Assuming that titanium atom are thermalized and the velocity distribution is maxwellian, we are able to determine by a procedure described later the titanium atom temperature too. The fourth transition will enable us to determine the unknown temperature of the lamp. For a moment, let us assume that temperature of the lamp is already known. Then, the procedure to determine titanium density and temperature is the following

1. Absorptions related to the three ground states sublevels n_2, n_3, n_4 at transitions 363.5, 364.3 and 365.4 are measured. The absorption coefficients A are calculated using Equation 3.1.

2. An initial value of α is determined using the estimated lamp temperature T_l and an arbitrary initial titanium temperature $T_{Ti} = 500$ K.

3. For each transition : 363.5, 364.3 and 365.4 nm the absorption coefficient is computed from the first 100 terms of the series 3.6 changing the density value $n_J (J = 2, 3, 4)$ until the computed value equals the measured one.

4. Assuming that the populations of three titanium ground state sublevels are in equilibrium, the temperatures T_{32} and T_{42} are determined by using the n_3/n_2 and n_4/n_2 and classical Boltzmann plot procedure. A mean temperature T_{Ti} is deduced.

5. At this point a new α value is calculated and the calculation returns back to the stage 3 and continues until convergence is reached, i.e. when relative variations of α, T_{32} and T_{42} are very small (less than 10^{-3}) between two consecutive iterations.

Note, that in the described procedures, the temperature T_{Ti} determined from titanium ground state sublevels is assumed to equal the temperature related to the movement of titanium atoms and involved in the Maxwell distribution.

The lamp temperature T_l is determined using the same procedure, adding a loop on T_l, making it vary until we obtain the equality between the n_2 densities

deduced from the two lines (363.5 nm and 398.2 nm) involving the same $J = 2$ titanium ground state sublevel. As this procedure takes a lot of time, this has been done on a sample of points, leading to a mean value of T_l, which is then used for the rest of measurements.

To determine the density of titanium ions, only one transition of the quartet a^4F ground state was measured
- 338.4 nm, transition $a^4F_{3/2}$ - $z^4G^o_{5/2}$, oscillator strength $f = 0.28$
We assume that ions and neutrals have the same temperature T_{Ti}. We can obtain the density of the ion ground state sublevel with $J=3/2$ using the same procedure as was described for the determination of the neutral sublevels densities. Then, making the assumption of the equilibrium between the four ion ground state sublevels, described by the same temperature T_{Ti} estimated from titanium ground state sublevels, the total density of the ion ground state should be calculated.

The density of titanium metastable atoms in a^5F state was obtained by measuring the absorption coefficient for
- 498.2 nm, transition a^5F_5 - $y^5G^o_6$, oscillator strength $f = 0.29$
and by assuming the Boltzmann distribution in a^5F sublevels with the same temperature T_{Ti} as was estimated from ground state sublevels. The procedure does not differ from that to obtain ion ground state density only the coefficients differ.

The advantage of this method is, that it allows to determine in addition to the density of Ti atoms the temperature of the titanium atoms and the temperature of the used hollow cathode lamp.

We would like to point out ones again that the main assumptions used in the procedure are that the hollow cathode lamp produces the gaussian shape lines described by temperature T_l (which means that there is no self-absorption in hollow cathode lamp) and that the temperature of the titanium atoms T_{Ti} is the same as the temperature determined using standard Boltzmann plot procedure applied on population of titanium ground a^3F state sublevels. That means, that titanium atoms must be thermalized, which exclude to use this method at very low pressures, where the ballistic transport regime dominates.

The procedure used to determine the neutrals and ions titanium densities requires the knowledge of the absorption length L (see equation 3.6). An absorption length of 25 cm (which corresponds to a little more than the vertical length of the magnetron) has been assumed for all distances from the magnetron cathode.

Realize that measured absorption coefficient is determined from the transmitted light after it goes through all the length of the reactor (45 cm) where the density of studied species need not to be homogeneous. It means that the density obtained from this absorption coefficient is an average value which is generally not the same as the spatially averaged density along the light path. It can introduce an error. This error will be more significant when two values obtained at different

distances from magnetron cathode are compared. Near the magnetron cathode, particles will be located near the racetrack, where they are created; far away from the magnetron cathode, spatial distribution of sputtered particle density will be more broad. The relative comparison of two measurements performed at the same distance from the magnetron cathode should not suffer from this uncertainty.

But surprisingly, the most important error in density evaluation occurs, when the absorption is extremely high. Then the small variation of absorption coefficient results in great changes in estimated density. In all absorption experiments, we were careful about it. When it happens, it could be simply solved by the choice of the transition with smaller oscillator strength.

Adding a small amount of nitrogen admixture to the main Ar gas enabled us to compare the values of T_{Ti} with rotational temperature T_r determined from transition 0-2 of the nitrogen second positive system. It has been found, that both temperatures, T_{Ti} and T_r, behaved similarly with changes in experimental conditions. Despite the same relative evolutions of both temperatures, T_{Ti} was always higher than T_r.

In conclusion, described optical absorption spectroscopy method enable us to obtain simultaneously temperature and species densities. In our case, hollow cathode lamp and studied plasma were very stable, the absorption coefficient varied in the range, where the error of density estimation was low, numerical code always converted to the same final values independently on the initial values used for the first iteration. In such conditions, the relative uncertainty of this method does not exceed 10 percents for density and 30 percents for temperature estimation. Despite the fact, that the absolute values of T_{Ti} can be questioned, the relative evolution of T_{Ti} and the ratio of two temperatures, obtained at two different experimental conditions should be correct.

3.3 Experimental results and discussion

3.3.1 Langmuir probe measurement results

It needs to be mentioned, that the reactor has been already studied. The spatially resolved Langmuir probe characterization of the microwave plasma was carried out by S. Gurlui [23] in argon, neon and their mixtures. In order to optimise the coaxial systems and to study the influence of various process parameters such as microwave power, gas pressure etc. on the gas ionization, S. Gurlui did the systematic study of the electron density and electron temperature evolution in the magnetron-substrate holder axis for various experimental conditions.

For a fixed microwave power of 800 W on each antenna, the highest electron density has been obtained for argon pressure $\sim$ 4 Pa. As the microwave systems
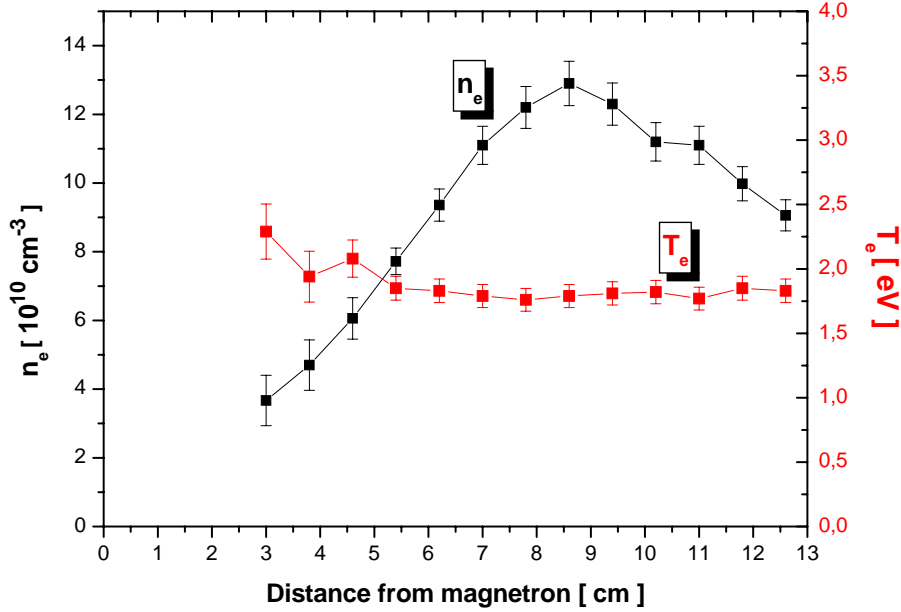
Figure 3.9: Spatial evolution of electron density n_e and electron temperature T_e for Ar pressure 4 Pa, argon flow 200 sccm and 800 W applied on each antenna.

are located 8 cm from the measurement axis, the pressure has to be low enough to permit a sufficient electron diffusion to obtain a high electron density in the centre of the reactor. This optimal pressure to get the highest electron density in the center of the reactor results from a balance between two competitive processes: electron-ion pairs creation near the microwave antenna which increases with pressure and the transport of electrons towards the central axis which becomes more important when pressure decreases.

Results obtained for this optimal pressure of 4 Pa spatially resolved along the target-substrate axis, are reported in the Figure 3.9. It has been found that the spatial distribution of the electron temperature is constant along the large region of the microwave discharge ($\sim$ 1.8 eV), however the electron density exhibits a maximum of $\sim 1 \times 10^{11} \mathrm{cm}^{-3}$ at the distance approximately 9 cm from the magnetron cathode. It was attributed to the presence of the metallic cover around the antennas. The only way, how the plasma may expand is through the vertical opening of the cover. Its orientation defines the direction of the plasma expansion and the region of the maximum electron density is exactly the region which faces the opening of the antenna metallic cover.

3.3.2 Optical emission spectroscopy results

The optical emission spectroscopy is very useful analytical technique in determining the composition of a plasma. The particles presented in plasma could be excited by many ways and after that their characteristic spectrum can be observed. However, detection of the characteristic spectrum of an atom, molecule or radical demonstrates only the presence of the species in the plasma. It is nearly impracticable to determine absolute particle density by optical emission spectroscopy.

If an upper energy state of a particle is populated only by direct electron impact excitation from particle ground state and is depleted only by radiative processes, the spatial intensity evolution $I(z)$ of a line originated from this upper energy state will be then linearly proportional to the spatial evolution of the product of ground state particle density $[N(z)]$, electron density $n_e(z)$ and a probability factor $C(T_e(z))$ depending typically on the electron temperature T_e:

$$I(z) \sim [N(z)] \times n_e(z) \int_0^\infty \text{v} \times f(\text{v}) \times \sigma(\text{v}) d\text{v} = [N(z)] \times n_e(z) \times C(T_e(z)) \quad (3.9)$$

where $f(\text{v})$ is electron velocity distribution function and $\sigma(\text{v})$ is excitation cross section.

The Figure 3.10 presents the spatial evolution of chosen Ar (750.4 nm), Ti (363.5 nm) and Ti$^+$ (368.5 nm) line intensity for magnetron current 0.5 A, microwave power 800 W and argon pressure 4 Pa.

The lowest Ar line intensity is observed near the magnetron cathode, where an important amount of energetic electrons is confined by the external magnetic field and where the electron temperature could be expected to be higher than in the microwave afterglow plasma. It signifies that argon atom density is highly reduced in magnetized plasma region with respect to other parts of the reactor. It was observed, that Ar line intensity continuously increases with the distance from the magnetron cathode and does not decrease even for distances higher than 9 centimetres, where n_e decreases and T_e remains constant (see Figure 3.9). It signifies that ground state argon density is not constant in microwave plasma too. The use of absorption spectroscopy technique will allow us to estimate the titanium atom temperature and assuming that the titanium and argon atoms are thermalized, it will permit to understand why the Ar intensity does not follow the n_e profile.

From the Figure 3.10, one can observe that titanium ion intensity continuously increases with the distance from magnetron cathode however titanium atom intensity does not vary a lot.

In the actinometry method a reference rare gas (generally Ar) is introduced in the percent range into the studied plasma and intensities of two emission lines, one of the studied species and the other of the reference gas, are divided in order to calculate the studied species density. It is assumed, that the excited states, from
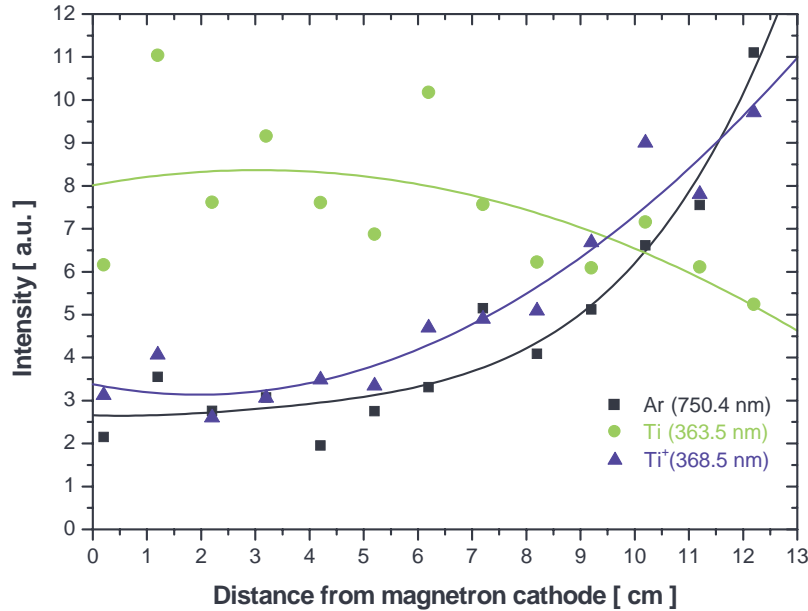
Figure 3.10: Spatial evolution of Ar (750.4 nm), Ti (363.5 nm) and Ti$^+$ (368.5 nm) line intensity for argon pressure 4 Pa, argon flow 200 sccm, magnetron current 0.5 A and 800 W applied on each antenna. Points represent the measured data, lines result of a numerical smoothing procedure.

which these lines originate have about the same energy and are populated from the ground states by an electron impact. Thus, they are affected by excitation of the same electron energy group. Moreover, the corresponding excitation cross sections need to have a similar shape. For more detail about the principle of actinometry method, see for example [24] or [25]

Actinometry method was performed using the line evolutions from Figure 3.10. The Figure 3.11 shows the spatial evolution of the Ti/Ar and Ti$^+$/Ar intensities ratio for magnetron cathode distances higher than 5 cm. At this region, T_e does not vary a lot. However, as was discussed previously, the strange Ar line intensity evolution indicates that the Ar gas density varies significantly even at high distances from the magnetron cathode. It limits usefulness of Ar lines as a good actinometrical reference. Moreover, the excitation energy and cross section for Ti and Ti$^+$ are not similar to that for Ar. One could assumed that Ti$^+$/Ar and Ti/Ar intensities ratios follows only qualitatively and not very reliably the evolution of titanium atom and ion density. From the Figure 3.11 one could conclude that titanium atom density decreases with the distance from the magnetron
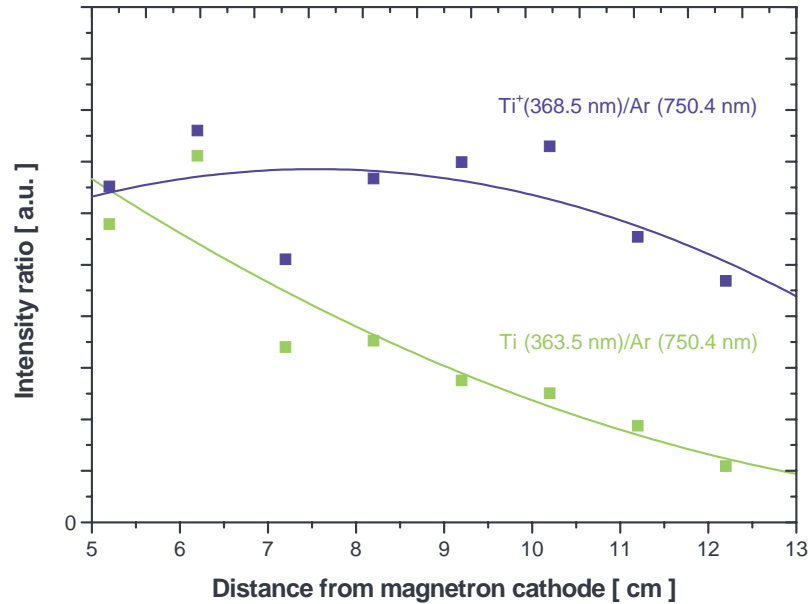
Figure 3.11: Ti$^+$ (368.5 nm) to Ar (750.4 nm) and Ti (363.5 nm) to Ar (750.4 nm) line intensity ratios for argon pressure 4 Pa, argon flow 200 sccm, magnetron current 0.5 A and 800 W applied on each antenna.

cathode, however titanium ion density remains almost constant between the magnetron cathode and substrate holder. More detailed and quantitative analyses can not be provided.

The intensity ratio of the lines emitted by Ti$^+$ and Ti should follow qualitatively the Ti$^+$ to Ti density ratio. Both energy states have practically the same excitation energy and form of corresponding cross sections should be similar too. Typical results for ion to neutral line ratio for a argon pressure of 4 Pa, magnetron current of 0.5 A and different microwave powers are reported on Figure 3.12.

For microwave powers lower than 400 W, the microwave plasma was not ignited. For low powers all intensities rapidly decrease with distance from magnetron cathode keeping the Ti$^+$ to Ti intensities ratio the same. We could conclude that only the light emitted by magnetron plasma and reflected by the metallic vessel is detected by outlying collimators. For higher microwave powers, we can observe the increase of the intensity ratio with the distance from the magnetron. Increasing the microwave power the increase of line ratio is more obvious. At this moment, we can conclude that applying the additional microwave plasma the ionization degree of sputtered vapour increases. For higher distances from mag-
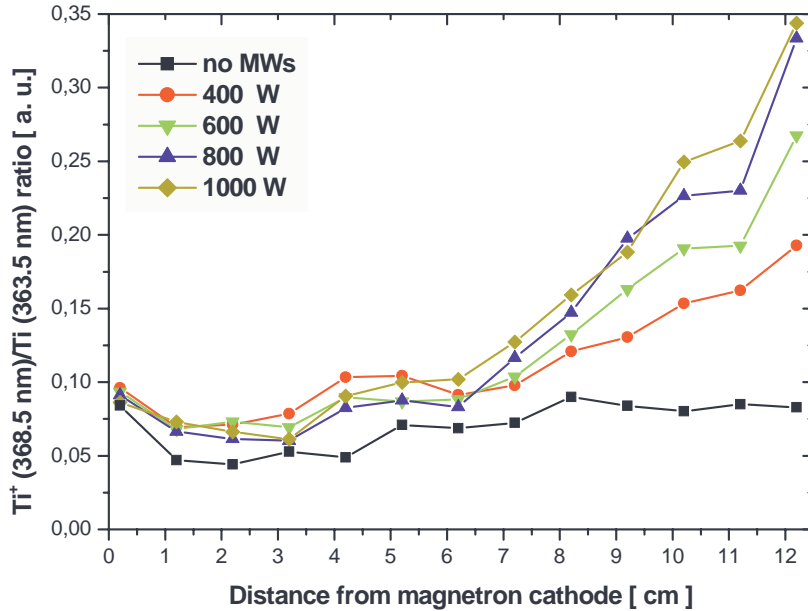
Figure 3.12: Ti$^+$ (368.5 nm) to Ti (363.5 nm) line intensity ratio as a function of the distance from the magnetron cathode for various microwave powers injected on each antenna. The argon pressure was 4 Pa, argon flow 200 sccm and magnetron current 0.5 A.

netron cathode the metal ionization degree is higher. It is difficult to set, how much it increases because we do not have any valuable intensity ratio near the substrate in the case of no applied microwave power than that determined from the reflected light coming from the magnetron discharge. Because the excitation pathways in the magnetron and microwave plasma could be different and/or because the electron energy distribution function in the magnetron and microwave plasma is not the same and the excitation cross section depends on the electron energy, it is difficult to draw further conclusion.

In order to be free of the uncertainty in the excitation mechanisms of Ti and Ti$^+$ the absorption technique was performed.
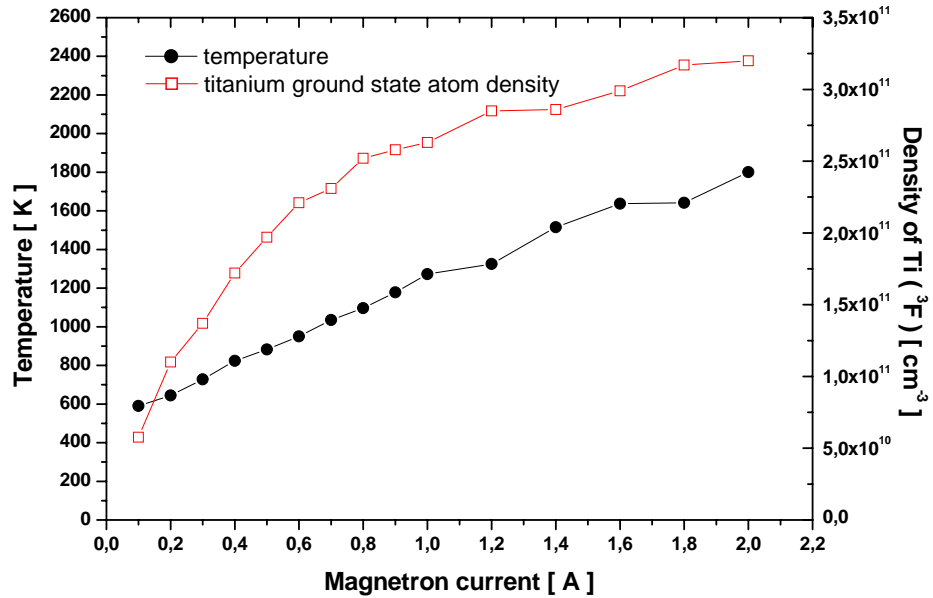
Figure 3.13: Dependence of titanium ground [3]F state atom density and titanium atom temperature on the magnetron current for argon pressure 4 Pa and argon flow 200 sccm. Measurement was performed at the distance of 2 cm from the magnetron, microwaves were off.

3.3.3 Optical absorption spectroscopy results

Production of sputtered particles and the titanium atom temperature in magnetized region

The absorption measurement was carried out to determine the density of titanium neutral atoms in ground [3]F and metastable [5]F state and the density of titanium ions in ground state [4]F.

The absorption measurement at wavelengths 363.5, 364.2, 365.3 and 398.1 was carried out. A numerical iteration program [21] was used to obtain simultaneously the neutral titanium ground state density n_{Ti}, the temperature of the used hollow cathode lamp and the titanium temperature T_{Ti}, corresponding to Boltzmann distribution in the ground state sublevels. This data processing is valid only if titanium atoms are thermalized. Detailed description of this method can be found in section 2 of this chapter.

The titanium atom density n_{Ti} and the titanium atom temperature T_{Ti} as a function of magnetron current is reported in Figure 3.13 for the Ar flow of 200 sccm

and pressure 4 Pa. The evolutions were measured very close to the magnetron cathode (at the distance of 2 cm from the magnetron cathode). During these experiments, the microwaves were turned off and only the production of titanium atoms and their temperature was studied. The magnetron voltage varied from 254 V for 0.5 A to 295 V for 2.0 A. The n_{Ti} increases with the magnetron current nonlinearly. For magnetron current higher than $\sim$ 1 A, n_{Ti} increase progressively slows down giving the density around $3 \times 10^{11} \text{cm}^{-3}$. The temperature increases with the magnetron current linearly.

Titanium atom leaves the cathode with the kinetic energy in the order of few eV, which is almost independent on the kinetic energy of the incident Ar ion. The flux of the argon ions on the cathode is linked with measured magnetron current. If the voltage applied on the cathode is constant, the flux of sputtered atoms is proportional to the flux of incident Ar ions and thus directly proportional to the magnetron current.

For the pressure of 4 Pa, the mean free path of the Ti atom in the Ar gas is in the order of few millimetres. According to [26], it requires about six mean-free paths for mean energy Ti atom to be thermalized in argon. For the pressure of $\sim$ 4 Pa, the distance required for a Ti atom to be thermalized in argon is in the order of few centimetres. Thus, the majority of Ti atoms deposits their energy in the region near the magnetron cathode, where the study was performed. Higher magnetron current induces higher flux of the sputtered particles. Each sputtered particle carries an energy of about few eV, each reflected and neutralized incident ion carries an energy in the order of tens or even hundreds eV. The major part of the kinetic energy of these particles is transmitted via collisions with the buffer gas atoms equally to all particles near the magnetron cathode. It results in the increase of gas temperature with magnetron current. We can notice that for the same magnetron current lower temperatures were observed at higher pressures. The same amount of energy was redistributed to higher amount of buffer gas particles.

From the Figure 3.13, one can observe that despite the fact that the flux of sputtered particles is directly proportional to the magnetron current, the n_{Ti} increase slows down at higher magnetron currents. The steady state particle density in a system is the result of a balance between the number of particles arriving to the system and leaving the system. Increasing the magnetron current, the flux of arriving particles increases but at the same time as the temperature increases, the Ti atom losses are favour too and the flux of particles leaving studied area increases too. Consequently, Titanium atom density increases will slow down.

Spatial evolution of the titanium species densities

Spatial distribution of titanium ground state atom density n_{Ti} and gas temperature T_{Ti} for pressure 4 Pa, argon flow 200 sccm, magnetron current 0.5 A and different microwaves powers is shown in Figures 3.14 and 3.15.
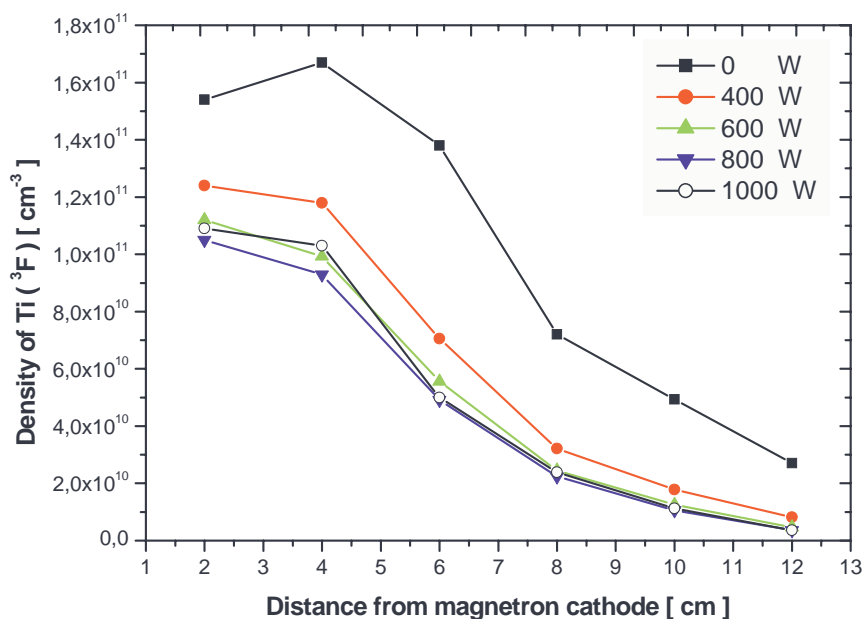
Figure 3.14: Spatial distribution of titanium ground ^{3}F state atom density for pressure 4 Pa, argon flow 200 sccm, magnetron current 0.5 A and variable microwave power.
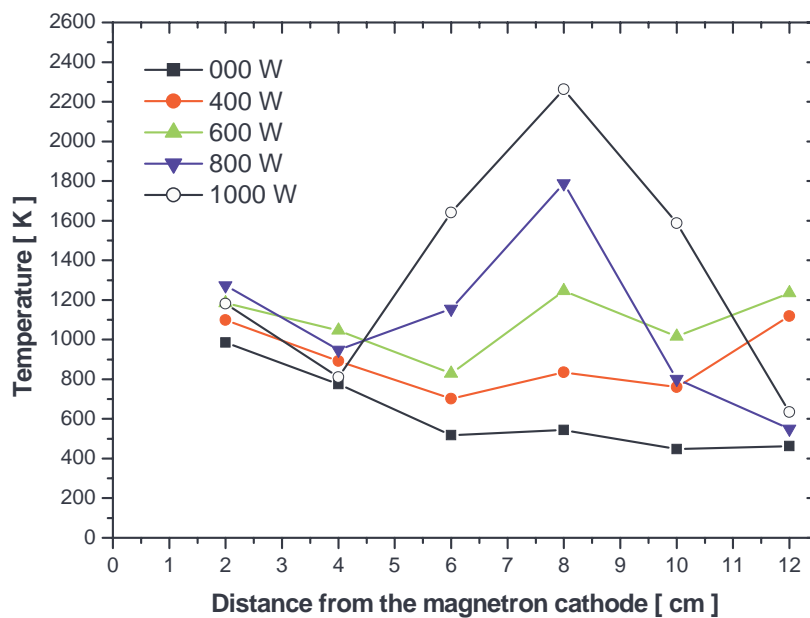

Figure 3.15: Spatial distribution of neutral titanium atom temperature for pressure 4 Pa, argon flow 200 sccm, magnetron current 0.5 A and variable microwave power.
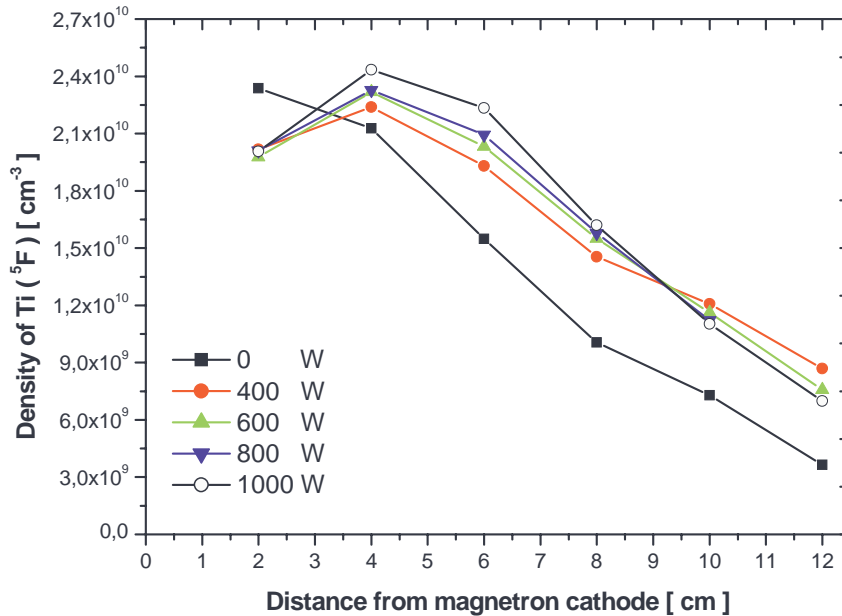
Figure 3.16: Spatial distribution of titanium metastable ^{5}F atom density for pressure 4 Pa, argon flow 200 sccm, magnetron current 0.5 A and variable microwave power.

The spatial evolution of T_{Ti} in Figure 3.15 can be divided in two parts: a magnetron region and a microwave region. The point of division between these two regions can be placed to a distance ~ 4 cm from the magnetron cathode.

For the case of no applied microwave power, the T_{Ti} is about 1000 K near the magnetron cathode. This value does not change a lot with applied microwave power. It is attributed to the heating of the buffer gas by the sputtered and on the cathode reflected particles.

In the microwave region, the T_{Ti} increases with microwave power and all curves show a significant maximum of T_{Ti} at the distance of about 8 cm. The titanium atom temperature reaches the value almost 2000 K for 800 W of applied microwave power on each antenna. The observed maximum in titanium atom temperature corresponds to the maximum of electron density shown in Figure 3.9, which results from the orientation of the vertical opening of cover placed around each antenna.

Some modelling works [27] present a theoretical study of an IPVD reactor. Even if their system is very different from our since they use an inductively coupled RF coil instead of our microwave coaxial system, the computed temperature
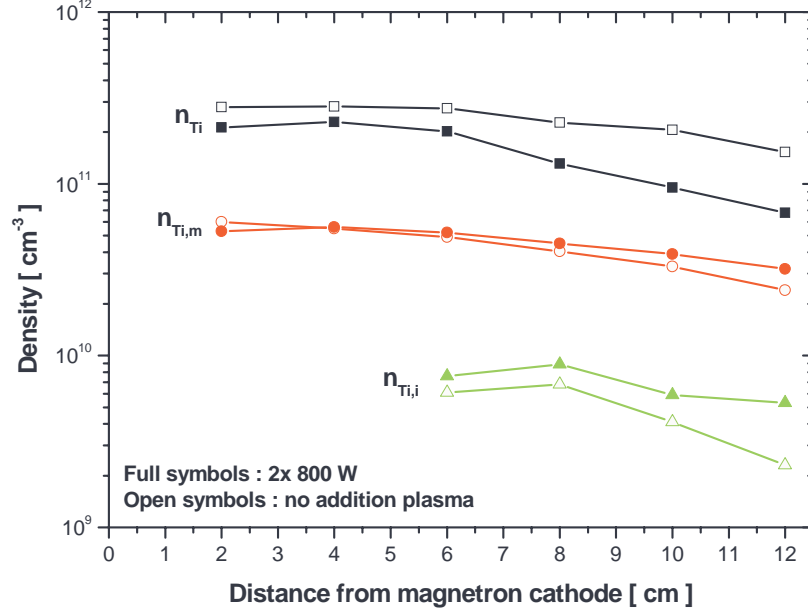
Figure 3.17: Spatial distribution of titanium ground [3]F state atom, metastable [5]F atom and ion ground [4]F state densities for pressure 4 Pa, argon flow 200 sccm, magnetron current 2 A and two cases: without additional microwave plasma (open symbols) and with additional microwave plasma created by 800 W applied on each antenna (full symbols).

values are of the same order of magnitude as our measured values. They show that both magnetron and ICP power have an influence on the gas temperature. They point out that the gas temperature variations are of great importance.

From the Figure 3.14, we can observe that at all distances from the magnetron cathode increase of microwave power results into decrease of n_{Ti}. Applying of 800 W of microwave power results into $\sim$ 30 percents decrease of n_{Ti} near magnetron cathode and into decrease of n_{Ti} by a factor 5 at distance of 10 cm from the magnetron cathode with respect to the case when no microwave power is applied.

For the same conditions as at Figure 3.14 (pressure 4 Pa, argon flow 200 sccm and magnetron current 0.5 A), the spatial distribution of titanium metastable atom density $n_{Ti,m}$ as a function of microwave power is shown in Figure 3.16. In the microwave area, we can observe for all microwave powers almost the same $\sim$ 50 percents increase of $n_{Ti,m}$ with respect to the value without microwave. The metastable atom density variation results from two competitive processes. The metastable atoms are created by the electron collision with the neutral titanium
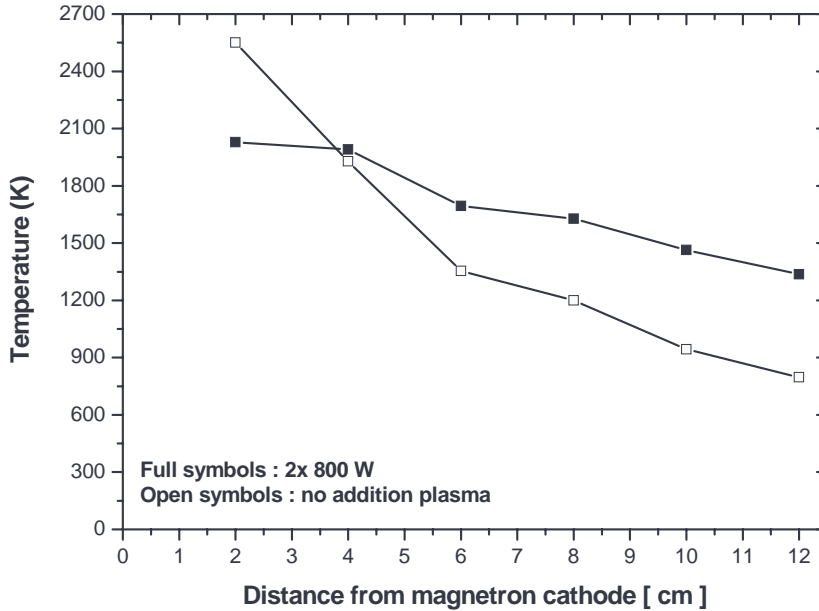
Figure 3.18: Spatial distribution of neutral titanium atom temperature for pressure 4 Pa, argon flow 200 sccm, magnetron current 2 A and two cases: without additional microwave plasma (open symbols) and with additional microwave plasma created by 800 W applied on each antenna (full symbols).

atoms and lost due to diffusion to the reactor walls. The metastable atom excitation rate follows the variation of titanium atom density and the electron density. Titanium ground state atom density is reduced with increasing microwave power (see Figure 3.14), however electron density increases with microwave power. Metastable loss rate increases with microwave power, because they are lost mainly by diffusion which depends on the gas temperature. The combination of these processes could result is Ti metastable atom density independent on microwave power. In the magnetron area, where the electron density and gas temperature are almost independent on applied microwave power, applying of microwave power results into decrease of $n_{Ti,m}$ due to decrease of n_{Ti}.

For the magnetron current 0.5 A the absorption at the wavelength 338.4 nm was very weak to determine the titanium ion density $n_{Ti,i}$ properly. Increase of the magnetron current to 2 A raises the absorption coefficient to a reasonable value to determine $n_{Ti,i}$. At this condition, the spatial variation of n_{Ti}, $n_{Ti,m}$ and $n_{Ti,i}$ are reported in Figure 3.17 for two conditions: without microwave power (full symbols) and with 800 W of microwave power injected on each antenna (open

symbols). Similar evolution, as was reported for magnetron current of 0.5 A is observed. With a microwave power of 800 W on each antenna, we can see that the presence of the additional plasma results in increase of $n_{Ti,m}$ by a factor 1.25 and $n_{Ti,i}$ by a factor 2.3 at the distance of 12 cm from the magnetron cathode while n_{Ti} decreases by a factor 2. In absolute values, n_{Ti} decreases of $7 \times 10^{10} \mathrm{cm}^{-3}$ while the sum of $n_{Ti,m}$ and $n_{Ti,i}$ increases only slightly of $1 \times 10^{10} \mathrm{cm}^{-3}$ when microwaves was turned on. Therefore, the decrease of n_{Ti} by a factor 2 near the substrate is clearly not only due to an increase in the sputtered particle ionization degree and excitation of metastables.

At the distance of 12 cm from the magnetron, which corresponds to the substrate holder position, metal ionization degree reaches the value of 5 percents. Comparing this value to the one without the microwave plasma, 4 times higher metal ionization degree was obtained with our system. For a comparison, RF coil amplified magnetron sputtering process [28] can increase the metal ionization degree by a factor 8, from ~ 3 percents in the magnetron regime to ~ 24 percents in the amplified discharge.

We report in Figure 3.18 the spatial evolution of T_{Ti} for the same experimental condition as in Figure 3.17. Increasing the magnetron current from 0.5 A to 2 A, the temperature of titanium atoms increases ~ 2 times near the magnetron cathode however far away, at the distance of 12 cm, only ~ 50 percent increase was observed. Without the microwave plasma the titanium atom temperature relaxes more slowly with the distance from magnetron cathode for magnetron current of 2 A than for 0.5 A and remains still very high in the microwave region. With the microwave power the increase of T_{Ti} is less pronounced for the magnetron current of 2 A than for 0.5 A and one can observe, that the significant maximum of T_{Ti} previously observed at the distance of 8 cm disappears. For magnetron current of 2 A and no microwave power applied, the titanium atom temperature is ~ 1300 K in the microwave region (at the distance of 8 cm) which is close to that obtained for magnetron current 0.5 A and 600 W of microwave power. The presence of the microwave plasma increases the titanium atom temperature by smaller extent in the case of higher magnetron currents, because at high magnetron current operation, gas is already heated even at further areas from the magnetron cathode.

3.3.4 Role of the substrate, ion and neutral fluxes to the substrate

In the deposition processes, the main parameters are the fluxes of sputtered species on the substrate. We evaluated the total flux of neutral species on the substrate Γ_n using the equation 2.5. The neutral species densities - n_{Ti} and $n_{Ti,m}$ - was measured near the substrate holder by absorption. Thermal velocity deduced from
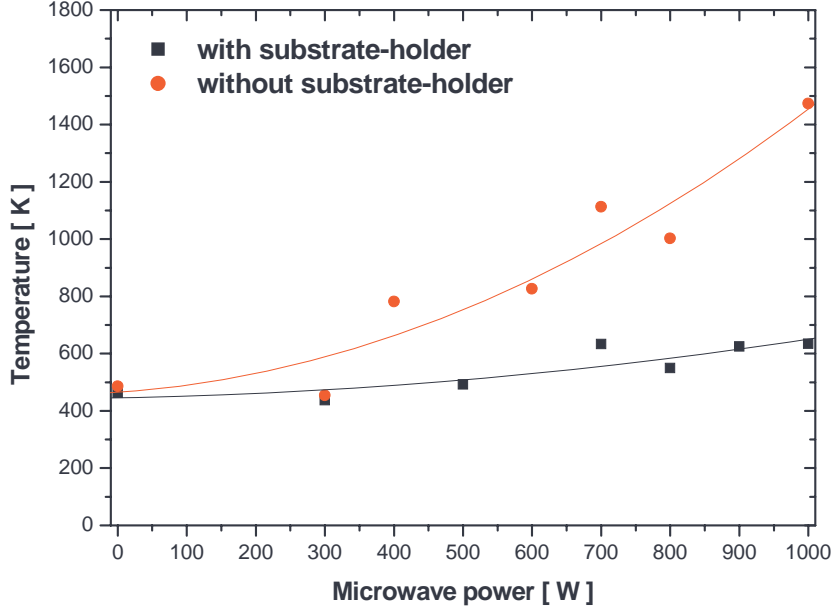
Figure 3.19: Evolution of titanium atom temperature measured at the distance of 12 cm from magnetron cathode for argon pressure 4 Pa, argon flow 200 sccm, magnetron current 0.5 A and variable microwave power. Black line - substrate holder was present, red line - substrate holder was removed.

the measurement of the T_{Ti} was assumed. Measuring the distribution of the magnetic field, our magnetron have been found to be well balanced. The electrons are well confined near the cathode and when the microwave power was turned off, only very low electron density was excepted at the distance of 12 cm from the magnetron cathode. For the ion flux Γ_i we used the same equation 2.5 as for the neutral species when the microwave power was turned off. However, when the microwaves were turned on, for microwave power of 800 W, the electron density is about $8 \times 10^{10} \mathrm{cm}^{-3}$ near the substrate and ions are accelerated to Bohm velocity which is much higher than the thermal velocity. In such case, we used the equation 2.4 to get the ion flux on the substrate.

For the pressure of 4 Pa, magnetron current of 2 A and microwave power 800 W applied on each antenna, $\Gamma_n = 2 \times 10^{15} \mathrm{cm}^{-2}\mathrm{s}^{-1}$ and $\Gamma_i = 6 \times 10^{14} \mathrm{cm}^{-2}\mathrm{s}^{-1}$ are found. Resulting flux ratio Γ_i/Γ_n is 0.3. Without additional microwave plasma, $\Gamma_n = 2.6 \times 10^{15} \mathrm{cm}^{-2}\mathrm{s}^{-1}$ and $\Gamma_i = 3 \times 10^{13} \mathrm{cm}^{-2}\mathrm{s}^{-1}$ are found. Resulting flux ratio Γ_i/Γ_n is only 0.01. It shows that applying of 800 W on each microwave antenna Γ_i increases by factor 20. With the microwave plasma, the ionized flux

fraction $\Gamma_i/(\Gamma_i + \Gamma_n)$ is 0.24. This experimentally estimated value well corresponds to the value 0.28 calculated by [4] for the secondary plasma with an electron density of about 10^{11}cm^{-3}.

All experiments have been carried out with the substrate holder places at the distance of 12.5 cm from the magnetron cathode. We would like to show, how the presence of the substrate holder influences the T_{Ti}. Figure 3.19 shows results of T_{Ti} measurement performed at the distance 12 cm from magnetron cathode as a function of applied microwave power. Measurements have been carried out with and without substrate holder in order to determine its effect on titanium atom temperature. Magnetron current was 0.5 A and argon pressure 4 Pa. It clearly appears that the presence of substrate holder efficiently reduces the titanium atom temperature.

3.4 Detailed discussion and simple model

3.4.1 Interpretation of spatially resolved optical absorption spectroscopy results

In this section, a simple model for explanation of n_{Ti} decrease with microwave power is shown. The goal of this model is to quantify the role of various physical processes, which could influence the vapour density in magnetron and microwave plasma. Various physical processes will be taken into account until the spatial distribution of $n_{Ti,0}$, measured in the case of no microwave power applied will be obtained from spatial distribution of titanium ground state density $n_{Ti,x}$, measured for the applied microwave power of x Watts. From many curves, we choose simply the one corresponding to applied microwave power of 700 W to demonstrate the influence of secondary microwave plasma on n_{Ti}.

Let us first estimate the effect of the excitation of titanium atoms from ground to upper metastable state on the titanium ground state density. The loss of $n_{Ti,x}$ due to the excitation of metastable ^{5}F levels was taken into account by adding the concentration of metastable titanium atoms $n_{Ti,m,x}$ to $n_{Ti,x}$ to obtain $n_{Ti,x}^m$

$$n_{Ti,x}^m = n_{Ti,x} + n_{Ti,m,x} \tag{3.10}$$

The value of $n_{Ti,x}^m$ should be the same as $n_{Ti,0}^m$, if the excitation of ground state atoms to their metastable states is the dominant mechanisms of n_{Ti} decrease.

In the Figure 3.20, there are plotted the spatial distribution of $n_{Ti,0}$, $n_{Ti,0}^m$, $n_{Ti,700}$ and $n_{Ti,700}^m$. We can observe, that adding $n_{Ti,700,m}$ to $n_{Ti,700}$, we are still far away from the value of $n_{Ti,0}^m$, we wanted to get. Now, it is obvious, that the excitation of titanium metastable ^{5}F levels is not the main effect leading to the decrease of n_{Ti} with microwave power. In these experimental conditions, the density
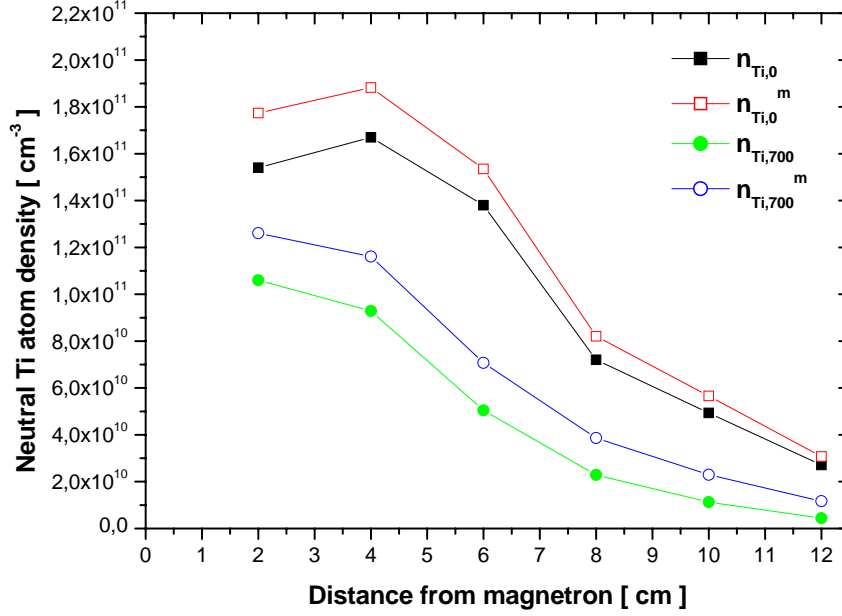
Figure 3.20: Effect of the metastable level excitation on the titanium ground state density.

of titanium ions is in the order of few percent, which is insufficient to cover the residual divergence between $n_{Ti,700}^m$ and $n_{Ti,0}^m$.

Next effects need to be taken into account. During the experiments the magnetron current was kept constant. It was observed, that increase of the microwave power results in decrease of magnetron voltage U_{mag} to keep the same magnetron current. The decrease of U_{mag} with microwave power is attributed to the coupling between the microwave and magnetron plasma. In spite that in our case the coupling between microwave and magnetron plasma is weak, the decrease of voltage, applied on the magnetron cathode results into reduction of the energy of argon ions bombarding the cathode. Consequently, it reduces the sputtering yield γ. As an example, for magnetron current of 0.5 A and no microwave power applied, the U_{mag} equals 231 V, however for 800 W of applied microwave power U_{mag} decreases to 215 V. The sputtering yield decreases from the value γ_0=0.23 to γ_{800}=0.20 [29].

The loss of $n_{Ti,x}$ due to the change of γ was taken into account to obtain $n_{Ti,x}^\gamma$

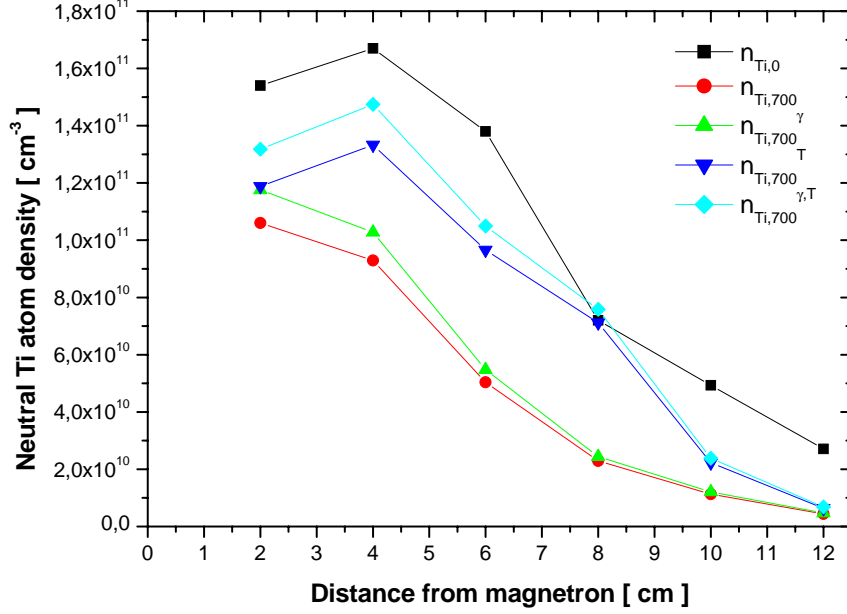$$n_{Ti,x}^\gamma = n_{Ti,x}\frac{\gamma_0}{\gamma_x} \qquad (3.11)$$

Figure 3.21: Effect of the magnetron voltage drop and gas temperature variation on titanium ground state density.

For a given pressure, we assumed, that changes of the temperature T_{Ti} results into rarefaction of all species densities presented in the plasma according to kinetic gas equation. The loss of $n_{Ti,x}$ due to changes of T_{Ti} was taken into account to obtain $n_{Ti,x}^T$

$$n_{Ti,x}^T = n_{Ti,x}\frac{T_x}{T_0} \tag{3.12}$$

In Figure 3.21, there are plotted spatial distributions of $n_{Ti,0}$, $n_{Ti,700}$, $n_{Ti,700}^\gamma$, $n_{Ti,700}^T$ and $n_{Ti,700}^{\gamma,T}$. We can observe, that in the microwave area the decrease of n_{Ti} is caused mainly by the increase of titanium atom temperature induces by microwave plasma presence. However in the magnetron area, where the gas is mainly heated by sputtered and by cathode reflected particles, the microwaves influence the gas temperature weakly and the γ effect becomes significant.

Because all assumed effects take place simultaneously, we used all equations at the same time to obtain $n_{Ti,0}^m$ from $n_{Ti,x}$. Order of the upper indexes indicates the order of the effects taken into account. Then $n_{Ti,700}^{\gamma,T,m}$ means that $n_{Ti,m,700}$ was added into $n_{Ti,700}$ after taking into account the γ and T_{Ti} effects. The $n_{Ti,700}^{m,\gamma,T}$ means that $n_{Ti,m,700}$ was added into $n_{Ti,700}$ before the γ and T_{Ti} effects were proceeded.

Figure 3.22: Effect of the metastable level excitation, magnetron voltage drop and gas temperature variation on titanium ground state density. The effects have been treated in the order given by upper indexes.

Changing the order of γ and T procedure does not change the final result, because both are represented by multiplication, which is a commutative operation. However, the position of upper index m changes the results. When the index m precedes the indexes γ and T, it means that the final result $n_{Ti,700}^{m,\gamma,T}$ will be greater than $n_{Ti,700}^{\gamma,T,m}$, where the m index is the last in the order. Physically, $n_{Ti,700}^{m,\gamma,T}$ means that the density of metastable and ground state atoms behaves the same, both undergo the same rarefaction due to the temperature increase as well as their density decreases due to the reduction of magnetron voltage. However, $n_{Ti,700}^{\gamma,T,m}$ indicates that only ground state atoms are rarefied due to the increase of temperature and influenced by the drop of magnetron voltage. Metastable atoms are not concerned by these processes. The simplicity of the model allows only to treat the physical phenomena in the order though everything takes place simultaneously. Metastable atoms are at the same time created from the ground state atoms and undergo the rarefaction as all the species in the reactor.

   In the Figure 3.22, there are shown the spatial distributions of $n_{Ti,0}^{m}$, $n_{Ti,700}^{\gamma,T,m}$ and $n_{Ti,700}^{m,\gamma,T}$. We can conclude, that $n_{Ti,700}^{\gamma,T,m}$ coincides well with the $n_{Ti,0}^{m}$ much better
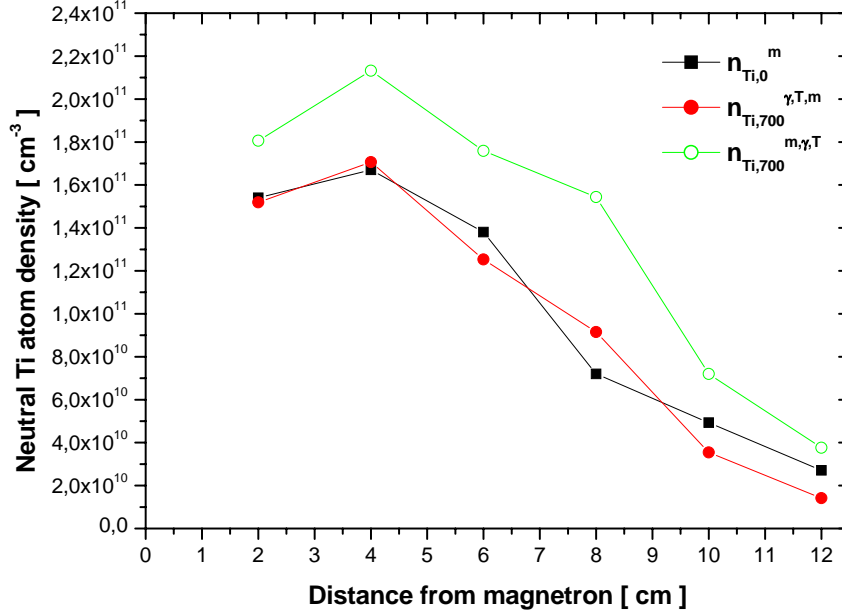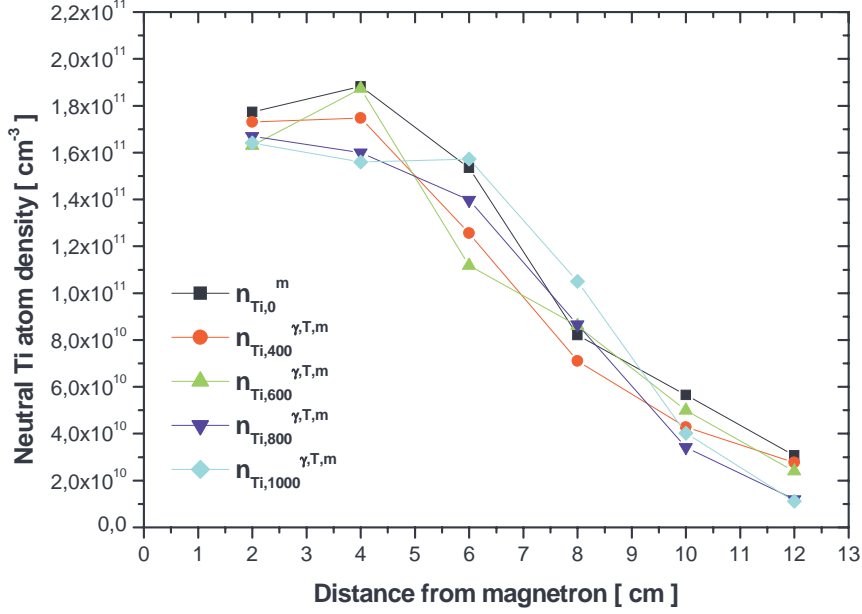
Figure 3.23: Effect of the metastable level excitation, magnetron voltage drop and gas temperature variation on titanium ground state density for various microwave powers applied on each antenna.

than $n_{Ti,700}^{m,\gamma,T}$ which is always higher. It shows that the processes taken into account in our model are satisfactory and that it is more correct to treat the excitation of the metastables at the last order after taking into account the reduction of vapour density by the heating and the change of the γ.

In Figure 3.23, there are plotted the spatial dependencies of $n_{Ti,0}^m$ and $n_{Ti,x}^{\gamma,T,m}$ for various applied microwave powers. The fact that for all experimental conditions $n_{Ti,x}^{\gamma,T,m}$ obtained from $n_{Ti,x}$ well corresponds to $n_{Ti,0}^m$ supports the validity of the model which allows to explain the decrease of n_{Ti} with microwave power and quantify γ, T_{Ti} and metastable excitation effects on titanium ground state atom density. Moreover, it proves, that all important effects has been taken into account in the model.

In conclusion, it has been shown that the main phenomenon causing the decrease of titanium ground state atom density in microwave region is an increase of temperature. Metastables and ions are more created than rarefied and so, their density increases with microwave power. In the magnetron area, the temperature effect has approximately the same importance on titanium ground state atom
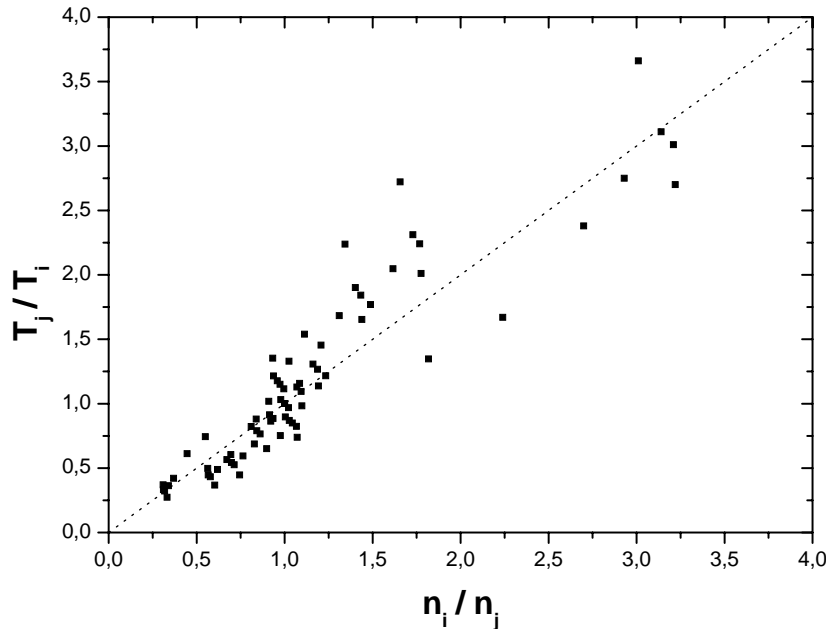
Figure 3.24: The inverse ratio of gas temperatures as a function of ratio of titanium ground state densities. Each point represents the ratio of two values at two different microwave powers. The line represents expected results according to kinetic gas equation.

density as reduction of sputtering yield and metastable level excitation.

3.4.2   Effect of temperature on titanium atom density

The titanium atom density reduction due to the increase of temperature is very obvious at the distance of 8 cm from the magnetron, where the temperature variation with applied microwave power is maximal. In the Figure 3.24 there are plotted an inverse ratio of two temperatures obtained at different microwave powers as a function of a ratio of titanium ground state atom densities. Each point represents the ratio of two values measured at two different microwaves powers. All measured data for microwaves powers 0, 300, 400... 1000 W have been used. The line represents expected results according to kinetic gas equation.

The agreement of such many experimental points with kinetic gas equation confirms the major influence of temperature on the titanium atom density decrease with applied microwave power. Moreover, it ensures us, that hypothesis, taken during the absorption data processing was correct. Notably, the hypothesis about
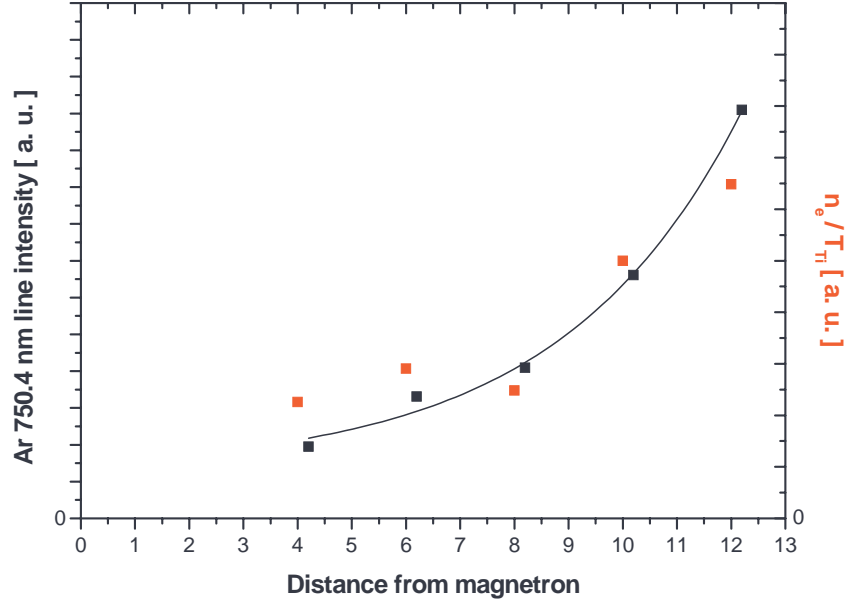
Figure 3.25: Comparison of Ar 750.4 nm line intensity spatial evolution and n_e/T_{Ti} ratio for argon pressure 4 Pa, argon flow 200 sccm, magnetron current 0.5 A and 800 W applied on each antenna.

the equality of titanium atom temperature and the temperature corresponding to distribution in titanium ground state atom sublevels proves its validity.

3.4.3 Interpretation of spatial evolution of Ar atom line intensity

Finally, we can explain the spatial variation of Ar 750.4 nm line intensity shown in Figure 3.10, particularly why the intensity does not follow the electron density shown in Figure 3.9 for distances higher than 9 centimetres. Assuming the direct excitation of the upper Ar level by an electron impact, the emission intensity is according to equation 3.9 proportional to density of electron n_e, density of argon ground state atom n_{Ar} and the probability factor $C(T_e)$.

Assuming that the titanium atoms are thermalized with argon atoms, the titanium atom temperature evolution $T_{Ti}(z)$ determined by absorption will be the same for Ar atom temperature evolution too. The ground state argon atom density

$n_{\mathrm{Ar}}(z)$ evolution can be then deduced from the kinetic gas equation

$$n_{\mathrm{Ar}}(z) = \frac{p}{kT_{Ti}(z)} \qquad (3.13)$$

From the Figure 3.9, one can conclude that the probability factor $C(T_e)$ in nearly constant for distances higher than ~ 5 cm where the electron temperature does not change a lot.

   According to the above consideration, the Ar 750.4 nm line intensity evolution should follow the evolution of n_e/T_{Ti}. Figure 3.25 shows scaled evolution of Ar 750.4 nm line intensity and the ratio n_e/T_{Ti}. Very good agreement between these two evolutions shows ones again the strong effect of the temperature on the density of species in the IPVD reactor. At the distances between 8 and 9 cm the electron density and the temperature are maximal. In this region strong Ar gas rarefaction takes place. The increase of argon line intensity for distances higher than 9 cm while n_e decreases is then simply due to faster decrease of the gas temperature than electron density.

3.5   Conclusion

In this chapter, an original IPVD reactor consisting of a magnetron assisted by an additional microwave source of ionization was studied.

   The spatial distribution of sputtered species in this IPVD reactor has been obtained by optical absorption spectroscopy measurements: densities of neutral titanium atom in ground (^{3}F) and metastable (^{5}F) state together with density of titanium ions in ground (^{4}F) state. The spatial distribution of titanium atom temperature T_{Ti} has been obtained too.

   For magnetron current of 0.5 A and argon pressure of 4 Pa, the titanium ground state density is in the order of $10^{11}\mathrm{cm}^{-3}$ in the magnetron area and $10^{10}\mathrm{cm}^{-3}$ in the microwave area. At these conditions, titanium atom temperature has been found ~ 2000 K near the magnetron cathode and ~ 500 K far away from the magnetron (10 cm from target).

   Applying the microwave power the titanium atom density is reduced in the magnetron area of ~ 30 percents, however in microwave area by factor ~ 5. The temperature increases up to value ~ 2000 K in the microwave area, however near the magnetron cathode, the temperature did not increase a lot.

   For pressure of 4 Pa, magnetron current of 2 A and no applied microwave power, the ionization degree near the substrate holder is about 1.5 percents. For 800 W of applied microwave power on each antenna, the metal ionization degree increases up to the value of 5 percents. It is an increase by factor 4 with respect

to the value without microwave. Both, the absorption and emission spectroscopy results show that the increase of metal ionization degree with the distance from the magnetron cathode is due to the huge decrease of titanium atom density simultaneously with only low increase of titanium ion density.

For magnetron current of 2 A, the flux of all titanium species on the substrate is $2.5 \times 10^{15} \text{cm}^2\text{s}^{-1}$. With 800 W of applied microwave power the flux of all titanium species on the substrate is $2.7 \times 10^{15} \text{cm}^2\text{s}^{-1}$. Comparing these values, one can easily found that microwave plasma does not influence the total flux of sputtered particles on the substrate and so the deposition rate could be expected to be not influenced by additional microwave plasma. We observed that total flux of sputtered particles is conserved independently on applied microwave power. Microwaves influence the ion fraction in the total sputtered particle flux. Applying 800 W of microwave power increases the ion flux by factor 20 with respect to no applied microwave power. It increased from value $3 \times 10^{13} \text{cm}^{-2}\text{s}^{-1}$ (without microwaves) to $5.9 \times 10^{14} \text{cm}^{-2}\text{s}^{-1}$ (800 W applied).

A decrease of titanium ground state density n_{Ti} with microwave power was observed. The model, taking into account the gas heating, metastable levels excitation and changes of sputtering yield with applied microwave power correctly describes the observed decrease of n_{Ti}. Increasing the microwave power, the n_{Ti} decrease in magnetron area was attributed to simultaneous small increase of gas temperature and drop of the magnetron voltage followed by a reduction of the sputtering yield. In microwave area, the titanium atoms in ground state are mainly rarefacted due to gas heating. The dominant role of the gas temperature on the titanium and argon atom densities was derived from both optical emission and absorption spectroscopy results. It was shown that the actinometry diagnostic method is of no much use in IPVD reactors.

The advantage of using the microwave coaxial antennas as a plasma source is that it allows to support long industrial magnetron cathodes by a secondary homogeneous plasma at long distances, which is impossible to deal with RF coil.

Unfortunately, deposition of sputtered metallic particles on the quartz tube limit long time operation. The operation time can be prolonged by proper chosen protection around each antenna. In a deposition process of dielectric films from a dielectric target or in a reactive mode, the antennas can run without any protection and the deposition of dielectric film on quartz will not decrease its efficiency.

The microwaves are easy to control, one has no problem concerning hybrid capacitive and inductive coupling such as with RF antenna. Applying sufficiently enough of microwave power ensures surface wave propagation along long tubes. Due to low potential difference between the plasma and the tube wall and low quartz sputtering yield, the quartz is not sputtered a lot and our system does not induce contamination of deposition process. It is well known [30, 31], that RF plasma could be a non negligible source of impurities in sputtering process, be-

cause it is not always possible to create the coil from the same material as the magnetron cathode. Even for proper designed coil, the potential difference between the plasma and coil should be some tens of volts.

The huge disadvantage of our system is low ionization efficiency with respect to high power injected into each antenna. The sputtered particles do not go through active plasma, which is located only near the quartz tubes, but through the plasma in afterglow, which is characterised by lower electron density and temperature.

Chapter 4

Fast Dynamics of High Power Pulsed Magnetron Discharge

4.1 Introduction

In previously published results [18, 19, 32, 33, 34, 35], unipolar high power pulsed magnetron sputtering was reported. The main advantage (apart from them presented in chapter 2) of this technique is high ionization degree of sputtered particles with no secondary ionization device in reactor chamber. Nevertheless, this method is limited by a too large delay between the beginning of the pulse and the moment when high magnetron current is reached. It requires long pulse duration (at least few tens of μs) to work in high current density regime (~ 1 A/cm^2). Long pulses increases the probability of an arc formation, which could be detrimental for deposition process.

To stabilise the high power pulsed sputtering process and to achieve the fast increase of magnetron current a home made system based on the superposition of low density preionization plasma with high voltage pulses was developed. This system was used to ignite and maintain the high density magnetron plasma and to study its time behaviours and dynamics. The results, obtained with this system will be presented in following two chapters.

At the beginning of this chapter, our experimental set-up and plasma diagnostic methods which permit time resolved study of the discharge will be shown. Time average optical emission spectroscopy carried out in the preionization mode only and in the superposition of preionization mode and high power pulses will enable us to compare qualitatively these two regimes of interest. Then we will report the time resolved magnetron voltage and current measurements for various pressures and pulse conditions. Time resolved optical emission spectroscopy, performs at many pressures will describe the time behaviour of chosen spectral line.
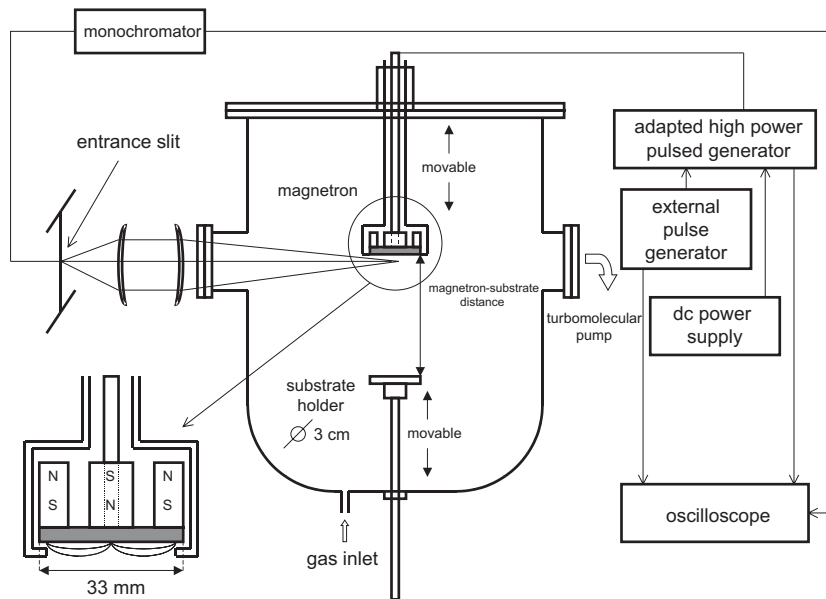
Figure 4.1: Schema of the experimental set-up

All these time resolved measurements allow us to discuss time changes of plasma composition, role of various processes and the fast transition to stable and arc-free self-sputtering regime when copper target was used. At the end, this chapter will be concluded.

4.2   Experimental set-up

The apparatus, shown in Figure 4.1 is a standard balanced planar magnetron source the type Mighty Mak-130-STD_E manufactured by Thin Film Products. It operates with a copper target (99.9% purity) of 33 mm in diameter. The cathode is located inside a stainless-steel chamber of radius R = 220 mm and height L = 350 mm.

A home made adapted pulse generator was developed in cooperation with Dr. Mihai Ganciu. It allows the superposition of a low power DC discharge ($\sim$ 4 mA, $\sim$ 300 V) and high voltage pulses (500-1100 V) applied directly on the magnetron cathode. The maximum magnetron current corresponding to 1 kV applied in pulse regime was 40 A for Ar and 65 A for He buffer gas. The system was designed to insure a fast rise and short fall (less than 1 μs) time of magnetron current and to vary the pulse parameters, such as pulse duration and repetition frequency. Pulse duration was varied from 1.5 μs to $\sim$ 55 μs. The maximum repetition frequencies $\sim$ 600 Hz was used only in the case of very short pulses. A pulse generated

by an extern pulse voltage generator (about 10 V) commands the high voltage coming from an high voltage DC generator. In our case, the pulse duration and repetition frequency were controlled by Thurlby Thandar Instruments TGP 110 Pulse Generator. Mean magnetron voltage or current regulation was provided by Technix SR 1.5-R-1500 high DC voltage generator.

The chamber was pumped prior to each measurements by a turbomolecular pump backed by a rotary pump down to the pressure of 10^{-3} Pa. Argon (helium) gas was used as a buffer gas. The working pressure was varied from 0.1 to 10 Pa by gas flow (from 1 to 15 sccm) and by exhaust throttle valve.

The processes taking place in pulsed magnetron plasma were characterized by time resolved measurements of magnetron current and voltage to get a basic magnetron characteristics and by optical emission spectroscopy to obtain the time behaviour of chosen line intensities.

To measure the magnetron voltage and current, the voltage and current probes were integrated directly into the power pulse system. After that, they were calibrated by classical commercial Tektronix large bandwidth probes.

Light emitted by the magnetized plasma together with part of plasma afterglow was collected by a system of lenses and was led to an entrance slit of a monochromator. Spectral analysis were made by Jobin Yvon THR 1500 monochromator equipped with Hamamatsu R4457P photomultiplier tube connected by an adapted 50 Ω coaxial cable to 100 MHz digital Tektronix TDS 340A oscilloscope. Signals from chosen lines were synchronised with the magnetron voltage pulse.

4.3 Experimental results

4.3.1 Time average optical emission spectroscopy

In a first approach, the discharge was investigated by a very simple way. The discharge colour was observed and the time average spectra were taken to get a first information about the ionization capability of our discharge.

In the Figure 4.2, there are shown the photos taken through the observation windows at argon pressure of 1.2 Pa. On the left photo, the plasma only in the preionization mode (~ 300 V, ~ 4 mA, ~ 1.2 W) is shown. The high power pulses were turned off. The observed red colour of the plasma is characteristic colour of the argon plasma. On the right photo, the superposition of the preionization mode with high power pulses is shown. One can observed, that the red colour of preionization mode is totally cover by the green colour which is characteristic for the plasma burned in copper vapour.

The numerical camera was set to an automatic regime, thus we can not compare the absolute light intensities in these photos because the integration time, di-
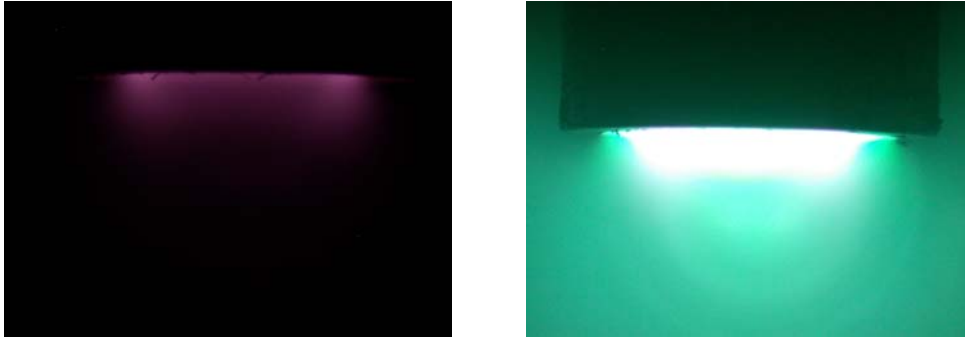
Figure 4.2: Photos of magnetized plasma taken through the observation window. Left photo - preionization mode only, high power pulses turned off. Right photo - superposition of preionization mode with 1 kV pulses of 10 μs length and repetition frequency 30 Hz. Argon pressure was 1.2 Pa.

aphragm etc. were not the same for both photographs. To compare them, the time average spectra in the UV-VIS range of spectra were measured for the same two modes of interest at the same experimental conditions. The intense lines which were easily separated from the others were chosen. In the Figure 4.3, there are shown by black line the representative Ar and Cu atom and ion lines taken in the preionization mode. The same lines taken in the preionized high power pulsed operation are shown by red line in the same figure.

One can observe, that superposing the high power pulses to the preionization, the intensity of Ar atom line is almost unchanged but the intensity of Ar ion line increases by a factor ~ 3. When high power pulses are turned on, the intensity of Cu atom lines increases a lot (~ 10 times) and Cu ion lines appears clearly. The low intensity of Cu atom lines in preionization mode demonstrates the weakness of preionization low current discharge to sputter a lot of material. The material sputtered in the preionization mode is not ionized as can be seen from an absence of Cu ion lines in preionization mode only. But it still contribute to the flux of the neutral atoms to the substrate, which is needed to be as low as possible with respect to the ion flux. To ensure high ionization degree of sputtered material, the preionization needs to be well chosen in order to simultaneously reduce the breakdown delay and does not provide a lot of sputtering itself.

High power pulses induce a high sputtered particle ionization degree, which can not be quantify by optical emission spectroscopy, but can be demonstrated by the presence of many times ionized sputtered species. The Figure 4.4 presents two times ionized copper lines observed during the high power pulse operation. Not only one, but many Cu^{++} lines were found. One can assume that if two times ionized copper atoms are present in detectable quantities, the ionization degree of metallic vapour will be very high during the high power pulsed operation.
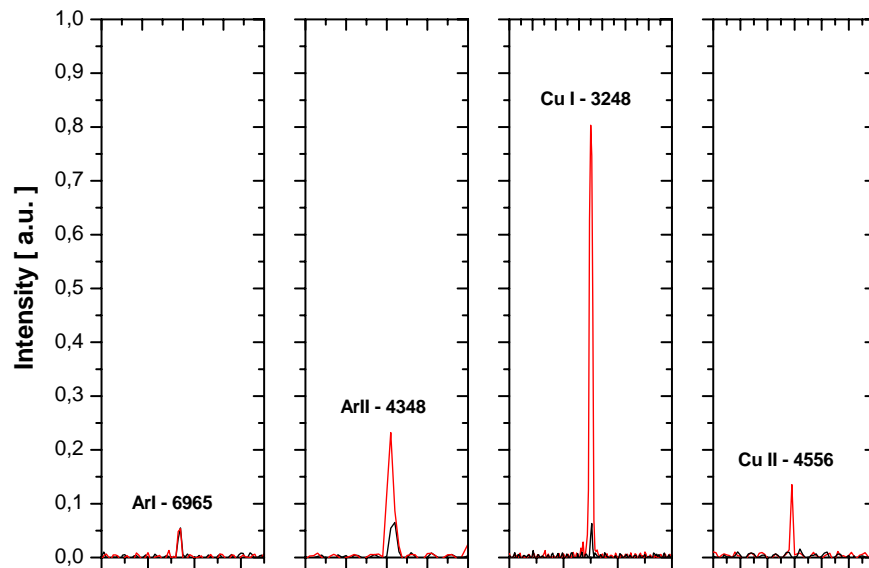
Figure 4.3: An example of time averaged intensity of selected lines taken in the preionization mode (black line) and superposition of preionization with high power pulses (red line). The pressure was 1.2 Pa, mean magnetron voltage 1 kV, pulse duration 10 μs and repetition frequency 30 Hz.
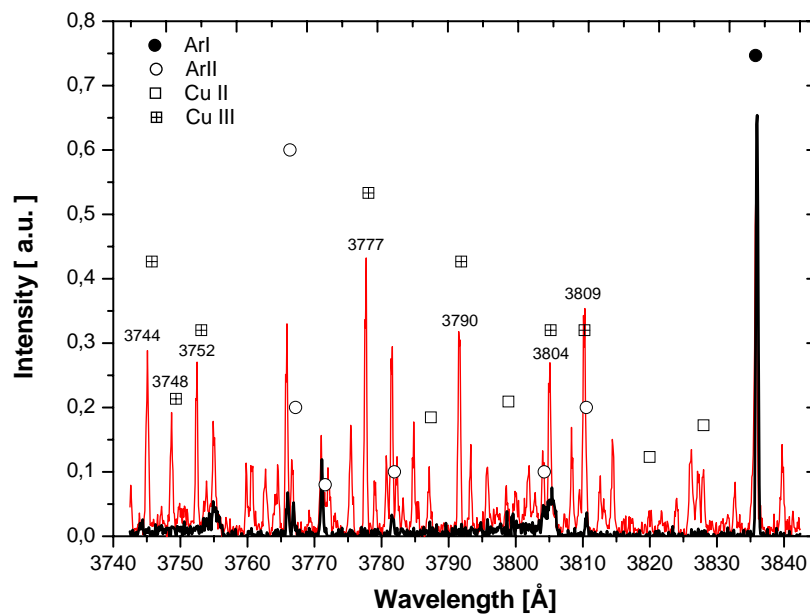

Figure 4.4: An example of time averaged intensity of selected lines in the preionization mode (black line) and superposition of preionization with high power pulses (red line). The spectral region of two times ionized copper lines is shown. The pressure was 1.2 Pa, mean magnetron voltage 1.1 kV, pulse duration 10 μs and repetition frequency 30 Hz.
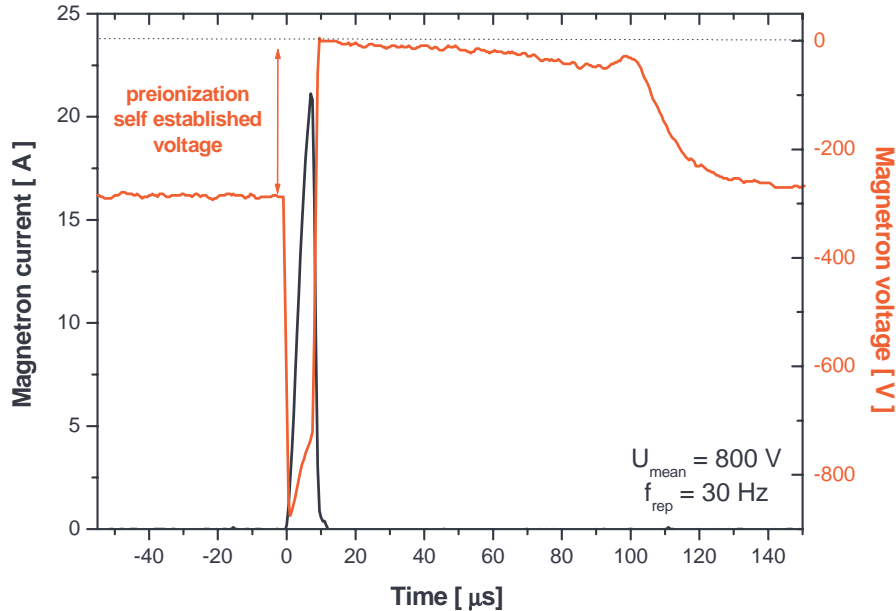
Figure 4.5: Typical time evolution of magnetron voltage and current in our experiment. It was measured at Ar pressure of 2 Pa, repetition frequency of 30 Hz and mean pulsed voltage of 800 V.

4.3.2   Time resolved magnetron voltage and current measurement

In the Figure 4.5, there are shown the typical time dependencies of magnetron voltage and current in our experiment. The characteristics were measured at argon pressure of 2 Pa, mean pulse voltage of ~ 800 V and repetition frequency of 30 Hz. As it was already mentioned, the system allows the superposition of low power DC preionization discharge with high power pulses. The system was designed to ensure before each high power pulse the magnetron current at least ~ 4 mA. Corresponding self-establish voltage on magnetron cathode was in our magnetron device ~ 300 V. When 800 V was applied in pulse regime, we observed from Figure 4.5 that magnetron current rise very steeply. After desired time, the high voltage is stopped and very short magnetron current fall follows. One can observe that it takes a certain time until the same self established voltage as was before the high power pulse is re-established. It is related to the fact, that our system is designed as a current generator and just after the end of the high power pulse, there are still enought charges to provide magnetron current higher than 4
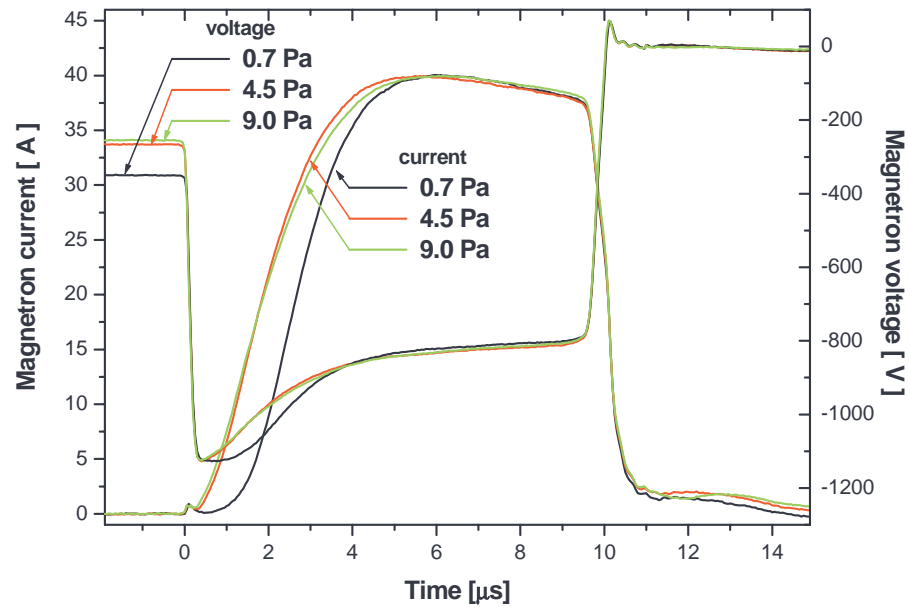
Figure 4.6: Typical time evolution of magnetron voltage and current during the high power pulse as a function of Ar pressure. It was measured at repetition frequency of 30 Hz and mean pulsed voltage of 1 kV.

mA. Hence, there is no need to apply voltage on the magnetron cathode immediately after the end of the high power pulse. At very high repetition frequencies (higher than ~ 10 kHz), the plasma afterglow of the previous pulse could assist as a preionization for the next pulse development and an external preionisation should be needless.

The preionization creates a stable low density plasma near the magnetron cathode. It ensures that the plasma sheath is already established before each high voltage pulse. The presence of the initial plasma sheath provides the fast and reproductive cathode current dynamics when high voltage is applied. Hence, the preionization significantly eliminates breakdown delay and ensure good process stability and reproducibility.

The preionization together with high voltage applied ensures proper current development and it allows to work with very short pulses. Short pulse duration and the short time of switching off significantly reduces the arc formation during the discharge because the plasma does not have time to undergo the transition to the arc discharge even at very high cathode loads. The arcing depends a lot on the cathode purity. For an unclean cathode surface, usually after opening the
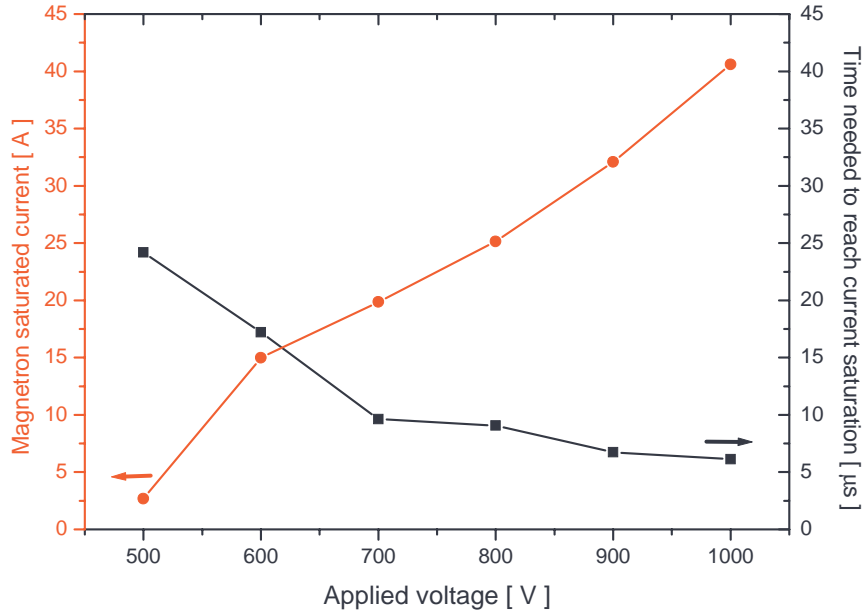
Figure 4.7: Dependence of the magnetron saturated current and time needed to reach them on mean voltage applied during the high power pulse. It was measured at repetition frequency of 30 Hz.

apparatus, first arcs occur at pulse duration of only few μs at 1 kV applied. For a clean cathode and 1 kV applied, the arcs occur rarely only for pulses longer than $\sim 35\ \mu$s.

Typical time variation of discharge current and cathode voltage are reported in Figure 4.6 for three values of the argon pressure and 1 kV applied in pulse regime. Three regimes has been identified. Shortly after the high voltage is applied, the magnetron current does not rise identically for various pressures. It was observed that for times lower than $\sim 2\ \mu$s the current rise is steeper at higher argon gas pressures. After this early regime, there is a transient regime between ~ 2 and $\sim 6\ \mu$s. Particularly at the beginning of this regime the magnetron current rise does not depend on the pressure. At the late part of this regime the magnetron current continues to rise little longer for lower pressures. Finally, for time higher than $\sim 6\ \mu$s, a stationary regime is reached characterized by pressure independent magnetron current of ~ 40 A for average 1 kV applied in pulse regime.

Now, knowing that after a certain time, the pressure independent magnetron current is reached, it could by useful to know, how it depends on the voltage applied on the magnetron cathode during a pulse. In the Figure 4.7, there is plotted

the dependence of the magnetron saturated current I_{sat} and the time τ_{sat} needed to reach it on the average voltage applied on the magnetron cathode during the pulse. It was observed that for average magnetron voltage of 1 kV, saturated pressure independent magnetron current of 40 A was reached in 6 μs. For lower magnetron voltage of 0.8 kV (0.6 kV) lower value of 25 A (15 A) was reached later 9 μs (17 μs).

In the magnetron discharges, the magnetron current is an important parameter related to the sputtering rate of magnetron cathode material. For a given voltage, two times higher magnetron current means two times more of the sputtered material. Power or current densities are other important parameters related to the density of magnetized plasma.

For the argon pressure of $\sim$ 1 Pa and $\sim$ 1 kV of mean voltage applied on the magnetron cathode, magnetron saturated current of $\sim$ 40 A is reached. Corresponding current and power densities are $\sim$ 5 A/cm^2 and $\sim$ 4 kW/cm^2. As the magnetron current does not go through the whole cathode uniformly, almost all the current goes only through the racetrack part of the cathode, the current and power densities are much higher than the values obtained by assuming the whole cathode surface. The racetrack surface was estimated from the width of the racetrack at its half depth. In our case, the racetrack surface is almost the half of the whole cathode surface. Thus, we can specify the current and power densities. The current and power density of $\sim$ 10 A/cm^2 and 8 kW/cm^2 was reached in the racetrack region during the high power pulsed operation.

Power density in a conventional DC magnetron devices is $\sim$ 10 W/cm^2. In our case, we managed to get three order of magnitude higher power density in pulsed regime and keep average power operation comparable to classical DC magnetron devices.

4.3.3 Time resolved optical emission spectroscopy

Temporal evolution of line intensities at Ar and He buffer gas

To understand the behaviour of our fast high power pulsed magnetron discharge, time resolved optical emission spectroscopy measurements were performed. We investigated the time evolution of chosen Ar, Ar$^+$, Cu, Cu$^+$ and even Cu^{++} lines. The experiment was done for many pressures.

The Figure 4.8 shows an example of data processing on the time evolution of very weak Cu^{++} 377.7 nm line. The line intensity evolution (green line) was obtained as a subtraction of measured base line (red line) from measured signal (black line). The base line was obtained at the same conditions as the signal except that the optical fibre was shuttered. The same process was applied to all time resolved line intensity measurements in order to subtract from measured signal
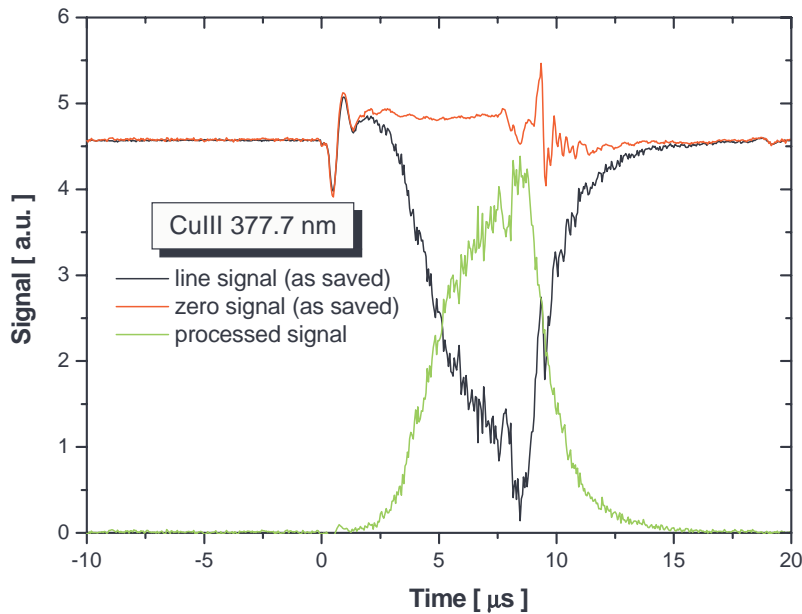
Figure 4.8: Time evolutions of measured signal (black line), baseline signal (red line) and two times ionized copper line intensity (green line) obtained as subtraction of baseline from measured signal. An example of data processing.

an electromagnetic oscillation at the beginning and at the end of the high power pulse.

Figure 4.9 presents the temporal evolution of magnetron current and Ar and Cu atom and ion lines for the pressure of 0.7 Pa and 1 kV applied in pulsed regime. One can observe that Ar atom line appears shortly after the high voltage is applied, a little earlier than Ar^+ line. Cu atom line starts to appear with $\sim 2\,\mu$s delay with respect to the beginning of the pulse. Short time after that, between 2 and 4 μs, Cu atom line increase is stopped for a moment and Ar atom line rapidly decreases. Cu^+ and even Cu^{++} lines appear almost simultaneously, only $\sim 1\,\mu$s later with respect to Cu atom line. For times higher than $\sim 6\,\mu$s, Ar neutral line is dropped, Ar^+ line decreases quickly however Cu^+ and Cu^{++} lines remain nearly constant until the end of the pulse. One can observe, that even at the end of the pulse, Cu atom line does not reach a maximum. Prolonging the pulse duration, the saturation of Cu atom line was observed at time $\sim 14\,\mu$s.

When argon working gas was replaced by helium, similar behaviour was observed. Helium has higher ionization potential, significantly lower mass and better heat conductivity than Ar gas. So it seemed us interesting to compare these two gases.

Figure 4.9: Time evolution of magnetron current and chosen line intensities of Ar (696.6 nm), Ar$^+$ (434.8 nm), Cu (521.8 nm), Cu$^+$ (204.4 nm) and Cu^{++} (377.7 nm). Argon pressure was 0.7 Pa, 1 kV was applied in pulse regime with repetition frequency of 30 Hz.

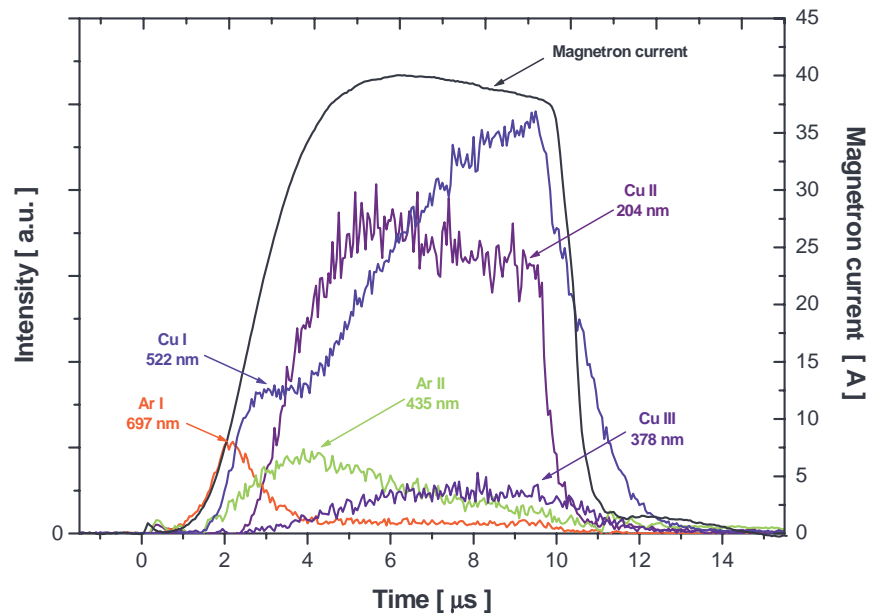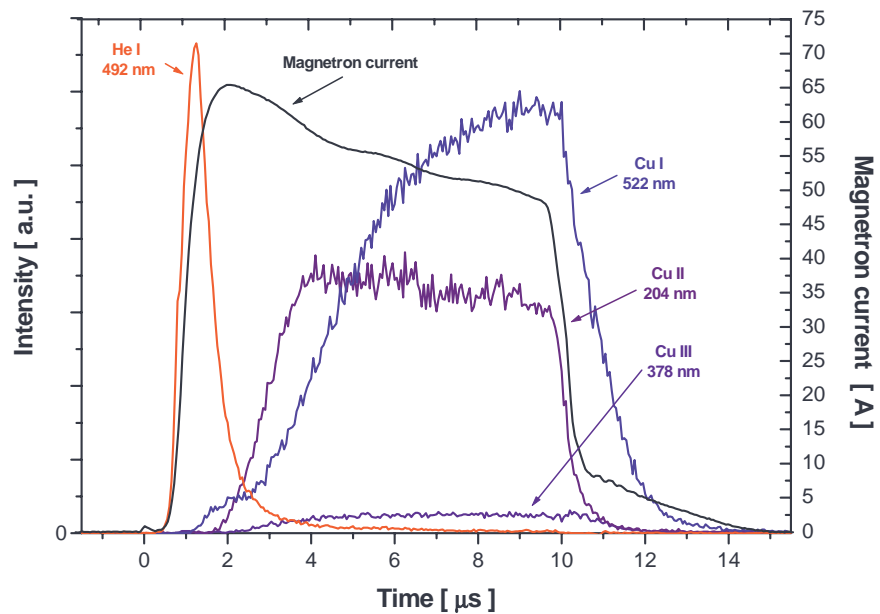Figure 4.10: Time evolution of magnetron current and chosen line intensities of He (492.2 nm), Cu (521.8 nm), Cu$^+$ (204.4 nm) and Cu^{++} (377.7 nm). Helium pressure was 8 Pa, 1 kV was applied in pulse regime with repetition frequency of 30 Hz.

The experiment was performed at helium pressure of 8 Pa. It was the lowest pressure at which a stable discharge was ignited. The discharge ignited at lower pressures was often unstable hence, these experimental conditions were avoided. It was not studied in detailed, but it seems us, that the preionization current was not stable at low helium pressures.

One can observe at Figure 4.10, that He line behaves identically to Ar line, it rises steeply and shortly after the moment, when Cu line appears, it starts to decrease. Time behaviour of Cu line intensity is very similar to the case of argon working gas. The same flat region at the beginning of the pulse is observed. Cu^+ and Cu^{++} lines reach saturated value for time $\sim 4\ \mu$s, Cu line saturates later. It can be concluded that replacing the Ar working gas by He, similar phenomena and a little faster discharge dynamic were observed.

Temporal evolution of line intensities at various Ar pressures

In Figure 4.11, there are plotted temporal evolution of magnetron current, magnetron voltage and Ar and Cu species intensities for Ar pressure of 0.7, 4.4 and 9.0 Pa. Let us emphasize the most significant changes in the magnetron electrical characteristics and line evolutions with pressure change.

As was discussed previously the time evolutions of magnetron current can be divided in three stages. In the early stage (t $<$ 2 μs) the current rise strongly depends on the buffer gas pressure. Lower pressure means slower current rise. Particularly at the beginning of the transient regime magnetron current rise does not depend on the pressure. At the late part of this regime, magnetron current continues to rise little longer for lower pressures. But finally the stationary regime (t $>$ 6 μs) is reached and magnetron current reaches always the same pressure independent value. These characteristic times are for magnetron voltage of $\sim$ 1 kV applied in pulsed regime Decreasing the magnetron voltage lower pressure independent saturated current is reached later as has been already shown in Figure 4.7.

In the early stage of the discharge fast magnetron current rise is followed by steep rise of Ar line. As magnetron current increases earlier and faster with increasing pressure, Ar line increases earlier and faster too. Shortly after the moment of Cu lines appearance, Ar line starts to decrease. For higher pressures, it happens earlier and the characteristic maximum of Ar line is observed at higher pressures earlier too. For all studied pressures, we can conclude, that Ar line drops in favour of Cu line. The low argon line intensity observed for times higher than $\sim 4\ \mu$s could not come from the active discharge but maybe mainly from the plasma afterglow. The measurement was done through the observation window and all the light, from the discharge and from a part of the afterglow was collected and led to the monochromator slit.

Contrary to the shift of Ar line maximum with increasing pressure toward the beginning of the pulse, Ar^+ line maximum shifts toward the end of the pulse.
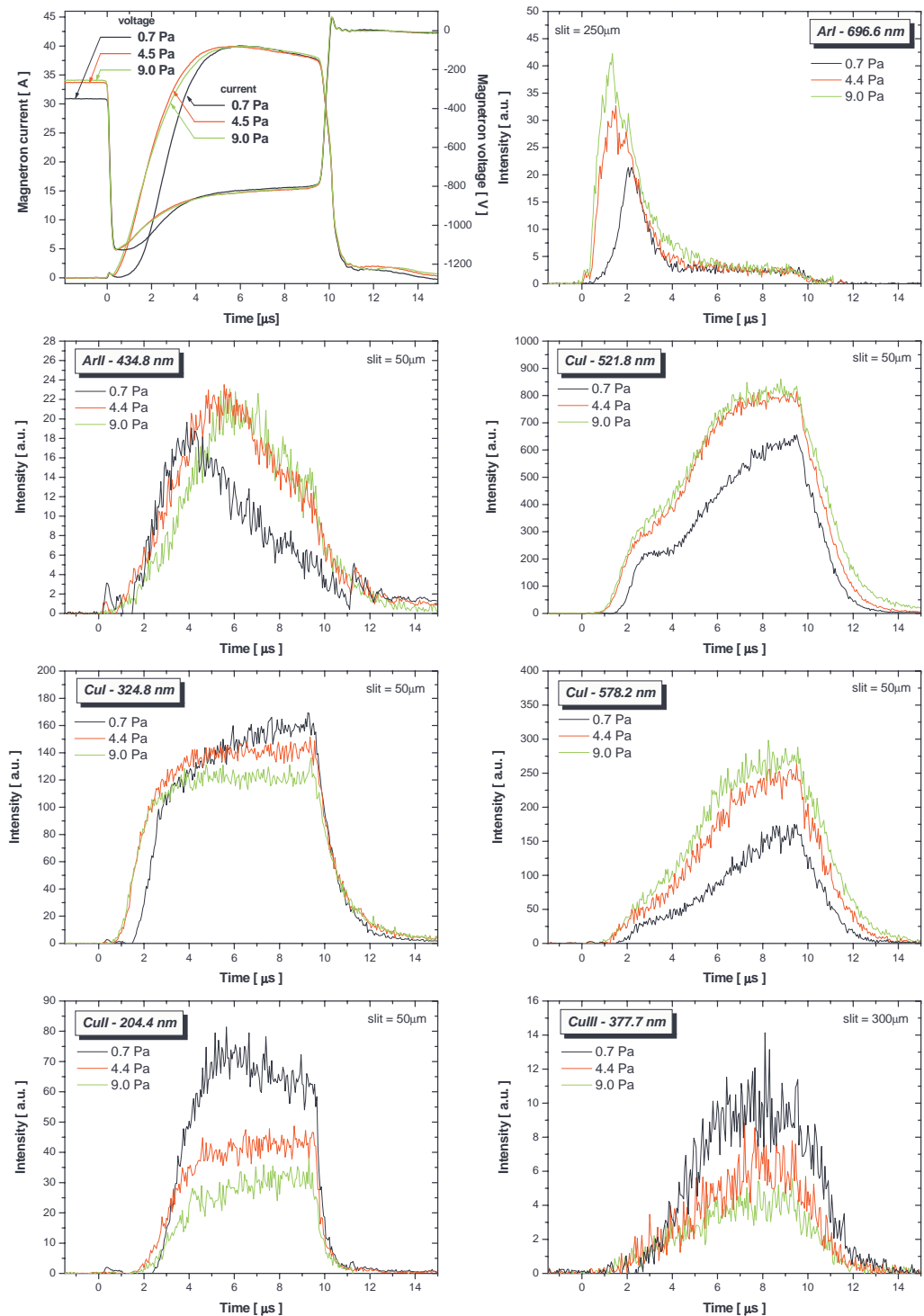
Figure 4.11: Time evolution of magnetron current, voltage and chosen line intensities of Ar (696.6 nm), Ar$^+$ (434.8 nm), Cu (324.8, 521.8 and 578.2 nm), Cu$^+$ (204.4 nm) and Cu^{++} (377.7 nm). Argon pressure was varied from 0.7 to 9.0 Pa, 1 kV was applied in pulse regime with repetition frequency of 30 Hz.
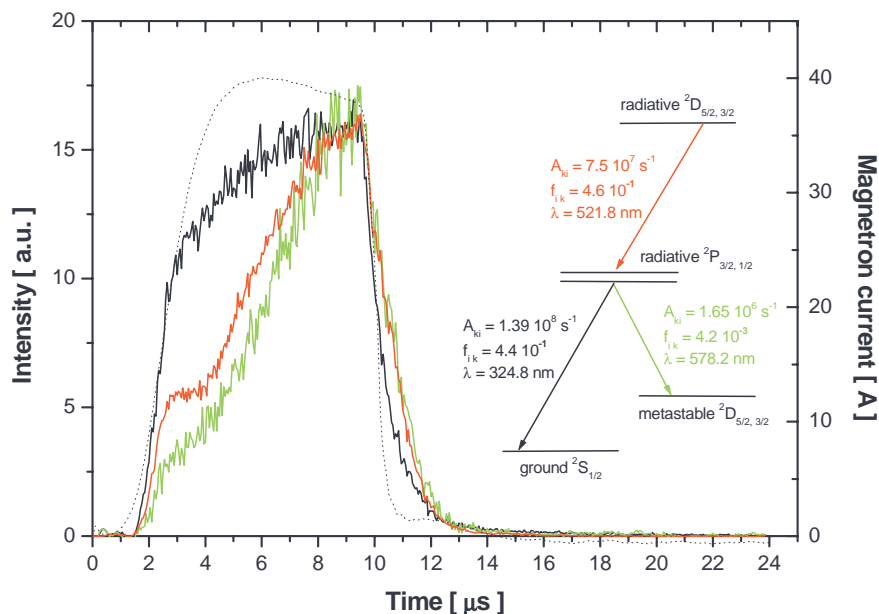
Figure 4.12: Time evolution of magnetron current and chosen line intensities of Cu (324.8, 521.8 and 578.2 nm). Argon pressure was 0.7 Pa, 1 kV was applied in pulse regime with repetition frequency of 30 Hz.

One can observe, that all studied Cu lines (324.8 nm, 521.8 nm and 578.2 nm) appear at the same time. For higher pressures, they appear earlier. In the early stage of the discharge, the only difference in their time evolution is that the lines obtained at 9 Pa are shifted of about 1 μs toward the beginning of the pulse with respect to them obtained at 0.7 Pa. The same shift can be observed at the magnetron current time evolution. The magnetron current obtained at pressure 9 Pa is shifted of about 1 μs with respect to the one for 0.7 Pa too. We can conclude that in the early stage of the discharge the time shift of Cu lines evolution corresponds well to the time shift of magnetron current.

Despite that all studied Cu atom lines appear at the same time and behave similarly in the early stage of the pulse, for times higher than ~ 2 μs they start to differ. The Cu 324.8 nm line tends to saturate very quickly, however the Cu 521.8 and 578.2 nm lines continue to rise practically until the end of the pulse. Increasing the pressure, all lines tend to saturate faster. The Cu 324.8 nm line reaches the maximal intensity at the lowest pressure, however the Cu 521.8 and 578.2 nm lines at the highest pressure. This behaviour was not expected because both lines 324.8 and 578.2 nm, which behave differentially, appear due to depletion of the

same upper level of a copper atom. At the Figure 4.12, time evolutions of all studied Cu line intensities observed at pressure 0.7 Pa are merged together. Their intensities are scaled to fit the figure. The schema of energy levels from which these lines originate together with Einstein coefficients and oscillator strengths was added on the right side of the figure. One can observe that Cu 521.8 nm line behaves more similarly as the Cu 578.2 nm line despite the fact that they do not rise from the same upper level. The Cu 324.8 nm line which rises from the same upper level as 578.2 nm behaves differently from the rest of the lines. We think, that the difference is probably caused by significant self-absorption of this line because of very high oscillator strength and/or high density of sputtered copper ground state atoms due to high magnetron current operation.

Returning back to the Figure 4.11 one can observe that characteristic flat region between 2 and 4 μs at the time evolution of 521.8 line is the most evident at low pressure. Increasing the pressure, it is less evident. Similar behaviour, but less visible shows the Cu 578.2 nm line evolution too.

Intensities of all studied Cu^+ and Cu^{++} lines behaves similarly in the pressure range we investigated. Both saturate for times higher than 6 μs. Increasing the pressure, lower saturated value is reached.

4.4 Discussion

Let us comment in detail the different stages of our preionized high power pulsed magnetron discharge. These stages were identify from the temporal evolution of magnetron current and voltage and from time resolved optical emission spectroscopy, which were shown in previous section of this chapter.

Before the high voltage pulse, system generates a low preionization current $\sim$ 4 mA. Corresponding self-established voltage is about $\sim$ 300 - 350 V depending on the pressure. This current comes from stable, low density plasma near the magnetron cathode. The plasma consists mainly of Ar ions and electrons, because no line intensity of copper ion was observed, when high power pulses were turned off. Only a very low intensity of copper atom line was detected. It makes us conclude that only a little amount of easy excited copper atoms were present. The preionization plasma provides a plasma sheath already established before applying the high voltage pulse. The presence of the plasma sheath ensures the fast and reproductive cathode current dynamics when high voltage is applied.

At desired time, the high voltage is applied directly on the magnetron cathode. The ions coming from preionization plasma are attracted to the cathode at high quantities. They sputter the copper atoms and knocks the secondary electrons, which are injected without significant delay to the magnetized region. They are trapped there by magnetic field and creation of new electron-ion pairs follows.

Argon atom line intensity copies at the initial stage of the discharge the magnetron current. Argon excited states are created by electron impact and the excitation rate is directly proportional to the electron density. Magnetron current is proportional to the density in magnetized plasma too, because argon ions are extracted from the plasma contributing to the magnetron current. From denser plasma, more ions can be extracted. Both magnetron current and argon line intensity are proportional to the density of magnetized plasma, and so, it is not surprising that both behaves same.

Increasing the pressure, the argon ionization and excitation collision frequencies in magnetized plasma increase too and both, magnetron current and argon line intensity rise more steeply. At higher pressure, an electron injected to the plasma loses its energy earlier in favour of creation of new electron-ion pairs. It accelerates the discharge dynamics.

Shortly after the beginning of the pulse, first Cu atom lines appear. This delay can be caused by the fact that Cu atoms, sputtered from the cathode surface are not excited in the magnetized plasma immediately. A cumulative probability of a sputtered Cu atom going through the magnetized plasma to be excited will depend on its resident time in the plasma. From the photograph presented in Figure 4.2, the plasma thickness was found to be ~ 5 mm. The velocity of the sputtered copper atoms ranges from a very low values up to few tens km/s. The most probable velocity of a sputtered copper atom is ~ 5 km/s [2]. The time in the range of $\sim 1\ \mu$s is needed to transport first sputtered Cu atoms from the cathode to the remotest parts of magnetized plasma. During this time, the travelling copper atom may be excited. Increasing the pressure, magnetron current is shifted toward the beginning of the pulse and significant amount of Cu atoms is sputtered earlier. Consequently, they arrive to the magnetized plasma, where they are excited earlier too. It explains, why the difference in the appearance time of Cu lines and their evolution in the early stage of the discharge corresponds well to the evolution of the magnetron current.

For times lower than $\sim 2\ \mu$s, plasma is formed mainly by buffer gas species. Despite the fact that till $\sim 4\ \mu$s magnetron current still increases and consequently both plasma density and sputtered copper atom flux arriving to the plasma increases too, in the time between 2 and 4 μs, Cu 521.8 line increase is stopped for a moment and argon line intensity rapidly decreases. This Ar line originates from the upper ^{4}P state of Ar atom, which is mainly populated by direct electron excitation from Ar ground state. The cross-section for this process is very narrow making excitation of this state very sensible on the changes in the tail of electron energy distribution function. The observed time variation of this Ar line can be explained by very fast electron cooling induced by an important amount of sputtered Cu atoms arriving into magnetized plasma. A fast and intense cooling of the electrons can explain the observed flat region in the time evolution at Cu 521.8 nm

line too. First copper atoms sputtered during the pulse enter to the plasma which in mainly formed by argon gas species and thus characterised by relatively high electron temperature due to high excitation and ionization energy levels of Ar atom. Cu has significantly lower excitation and ionization energy levels than Ar. It means that excitation and ionization of Cu atoms will be favoured and the Cu line intensities will rise steeply. Consequently, electron energy distribution function (EEDF) will be modified towards the lower energies with respect to the one at the early stage of the discharge. The argon atoms excitation rate decreases and the excitation of the copper atoms arriving to the magnetized plasma just after the first huge packet of copper atoms will be reduced. The argon lines will decrease and Cu lines may show a shoulder in their time evolution. After a certain time, needed to establish a new steady state electron energy distribution function, Cu 521.8 nm line will continue to increase due to the simultaneous increase of copper atom and electron densities however Ar lines will keep their low intensity. Other studied Cu line, such as 324.8 nm and 578.2 nm, will be less affected by changes of EEDF due to the lower excitation energy of the states, from which they originate.

Cooling of electrons will be more faster at higher pressures, where the discharge dynamics is faster. Faster magnetron current increase causes higher copper atom flux arriving to the plasma. More copper atoms will faster modify the electron energy distribution function. It will cause that at higher pressures, the flat region at Cu 521.8 nm line will be observed during shorter time and will be less pronounced.

Cooling of the electrons could explain why, for all studied pressures, Ar line maximum is linked together with appearance time of Cu lines and both are shifted towards the beginning of the pulse with increasing pressure.

Moreover, huge amount of sputtered Cu atoms and reflected Ar neutrals collides with buffer gas atoms, shares a part of their kinetic energy with them, increases the gas temperature in magnetized region and pushes the buffer atoms out from the magnetized region. In conventional DC magnetron discharge, buffer gas density is reduced significantly even at low current operation. For direct current density of ~ 200 mA/cm^2 and Ar pressure of 4 Pa, gas density was reduced ~ 5 times at the distance of 5 cm from magnetron cathode [36]. In the case of pulse regime, it is difficult to quantify the gas rarefaction effect. One can assumed, that during the discharge on time, gas will be intensively rarefied in the magnetized region due to high current operation and during discharge off time, buffer gas density will increase because atoms will return back from a perimeter.

During the high power pulsed operation, it is difficult to distinguish the main excitation mechanisms of the upper ion energy level from which studied line originates. It can be two step process of consecutive ionization and excitation or one step simultaneous ionization and excitation. It makes the situation difficult because one does not know, which ground state - if of argon atom or of argon ion -

is concern.

The buffer gas rarefaction effect could be observed at the behaviour of Ar^+ 434.8 nm line and can explain higher Ar^+ line intensity at higher pressures. It was observed that for times higher than $\sim 6\,\mu$s a steady state regime was reached characterized by pressure independent magnetron current and voltage. Assuming that plasma density and electron energy distribution function are almost pressure independent at this regime, the only explanation in pressure behaviour of the Ar^+ 434.8 nm line is that the amount of Ar species (neutral and/or ions) is different. At higher pressure, higher intensity was observed. It could mean, that at higher pressures, the density of residual Ar species (neutrals and/or ions) is higher. It is only incomplete information, we are not able to estimate the absolute densities. However it is reasonable to assume the residual argon atom and/or ion density to be very low.

For times higher than $6\,\mu$s, pressure independent magnetron current was reached and Cu^+ and Cu^{++} line intensities reached a steady state value. As the magnetron current does not depend on the Ar pressure, one can conclude that the plasma is formed mainly by Cu ions which dominate over Ar ions and that mainly these Cu ions contribute to the magnetron current. Such situation is called self-sputtering regime [5]. We suppose that for times higher than $6\,\mu$s, transition between buffer gas discharge and a discharge sustained in copper vapour has been already passed. This transition was associated with the falling of Ar^+ line investigated in magnetron plasma simultaneously with a transition toward the stable Cu^+ and Cu^{++} emission and pressure independent magnetron current.

After the transition to the metallic vapour sustained discharge the stable self sputtering regime is achieved which is consistent with current densities of ~ 10 A/cm^2 and power densities of ~ 8 kW/cm^2 (averaged on the cathode racetrack) which is about two orders of magnitude higher than those reported for self sputtering operation. The possibility to reach sustained self sputtering by using the direct current magnetron source of different material is well described in detail in [5]. The threshold power densities for copper target ~ 80 W/cm^2 [37] and threshold current densities ~ 200 mA/cm^2 [38] were estimated. In the high power pulsed magnetron discharges, the peak power densities are at least one order higher than that in the dc magnetrons and the plasma process naturally tends toward the self-sputtering. In our experiment, the times needed to obtain sustained self-sputtering regime is very short and approaches the self-sputtering cycle duration [39] which was estimated to be $\sim 1\,\mu$s. We can emphasize that we obtain a fast dynamics of the pulsed magnetron discharge (copper target, 4 kW/cm^2) with time characteristics one order shorter than previously reported by [32] (titanium target, ~ 2.8 kW/cm^2) and [19] (copper target, ~ 0.5 kW/cm^2). The self sputtering regime is generally convenient regime for sputtering due to high copper ionization degree despite the fact that copper ions participate on the sputtering.

These ions are lost, but the material is not lost, because the sputtering ion will stick on the cathode being ready to be sputtered and return back to the plasma, of course as neutral. For more detail about self-sputtering operation, see Figure 2.3 and accompanying text in chapter 2.

It was observed, that copper atom 521.8 and 578.2 nm lines (which did not suffer from significant self-absorption) tend to reach a steady state value after $\sim 14\ \mu$s, far later after the current saturation was reached. The stationary state of Cu lines can be achieved only after a certain time, needed for copper atoms to fill the whole volume of magnetized region, where they are excited. As neutral species, they can leave the magnetized region freely. The only way how to make the copper atoms to stay in plasma and occupy the whole magnetized plasma volume is through the collisions with the species in magnetized region. Without any collision, they will continue to move away from the plasma with their initial velocity ~ 5 km/s originated from a sputtering process. It can explain, why a certain time is needed for Cu line to reach the saturation. Increasing the pressure favoured the collisions and Cu 521.8 and 578.2 nm lines reached stationary state earlier.

4.5 Conclusion

We advanced currently used high power pulsed magnetron sputtering technique by using a preionization to significantly reduce the breakdown delay and to accelerate the discharge dynamics.

This preionization maintains stable low magnetron current in the order of few mA between two successive pulses. The preionization current comes from a stable, low density plasma near the magnetron cathode. It ensures a plasma sheath already established before each high power pulse. It significantly reduces the breakdown delay and provides very good process stability and reproductibility.

Our system provides the reproductive and fast magnetron current rise when high voltage is applied. It allows to reach a high power operation in few μs and consequently to reduce the pulse duration. The short pulse duration avoids the arc formation even at very high cathode load of ~ 10 A/cm^2 and ~ 8 kW/cm^2. The average power set by pulse duration and repetition frequency was kept at moderate ~ 10 W/cm^2 which is a value compatible with classical DC magnetron devices.

In the Ar buffer gas, the maximum pressure independent current of ~ 40 A was reached in 6μs, when 1 kV was applied on the copper magnetron cathode of 33 mm in diameter. The high cathode load in pulsed regime was accompanied by observation of spectral lines of two times ionized copper atoms indicating very high ionization degree of sputtered particles.

Time resolved diagnostics were performed for pulse duration of 10 μs, which

was pulse long enough to cover all important stages of discharge evolution.

The shift at the early stage of the discharge between the time evolution of Cu atomic lines and the magnetron current has been found to be $\sim 1\,\mu s$ and pressure independent. It well corresponds to the time, needed to transport the sputtered copper atoms from the cathode, where they are sputtered through the magnetized plasma, where they are excited.

The drop of Ar lines originated from upper ^4P level together with the occurrence of the flat region in Cu 521.8 nm line was associated with the fast changes of electron energy distribution function due to the huge amount of copper atoms arriving to the magnetized plasma.

It has been observed, that at the beginning of the pulse, the plasma is dominated by Ar ions and as time elapses, metallic ions are detected and they outnumber very quickly the argon ions. We associated this transition with the falling of Ar^+ line simultaneously with the passage towards the stable Cu^+ and Cu^{++} emission and pressure independent magnetron current. Gas-metal plasma transition takes place only $\sim 6\,\mu s$ after the beginning of the pulse which is at least one order faster transition than was already reported in literature.

By changing the pulse duration, from a few μs up to about $50\,\mu s$, it is possible to choose the proportion of self-sputtering regime on the overall sputtering process. The pulse duration can be adapted in order to avoid the arc formation even at unusually high power densities. It was shown, that an arc free self-sputtering is possible to maintain.

Chapter 5

Transport of Sputtered Particles and Trench Filling

5.1 Introduction

The potential of high power pulsed magnetron sputtering has created growing interest, because it can generate a dense plasma with high target material content.

One issue reported recently [40] is a reduced deposition rate compared to the conventional DC deposition rate at the same average power. These lower deposition rates in high power pulsed magnetrons of only about 25-35 % of the deposition rates of convention DC magnetrons may be an issue for many already working industrial application.

Additionally, the ionized fraction of the target material arriving at the substrate is lower than might be expected. Observed fraction of $\sim$ 30 % positive Cr ions [34] and $\sim$ 70 % positive Cu ions [18] near substrate was reported.

To understand all the processes taking place in the deposition chamber, it is important not only to focus on the plasma composition and the discharge dynamics, but at the same time to study the processes taking place between the plasma and the substrate. A high metal ionization degree in the magnetized plasma need not to mean the same high metal ionization degree near the substrate. The deposited thin films could not have expected high quality.

In this chapter, our attention will be focused on the study of the ion transport using a simple system, similar to them used by [32]. To measure a saturated ion current, a moveable negatively biased substrate holder was used as a planar Langmuir probe. The influence of the process parameters (magnetron voltage, pressure, distance from the magnetron cathode, pulse duration and repetition frequency) on the amount of ions collected on the substrate is shown in section 3 and discussed in section 4 of this chapter. Particular attention is devoted to the study of a plasma
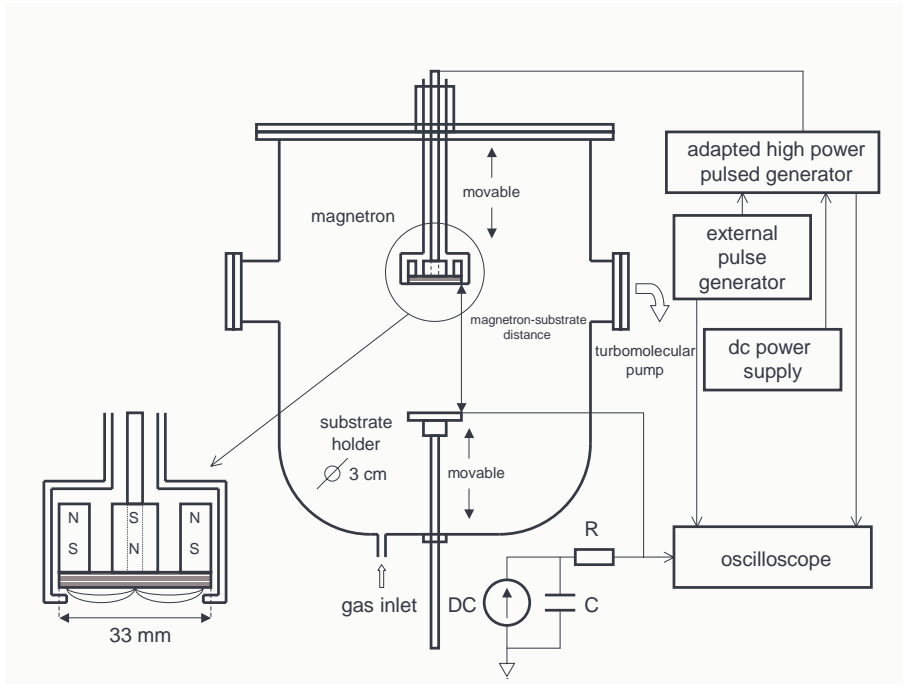
Figure 5.1: Schema of the experimental set-up

de-confinement and to the transition toward the sustained self-sputtering regime. In the section 5, industrial potential of our system is tested on the filling of 2 μm trenches and vias of aspect ratio 1.

5.2   Experimental set-up

The apparatus, shown in Figure 5.1, is the standard planar magnetron source Mighty Mac-130-STD_E, which has been already described in the Chapter 4. It operates with a copper target (99.9% purity) of 33 mm in diameter. The cathode is located inside a stainless-steel chamber of radius R = 220 mm and height L = 350 mm. The chamber is pumped by a turbomolecular pump backed by a rotary pump down to the pressure of 10^{-3} Pa. Argon is used as a buffer gas. The pressure is varied from 0.5 to 10 Pa by gas flow (from 1 to 15 sccm) and by an exhaust throttle valve.

A home made adapted pulse generator was developed in cooperation with Dr. Mihai Ganciu. The generator allows the superposition of the low power DC preionization discharge ($\sim$ 4 mA, $\sim$ 300 V) and high voltage pulses applied directly on the magnetron cathode.
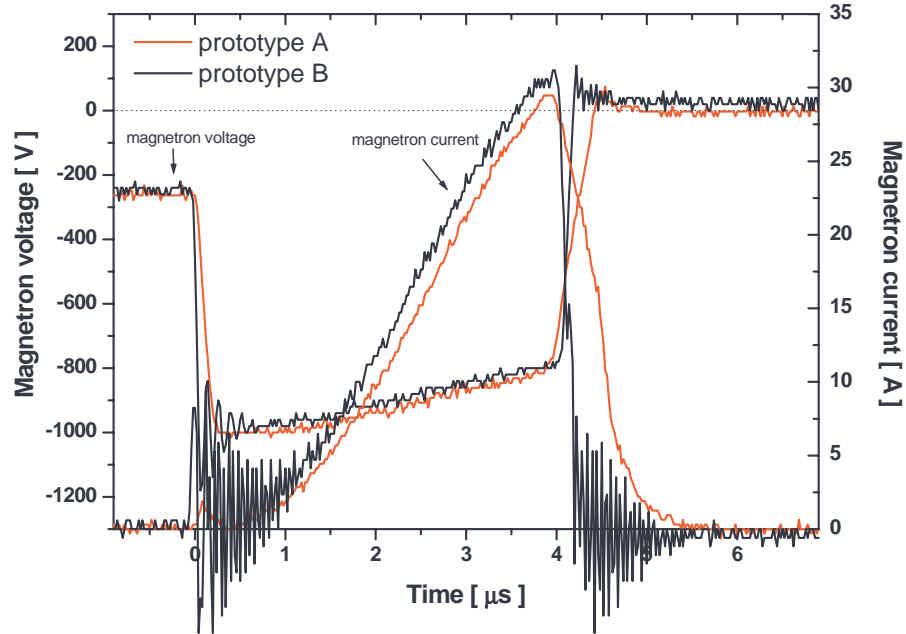
Figure 5.2: Typical time evolution of magnetron current and magnetron voltage during the high power pulse operation with prototype A and B. The pressure was 1.4 Pa, repetition frequency was 30 Hz and 1 kV was applied in pulsed regime.

The system was designed to ensure a fast rise and a sharp drop of the magnetron current. Pulse duration was varied from 1.5 μs to 55 μs. The highest repetition frequency about 600 Hz was used only in the case of very short pulses.

The current and voltage probes were integrated directly into the pulse generator system and calibrated by a classical commercial voltage and current probe. The maximum magnetron current corresponding to 1 kV applied in pulse regime was 40 A.

Ion saturated current measurements were performed using a movable substrate holder with a diameter of 30 mm. It was used as a flat Langmuir probe and biased by a system allowing $\sim$ 10 ns time resolution. The probe was positioned at the distances of 40-100 mm from the magnetron cathode along the central axis. The time resolved ion saturated substrate holder current was recorded by 100 MHz digital Tektronix TDS 340A oscilloscope at fixed negative substrate holder bias voltage -60 V to repel the electrons. The signal was synchronised with the beginning of the voltage pulse applied on the magnetron cathode.

During the deposition samples were placed on the biased substrate holder placed at a desired distance from magnetron cathode.

The experiments described in this chapter were performed by using two prototypes (let us call them A and B) of the adapted pulse generator. The results discussed in previous chapter and trench filling described in section 5 of this chapter were obtained with the prototype A, which was the first one developed in LPGP. The saturated substrate holder current measurements, shown in section 3 and discussed in section 4 of this chapter were obtained with the prototype B which was developed later. Prototype B was advanced with respect to A in order to ensure faster switch-off of the magnetron current.

The typical time variations of the magnetron current and voltage obtained by these two power supplies operating at the same experimental conditions are shown in Figure 5.2. One can observe, that in the case of prototype B, magnetron voltage is applied faster and magnetron current rise is little steeper. After the end of the voltage pulse, magnetron current relaxes $\sim$ 3 times faster with the prototype B than with A. It drops from $\sim$ 30 A to 15 A in 0.5 μs with prototype A and only in 0.15 μs with B.

5.3   Influence of the process parameters on the amount of ion collected on the substrate

5.3.1   Influence of the pulse duration

The simple and direct way, how to study the influence of the pulse duration on the amount of ions collected on the substrate, is to prolong the magnetron pulse and to observe the ion saturated substrate holder current change. To perform this study correctly, it is necessary to assure that at least following two conditions are satisfied. The first condition is, that the prolonged magnetron pulse must copy the shorter one in their common part. If it is not assured, one can not distinguish, if observed changes in substrate holder current are due to prolonged part of the pulse, or due to the changes in the common part of the reference and the prolonged pulse. The second condition is, that the magnetron current fall must be as fast as possible after the end of the pulse. The fast fall time of the magnetron current will reduce the role of the post-discharge on the substrate holder current, which may not be the same for the pulses of different durations.

In the Figure 5.3, there are shown the typical dependencies of magnetron and substrate holder current for two pulse durations: 2 and 2.5 μs. One can easily observe, that the first 2 μs of the 2.5 μs magnetron current pulse is the same as the 2 μs magnetron current pulse. Moreover, the pulse generator, which allows very short magnetron current and voltage fall time, was used. This significantly reduced the role of plasma afterglow on ion saturated substrate holder current. It implies that the two previously defined conditions were well fulfilled and that the
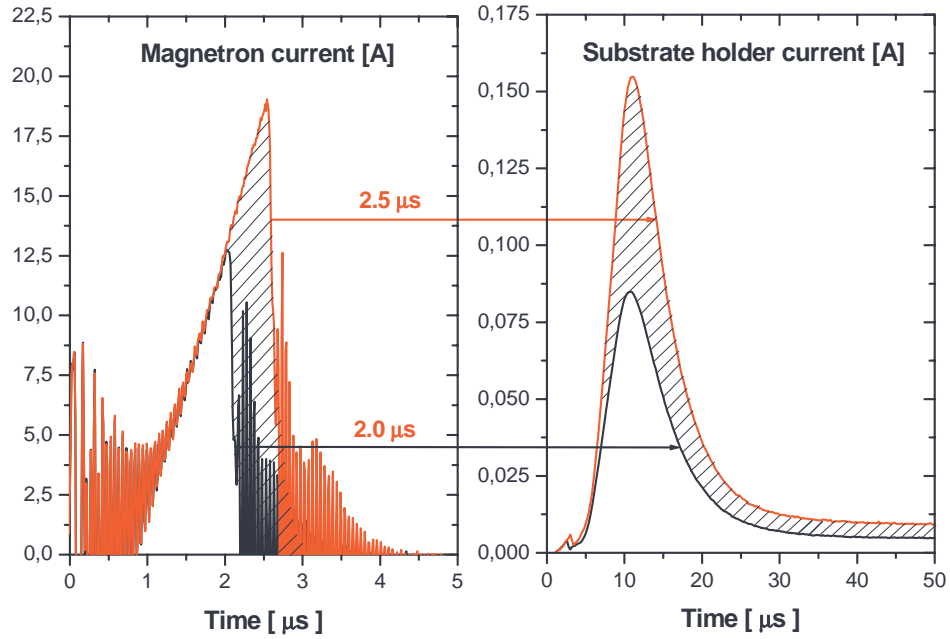
Figure 5.3: Time evolution of magnetron and ion saturated substrate holder current for two pulse durations: 2 and 2.5 μs. The pressure was 1.4 Pa, -60 V biased substrate holder was placed at the distance of 4 cm from magnetron cathode, 1 kV was applied in pulsed regime.

hatched difference between substrate holder currents for 2 and 2.5 μs magnetron current pulse comes mainly from the last 0.5 μs of the 2.5 μs pulse. The area between these curves represents the number of ions collected on the substrate holder due to the prolongation of magnetron high power pulse from 2 to 2.5 μs.

In the Figure 5.4, there are plotted the time evolutions of magnetron current obtained at Ar pressure of 1.4 Pa, repetition frequency of 5 Hz and 1 kV applied in the pulse regime. The pulse duration varied from 1.5 to 8 μs. The corresponding substrate holder currents measured at the distance of 4 cm from magnetron cathode are shown in Figure 5.5. Pulse durations are labelled in the figure. Figures 5.6 and 5.7 show the substrate holder currents measured at the distance of 6 and 8 cm from the magnetron cathode. They will be discussed in the next section, now we focus only on the Figure 5.5. One can observe, that the substrate holder current does not copy the magnetron current. The shape of magnetron and substrate holder current is different. For all pulse durations, the maximum of substrate holder current is always observed with a certain delay of ~ 7 μs with respect to the end of the magnetron pulse. This time delay indicates a transport of the ions from the magnetized region toward the substrate.
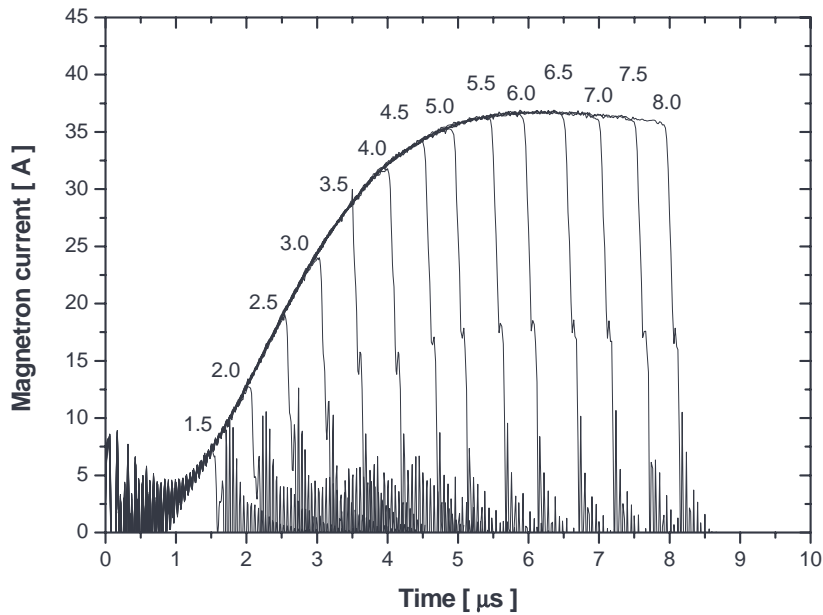
Figure 5.4: Time evolutions of magnetron current. The pulse duration ranges from 1.5 μs to 8 μs. Pressure was 1.4 Pa, repetition frequency 5 Hz and 1 kV was applied on magnetron cathode in pulse regime.

Figure 5.5: Time evolutions of substrate holder current measured at the distance of 4 cm from the magnetron cathode for the magnetron pulses described in Figure 5.4. Pulse durations are labelled.
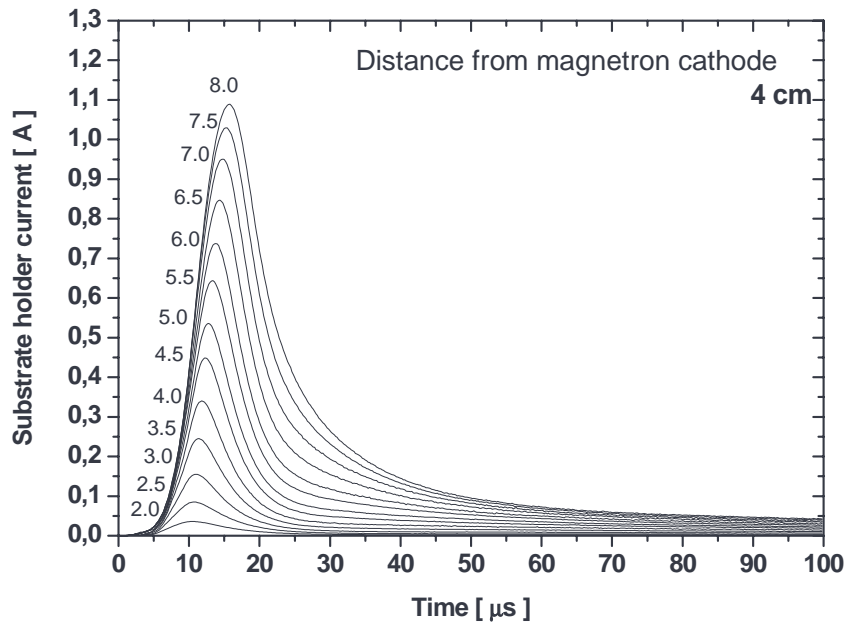
Figure 5.6: Time evolutions of the substrate holder current measured at the distance of 6 cm from the magnetron cathode for the magnetron pulses described in Figure 5.4. Pulse durations are labelled.

Figure 5.7: Time evolutions of the substrate holder current measured at the distance of 8 cm from the magnetron cathode for the magnetron pulses described in Figure 5.4. Pulse durations are labelled.
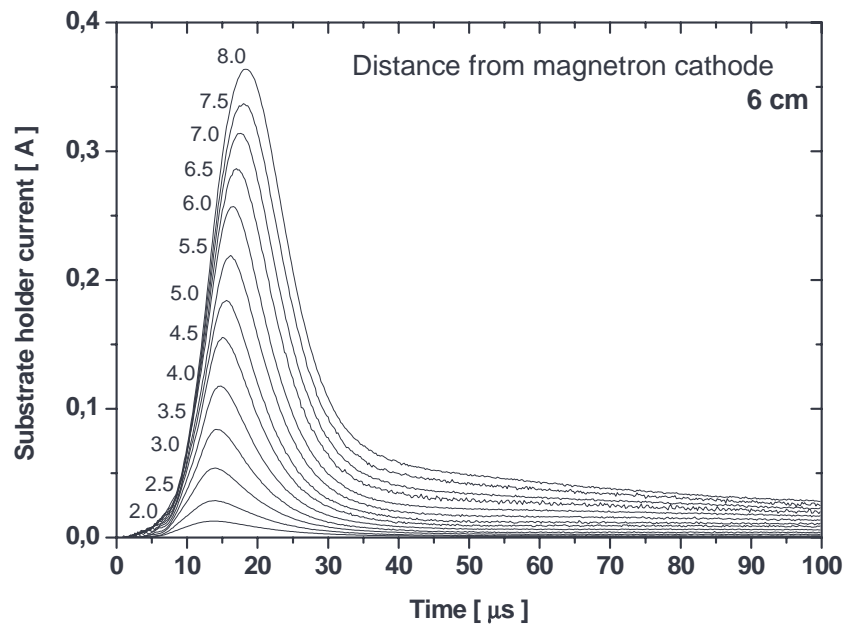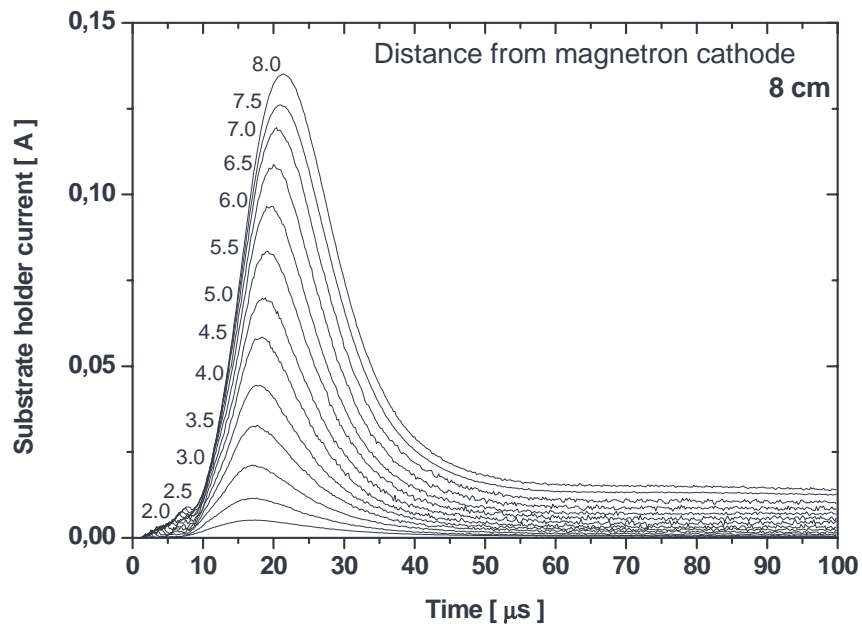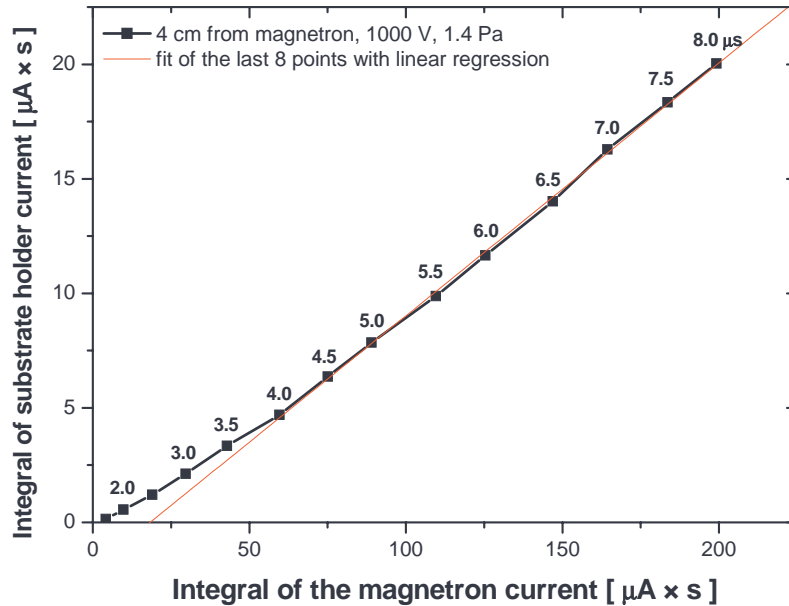
Figure 5.8: Dependence of the integral of substrate holder current recorded at the distance of 4 cm from magnetron cathode on the integral of magnetron current. Each point represents a pulse duration which is labelled in the figure. Pressure was 1.4 Pa, repetition frequency 5 Hz and mean voltage of 1 kV was applied in pulsed regime.

If we assumed that the maximum of the substrate holder current originates always from the latest part of the magnetron pulse, the ~ 7 μs, needed for copper ions to cross the distance between the magnetized plasma and the substrate holder gives a transport velocity ~ 6 km/s. This value is very close to the average velocity of a sputtered copper atom.

One can observe that for 8 μs pulse, the substrate holder current maximum is ~ 1 A at the distance of 4 cm from the magnetron cathode. It gives the substrate holder current density in the range of ~ 100 mA/cm^2. For 20 μs pulse, even higher maximum substrate holder current of about 6 A was reached corresponding to extremely high substrate holder current density ~ 600 mA/cm^2. This value, obtained by high power pulsed sputtering is much larger than that of about < 1 mA/cm^2 and 2-10 mA/cm^2 reported by [3] for conventional DC sputtering using balanced or unbalanced device respectively. Note, that our magnetron is well balanced according to manufacturer's certification and hence the reference value for DC sputtering is rather that < 1 mA/cm^2. One can conclude, that even with

very short pulses of $\sim 2\,\mu$s, we are able to have an important substrate holder current density in the range of ~ 10 mA/cm^2, significantly higher than that obtained with the DC magnetron sputtering.

In the Figure 5.8, we deduced the dependence of the integral of substrate holder current on the integral of magnetron current. Each point represents a different magnetron pulse duration, which is labelled in the figure. Integral of the substrate holder current corresponds to the amount of ions collected on the substrate holder during one period (during the magnetron pulse and between two succeeding pulses). Integral of the magnetron current is proportional to the number of ions bombarding the cathode during a pulse.

One can observe that at the distance of 4 cm from the magnetron cathode, for argon pressure of 1.4 Pa and 1 kV of mean voltage applied on the magnetron cathode, we detect an important amount of ions. The integral of substrate holder current is about 10 percents of the integral of the magnetron current.

One can notice, that the dependence is not exactly linear. In the first part, for times lower than $\sim 4.0\,\mu$s, it increases less than linearly. For pulse durations larger than $\sim 4.0\,\mu$s, it changes behaviour and the dependence becomes linear.

5.3.2 Influence of the distance, pressure, magnetron voltage and repetition frequency

In the Figure 5.4, there are plotted the time evolutions of magnetron current obtained at Ar pressure of 1.4 Pa, repetition frequency of 5 Hz and mean magnetron voltage of 1 kV applied in the pulse regime. The pulse duration varied from 1.5 to 8 μs. The corresponding substrate holder currents measured at the distance of 4, 6 and 8 cm from the magnetron cathode are shown in Figures 5.5, 5.6 and 5.7 respectively. Pulse durations are labelled in each figure.

One can observe, that moving away from the magnetron cathode, lower maximal current is observed later. At the distance of 4 cm (6 cm or 8 cm) from the magnetron cathode, maximum of substrate holder current is always observed with a certain delay of $\sim 7\,\mu$s($\sim 10\,\mu$s or $\sim 13\,\mu$s) with respect to the end of the magnetron pulse. Using the same reflection as few paragraphs above, the transport velocity of ~ 6 km/s can be found. This value is independent on the distance from the magnetron cathode and corresponds well to the mean velocity of a sputtered copper atom. It seems clear now, that the maximum of substrate holder current corresponds to the sputtered, non thermalized atoms, which were ionized during their passage through the magnetized plasma.

From the Figures 5.5, 5.6 and 5.7, one can observe that the peak of the magnetron current corresponding to non thermalized ions broads with the distance from the magnetron cathode and that the tail of the substrate holder current be-
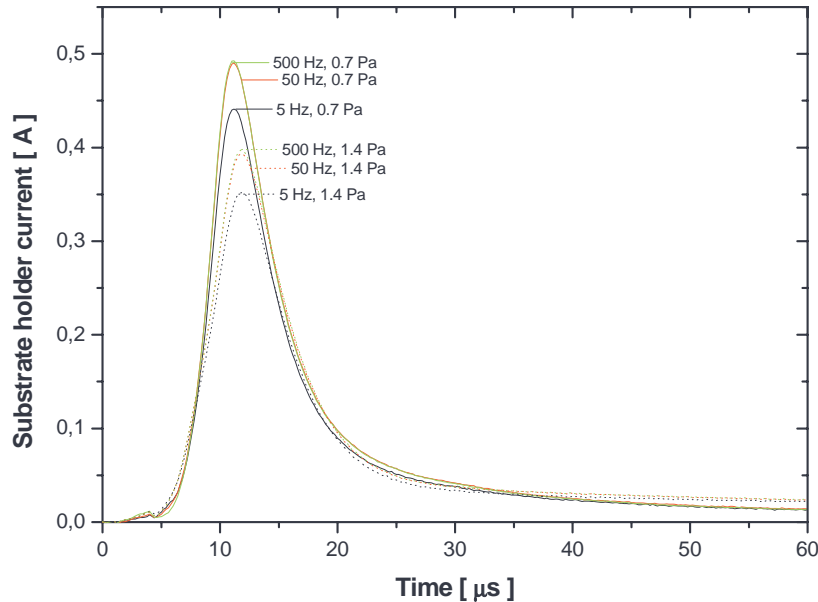
Figure 5.9: Time evolutions of the substrate holder current measured at the distance of 4 cm from the magnetron. Pulse duration was 4 μs, mean magnetron voltage was 1kV. Other experimental condition, such as pressure and repetition frequency are marked in the figure.

comes more important at higher distances from the magnetron cathode. At higher pressures, peak of non thermalized ions broads more with distance from the magnetron cathode too.

In the Figure 5.9, there are shown the substrate holder currents measured at the distance of 4 cm from the magnetron cathode for pulse duration of 4 μs, two Ar pressures and three repetition frequencies. Increasing of repetition frequency from 5 to 50 Hz increases the substrate holder current of $\sim$ 10 percents, however increase of repetition frequency from 50 to 500 Hz keeps the substrate holder current almost unchanged.

In the Figures 5.10 and in detail in the Figure 5.11, there are reported the results of several experiments. Similarly as in Figure 5.8, we deduced the dependence of the integral of the substrate holder current on the integral of the magnetron current. Each point represents a magnetron pulse duration and each curve particular experimental conditions. For the same integral of the magnetron current, it is observed that higher pressures, higher distances from the magnetron cathode or lower magnetron voltages result in less ions collected on the substrate.

Figure 5.10: Dependence of the integral of substrate holder current on the integral of magnetron current. Each point represents a pulse duration and each curve particular experimental condition. For one curve, pulse durations are labelled, for others, only the last point is marked by pulse duration.
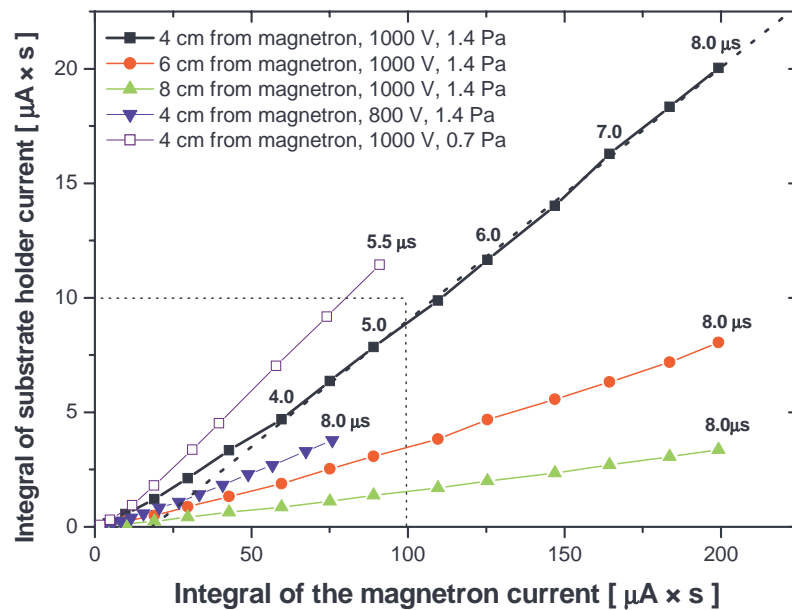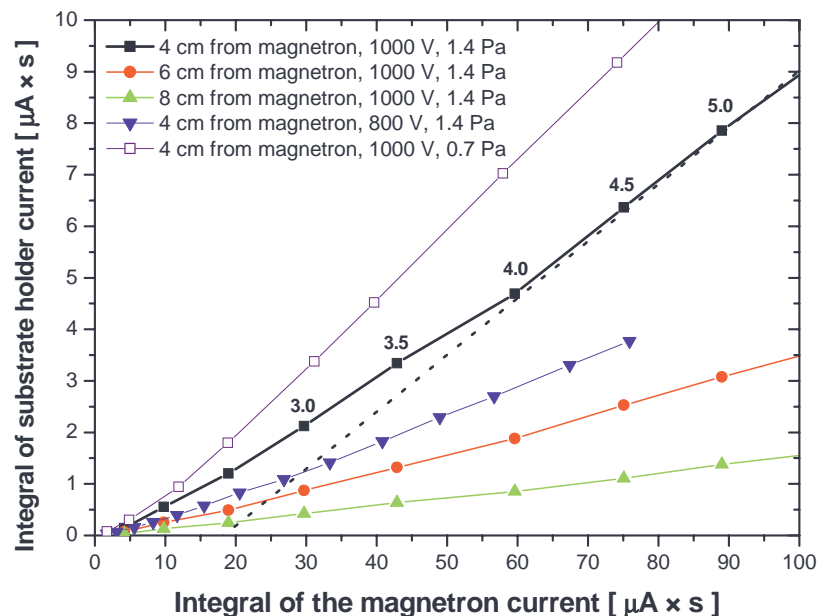

Figure 5.11: Dependence of the integral of substrate holder current on the integral of magnetron current. Each point represents a pulse duration and each curve particular experimental condition. For one curve, pulse durations are labelled. This figure is a zoom of the Figure 5.10.

Distance[cm]	Voltage [kV]	Pressure [Pa]	i
4	1.0	1.4	9
6	1.0	1.4	23
8	1.0	1.4	56
4	0.8	1.4	19
4	1.0	0.7	8

Table 5.1: Parameter i, amount of ions bombarding the cathode needed to get an ion more at the substrate at various experimental conditions.

At all studied experimental conditions, the dependency behaves similarly. In the first part, the increase is non linear and from a certain time, the integral of substrate holder current becomes almost linear function of the integral of magnetron current. It happens at the time $\sim 4\mu$. It seems, that this time does not depend on the distance from the magnetron cathode and on the Ar pressure.

Parameter i, amount of ions bombarding the cathode needed to get an ion more at the substrate, can be simply derived as the inverse value of the slope of linear dependencies shown in Figure 5.10. It makes it independent on the pulse duration contrary of the substrate holder current density, which increases with the pulse duration due to the overlap of the current originated from various pulse stages. It could be a good marker to quantify simultaneously the ionization and the transport of sputtered particles. It is reported together with the corresponding experimental conditions in the Table 5.1. One can observe, that there is only a small dependency on the pressure. It has been found in the previous chapter, that after a certain time from the beginning of the pulse, magnetron current is independent on the pressure. Thus, the small increase of i with pressure is probably due to an increase of loss processes between the magnetized plasma and the substrate holder. The fast decrease of i with increasing voltage applied during the pulse on the magnetron cathode is probably associated with low impedance behavior of magnetron discharge. Increasing the magnetron voltage from 0.8 to 1 kV, magnetron saturated current increases from 25 A to 40 A (see Figure 4.7) and i decreases from 19 to 8.

5.4   Discussion

A metallic particle taking part on the deposition process should start at the cathode surface and finish at the substrate. Live of an ion collected at the substrate holder can be split into five elementary processes, one coming after another.

First, a neutral atom is sputtered. This process is characterised by a sputtering yield γ which depends on the applied magnetron voltage and the incident ion

nature. After that, neutral atom goes through the plasma where it can be ionized mainly by an electron impact. In the high power pulse operation, the Penning ionization in the plasma can be neglected [4]. The probability of a neutral to be ionized depends mainly on the resident time of a neutral inside the plasma, on the electron temperature and on the electron density and therefore on the magnetron current too.

Then, ions have to leave the magnetised region. The ions are not confined by external magnetic field as the electrons. The radius of curvature (Larmor radius) for a 100-eV electron (100-eV Ar ion) in magnetic field of 0.01 T is $\sim$ 0.3 cm ($\sim$ 66 cm). However, important ion current to the substrate requires the space charge compensation of the ions by electrons in the area between the target and the substrate. Usually it is achieved by unbalanced magnetron [3], where the magnetic field configuration facilitates the transport of charged particles. It could be achieved by a secondary plasma presence between the magnetized plasma and the substrate too. The secondary plasma could re-arrange itself to provide the charge compensation of the flux of ionized sputtered particles. Since our magnetron is according to manufacturer's certification well balanced and no other secondary plasma, between the magnetron and the substrate is present, other processes have to be looked for.

At low pressures, after an ion leaves the magnetized plasma the ballistic transport with a velocity associated to the ejection velocity follows. After first collision with a buffer gas atom, which not only changes the preferred particle momentum but changes its kinetic energy too, thermalization start. At the end the ion taking part on the deposition, arrives to the substrate, where it is detected.

Let us focused now on the role of various process parameters on the integral of saturated ion substrate holder current. The dependency on the distance from magnetron cathode, on the magnetron voltage and on the Ar pressure is shown in Figure 5.10.

When the substrate holder is moved away from the magnetron cathode, lower amount of ions is collected. Moving away from the cathode, solid angle for ion collection decreases and at higher distances, ion losses due to scattering collisions are more important. Both lead together to a decrease of detected ion current on the substrate. Reducing the working pressure, the loss processes due to scattering collisions are reduced and more ions can arrive on the substrate.

Let us quantify by a very simple model, how many ions leaving the magnetized region are not detected on the substrate due to its finite surface. In this model, a symmetry with respect to the central axis was assumed. Two point source of ions in the racetrack region, each located 8.5 mm from the central axis was assumed. The angular distribution of sputtered atoms was described by a cosine distribution function, which is accurate to first order for most situations [2]. The transport of sputtered particles was assumed to be pure ballistic. It was assumed, that ion-

ization event takes place only in the magnetized region and does not change the momentum of sputtered particles. Ionized sputtered atom simply hits the substrate holder or misses it and then continues directly to the wall. It was predicted, that the fraction of the ionized sputtered particles collected on the substrate is about 50, 25 and 20 percents of all ionized sputtered particles leaving the magnetized plasma for the case of the substrate holder located at the distance of 4, 6 and 8 cm from the magnetron cathode respectively. This simple model predicts decrease of ionized fraction of sputtered particle flux by factor 2 when substrate holder is moved from 4 to 6 cm from the magnetron cathode and by a factor 1.3 when it is moved from 6 to 8 cm.

As was discussed previously, the first peak at the time evolution of substrate holder current corresponds to the flux of non thermalized ionized sputtered particles. For 8 μs pulse, it decreases from 154 mA/cm^2 at the distance of 4 cm from magnetron cathode to 51 and 19 mA/cm^2 at the distance of 6 and 8 cm respectively. The relative decrease between 4 and 6 centimeters by factor 3 and between 6 and 8 centimeters by factor 2.7 was derived experimentally. The losses calculated in previous paragraph due to the decrease of solid angle for ion collection gives only factor 2 and 1.3. That means that there still remains a factor of 1.5 between 4 and 6 centimetres and a factor 2 between 6 and 8 centimeters to explain. It is probably related to the scattering losses due to collisions with buffer gas atoms.

Reducing the magnetron voltage results into the decrease of an amount of ions arriving to the substrate. Integral of the substrate holder current at the same integral of the magnetron current decreases by a factor ~ 1.7 when magnetron voltage was reduced from 1000 to 800 V. Lower voltage applied on the cathode results in lower sputtering yield and consequently lower sputtered particle flux. At the same time, a secondary electron will at lower magnetron voltage enter to the plasma with lower energy and consequently, a lower production of electron-ion pairs in the gas phase could be expected. Observed decrease by a factor ~ 1.7 could be explained by the cumulative effect of the drop of sputtering yield (only ~ 10 percents) and the decrease of the ionization efficiency.

The variation of the substrate holder current with repetition frequency shown in Figure 5.9 can be explained by buffer gas rarefaction between the magnetized plasma and the substrate holder. A huge amount of sputtered particles moving from magnetized plasma towards the substrate collides with buffer gas atoms. It results in simultaneous scattering of sputtered particles and partial removing of buffer gas atoms from the area between the target and the substrate. At very low repetition frequency (few Hz), the buffer gas atoms return back during the discharge off time (hundreds ms) to scatter the sputtered particles and to be partially removed during the succeeding pulse. However, at higher frequencies (tens or hundreds Hz), the buffer gas can only partially return back during the discharge off-time (tens or even few ms) and the buffer gas density will be then significantly

lower between the target and the substrate at the beginning of a pulse. Less scattering collision will take place at higher frequencies than at lower and consequently, the substrate holder current collected during a period will be higher at higher repetition frequencies. Note that obtaining higher ion saturated current during a period at higher repetition frequency need not to mean an increase of ionization fraction of total particle flux to the substrate. The ions and neutrals are probably scattered by the same way.

Few paragraphs above, it has been found that the maximum of substrate holder current decreases between 4 and 6 centimetres by the factor 1.5 and between 6 and 8 centimetres by the factor 2 probably due to scattering collisions. This factor increases with the distance from the magnetron cathode. It could signify that the buffer gas is not homogeneously rarefied in the area between 4 and 8 centimetres from the magnetron cathode, where the study was performed.

Plasma de-confinement

At high plasma temperature and/or plasma density, the plasma kinetic pressure might disturb the magnetic field of the magnetron. A parameter β, defined as the ratio of the plasma kinetic pressure p_{kin} (density of charged particles kinetic energy) at the point inside the plasma, to the confining magnetic field pressure p_{mag} (magnetic energy density) at the plasma boundary, is usually [41] introduced as a measure of the relative magnitudes of the kinetic and magnetic pressures. It is defined as

$$\beta = \frac{p_{kin}}{p_{mag}} = \frac{p_e + p_i}{p_{mag}} \tag{5.1}$$

where the p_e and p_i represents the electron and ion contribution to plasma kinetic pressure. Assuming a homogeneous non curved magnetic field of magnitude B the magnetic field pressure can be derived from equation

$$p_{mag} = \frac{B^2}{2\mu_0} \tag{5.2}$$

To complete the Equation 5.2, it remains to estimate the plasma kinetic pressure. Usually, in the hot plasma physics field [41] the β parameter is introduced as

$$\beta = \frac{n_e k T_e + n_i k T_i}{B^2/2\mu_0} \tag{5.3}$$

where n_e, n_i, T_e and T_i are electron and ion densities and temperatures.

It is clear that the parameter β characterises the relative importance of the plasma pressure versus the magnetic pressure. For $\beta \ll 1$ the plasma pressure has a small effect on magneto-hydrodynamics equilibrium and the magnetic field

structure is approximately that determined from the vacuum magnetic field repre-
sentation and the plasma is well confined. In the opposite limit $\beta \gg 1$ where the
plasma pressure is much larger than the magnetic pressure, in general the plasma
'pushes the magnetic field around' and carries it along with its natural motion.

In DC magnetron discharges, the β factor is in the range $10^{-6} - 10^{-3}$, and
the plasma will not significantly affect the magnetic field distribution. In the high
power pulsed magnetrons having densities of several order of magnitude higher
than in DC case, the kinetic pressure could reach the magnetic pressure and high
density plasma can influence the magnetic field configuration and can not be more
confined by the external magnetic field [33].

Equation 5.3 gives for typical magnetic field used in a magnetron of ~ 0.02 T,
mean kinetic energy of ionized part of sputtered vapour of ~ 3 eV, electron tem-
perature of ~ 3 eV the minimum magnetron current density ~ 3.4 A/cm^2 at which
the plasma kinetic pressure overreaches the magnetic pressure. Magnetron current
density was related to plasma density by Equation 2.4, where m_i was substituted
with the mass of copper ion assuming the self-sputtering regime.

Thus we can suppose that at higher cathode current densities such as that of
~ 10 A/cm^2 obtained in our case, the plasma could be probably de-confined and
may expand with the velocity driven by the ionized part of sputtered particles.

In the magnetron devices, the magnetic field is inhomogeneous, curved and
decreases with the distance from the cathode. It makes the estimation overesti-
mated, because the electrons will be de-confined primarily in the weakest parts
of magnetic field which are mainly the area of field disturbances. The plasma
kinetic pressure is proportional to the density of charged particles and their mean
energy while the magnetic pressure is proportional to B^2. One can expect that dur-
ing the high power operation, there are some regions, where the plasma reaches
high enough density to not be confined anymore. Then, the plasma can be leaved
and continue toward the substrate holder with an average velocity driven by the
ionized part of the sputtered particles. It well correspond to velocity ~ 6 km/s
determined experimentally.

We are not sure, that this is the main mechanism leading to plasma expansion
and unusually high ion substrate holder current densities. Let consider described
phenomenon of the plasma de-confinement as a suggestion, which has not been
yet experimentally verified. Study of the transport of ionized species in a reactor
operated with highly dense magnetized plasma will continue in LPGP in order to
get more information and to understand better this complicated problem.

Transition to self-sputtering regime

The term self-sputtering was used in several reports [5, 37, 38] which describe the
sputtering of metals using ions of the same elements.

It was shown in [39] that the self-sputtering is an important process in magnetron high current density operation. An upper limit for a magnetron current density which can be reached without self-sputtering can be estimated by the kinetic gas equation assuming high ionization degree of buffer gas and that only Ar ions contribute to magnetron current

$$n_i < n = \frac{p}{kT} \tag{5.4}$$

Using $p = 0.1$ Pa ant $T = 300$ K, we obtain density of ions n_i lower than density of buffer gas atoms $n = 2.4 \times 10^{13} \text{cm}^{-2}$. Putting this to equation 2.4, one gets upper current density limit ~ 1 A/cm^2. Due to the heat transfer from sputtered and by cathode reflected particles to neutral background atoms, the gas temperature is higher, and therefore, at given constant pressure, the density of neutrals and consequently the upper magnetron current density limit will be lower than the estimated value. However, in our case, very high current density operation was reached. It signifies that ionized sputtered particles contribute to the magnetron current together with argon ions. A self-sputtering must take place.

The self-sputtering regime is stable only for the metals with high self-sputtering yield. Others, with low self-sputtering yield, will suffer at high current density operation very quickly from a lack of charged particles to sputter the cathode and to create the secondary electrons. In this case, stable high power self-sputtering operation is impossible to maintain the plasma.

Due to magnetron current densities of ~ 10 A/cm^2 higher than of ~ 200 mA/cm^2 those reported by [5] as minimum current densities for copper self sputtering operation, our system will tend very quickly towards self-sputtering regime.

Let us now examine the temporal transition from usual sputtering by Ar ions to stable self-sputtering in high power pulse operation. As soon as the sputtered copper atoms are injected into the magnetised plasma the electron energy distribution function is modified in the sense to decrease the Ar ionization. The important amount of sputtered and by cathode reflected particles shares a part of their kinetic energy via collisions with buffer gas. It increases the temperature of argon gas and reduces the argon gas density. Both processes (Ar rarefaction and T_e decrease) lead to an increase of the ratio of copper to argon ions. It will continue until the stable self-sputtering regime is reached.

Let us estimate by a very simple model a minimum time t_f, needed to reach a stable self-sputtering regime. It could be reasonable to assume that the stable self-sputtering regime will be reached when the copper ions fill the whole volume of magnetized plasma and significantly outnumber the argon ions. It leads to estimate the t_f as the minimum time needed to fill the magnetized region by copper ions.

Let simplify the situation and assume that no copper ion leaves the magnetized region toward the substrate or toward the magnetron cathode until the stable self-sputtering is reached. That means that till the time t_f only Ar ions participate on the sputtering process, which will be described by sputtering yield γ. The magnetized region is filled by copper ions, which represent the α part of the sputtered copper atom flux. The number of copper ions needed to fully fill the magnetized plasma is $n_e V$, where V is the volume of an homogeneous and quasineutral plasma. This volume was assumed to equal the product of the racetrack surface and the plasma thickness d. Equation

$$n_e V = \frac{I}{q} \gamma \alpha t_f \qquad (5.5)$$

allows us to estimate t_f.

At the time t_f, electron density n_e equals the density of copper ions $[M^+]$. Substituting $[M^+]$ from Equation 2.4 to n_e from Equation 5.5 one find

$$t_f = \frac{d}{0.61 \gamma \alpha \sqrt{\frac{kT_e}{m_{Ar}}}} \qquad (5.6)$$

Note, that in this model, t_f does not depend on the plasma density or on magnetron current.

The minimum value of $\alpha \sim 0.4$ to maintain the stable self-sputtering regime can be derived from consideration done by [5]. The sputtering yield for a 1 kV Ar ion bombarding a copper surface is ~ 2.5 as can be found in [29]. The electron temperature was assumed to be ~ 3 eV and the plasma thickness ~ 0.5 cm was approximately estimated from the photographs shown in Figure 4.2. Using these values, the minimum time to fill fully the whole magnetized region by copper ions is about 3 μs. The transition time of a very fast pulsed magnetron discharge to the stable self-sputtering operation could be expected to be only little higher than ~ 3 μs this value.

It coincides well with the experimentally estimated time ~ 6 μs. It was estimated in previous chapter from optical emission spectroscopy (Cu$^+$ lines reach a steady state value, Ar$^+$ lines decrease) and magnetron current measurement (the pressure independent magnetron current is reached). The closeness of these two values proves the hypothesis discussed in previous chapter about very fast dynamics and fast transition to self-sputtering operation of our preionized high power pulsed magnetron discharge operated with a copper target.

Copper ion flux equality in a stable sustained self-sputtering regime

In any stationary regime, the plasma density does not change. It means that the fluxes of ions leaving the plasma equal the fluxes of ions arriving to the plasma.

The creation of electron-ion pairs in the plasma volume can be included to this balance of a virtual flux of ions arriving to the plasma. In stable sustained self-sputtering regime, one can assume that the fluxes of copper ions leaving the plasma equal the ionized fraction of sputtered particle flux.

Comparing the copper ion flux leaving the plasma towards the magnetron cathode Φ_1 and towards the substrate Φ_3 with the ionized α part of the sputtered particle flux $\Phi_2 = \Phi_1\gamma_s\alpha$ (where γ_s is a self-sputtering yield) one find the relation

$$\Phi_3 = \Phi_1(\alpha\gamma_s - 1) \tag{5.7}$$

At the substrate holder, we detect only a part of the Φ_3 depending mainly on the distance from the magnetron cathode and on the pressure. At higher distances from magnetron cathode, the solid angle for ion collection decreases. At higher pressures, losses induced by the scattering with buffer gas atoms are more important.

In a steady state self-sputtering regime α and γ_s should be unchanged. Then, according to Equation 5.7, the flux of copper ions leaving towards the substrate holder will be linearly dependent on the flux of copper ions on the cathode. Consequently, the integral of ion saturated substrate holder current will depend on the integral of magnetron current linearly too.

It could explain the observed linear dependence of the integral of substrate holder current on the integral of magnetron current shown in Figure 5.8, 5.10 and 5.11. If it is so, one can conclude that for 1 kV applied in the pulse regime and argon pressure 1.4 Pa, the self sputtering regime was reached at time $\sim 4~\mu$s. From optical emission spectroscopy and magnetron current measurements, the transition time to stable self-sputtering regime was situated to $\sim 6~\mu$s. At this time, magnetron current was pressure independent and copper ion lines already reached the saturation. At the time $\sim 4~\mu$s, magnetron current is not exactly, but almost pressure independent and copper ion lines tend toward the saturation very quickly (see Figure 4.11). In conclusion, these results coincide well.

When magnetron current increases, the density of magnetized region increases too and therefore the ionized fraction of sputtered particle flux must be greater than the flux of the copper ions leaving toward the target and the substrate. In this case, Φ_3 will not be linked with Φ_1 linearly.

Moreover, the formula 5.7 may be used for a crude estimation of the ionized fraction of the sputtered particle flux. It was observed that at the distance of 4 cm from the magnetron cathode and argon pressure of 0.7 Pa, the integral of substrate holder current is about 15 percents of the integral of the magnetron current. Assuming that all ions leaving the magnetized plasma are collected by the substrate and for the self-sputtering yield of ~ 2.5, the ionized fraction of the sputtered particle flux $\alpha \sim 0.5$ is found. This is, of course, a crude and underrated value.
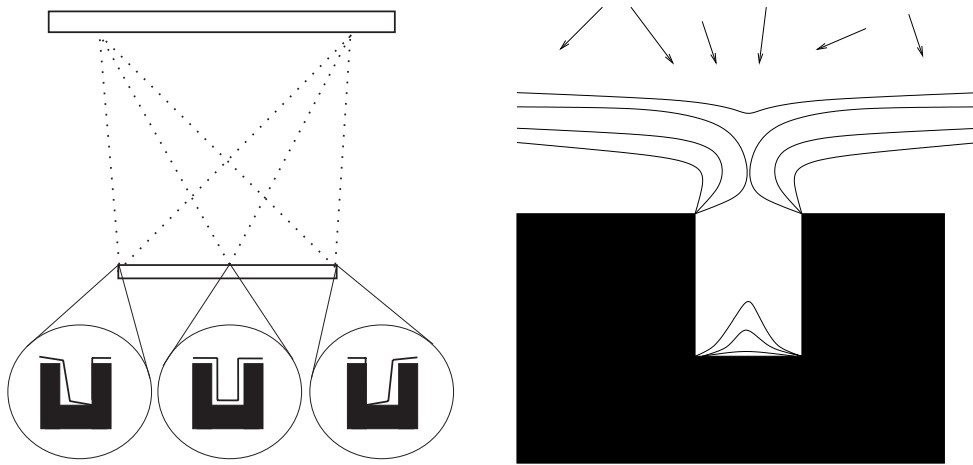
Problem with deposition asymmetry in low pressure PVD.

Problem with void formation in high pressure PVD.

Figure 5.12: Problems with deposition in trench structure in conventional PVD techniques.

The real value can be expected to be higher than the value of ~ 0.7 reported by [18] for high power pulsed magnetron sputtering due to higher magnetron current density met in our case.

5.5   Trench and via filling by metal

In the microelectronics much attention has been focus on the rapidly increasing number of devices per chip and on the shrinking of critical dimensions of components. The multilevel integrated circuit technology has place extreme demands to precise electrical interconnection. The individual transistors are fabricated within the silicon surface, they are contacted and wired together locally to form specific function and then interconnected together globally to form a fully functioning integrated circuit on the chip. To minimize signal propagation delay caused by parasitic capacitances and ohm resistances a high rise architecture is used in which multiple levels of metal are isolated by and interconnected through multiple levels of dielectrics. At this moment, trench and via filling by metal is important.

The filling of trench and via structure is more difficult than depositing a contact layer. This is driven primarily by the lack of fully ionization of the depositing species. At very low pressures, free mean path of a sputtered atom is in the order of few tens of centimetres. In this case of ballistic transport, majority of sputtered particles arrives to the substrate without any collision keeping the cosine angular

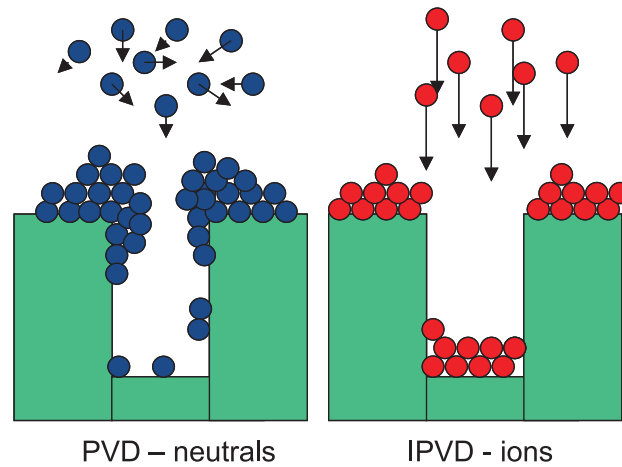PVD − neutrals   IPVD - ions

Figure 5.13: Schematic picture of trench filling by a high pressure PVD and an IPVD method.

distribution characteristic for a sputtering process. It results in an asymmetry of the deposition on the trench structure, as is schematically reported on the left part of Figure 5.12. At high pressures, sputtered atoms undergo many collisions before reaching a substrate and their velocity distribution near the substrate is almost isotropic. This results in eventual build of a sidewall deposit which could prevent to keep on the deposition at trench or via bottom. The example of this is schematically shown on right part of Figure 5.12 and left part of Figure 5.13. The experimentally obtained trench filling performed by a typical DC magnetron is shown in Figure 5.14. Low level of relative ionization and the fact, that an upper part of the trench see the plasma from larger solid angle than a bottom part causes that the majority of the atoms will be deposited there resulting in a poor filling, trench close-off and void formation.

To fill the trench structure properly, one need to impose on the sputtered particles a velocity perpendicular to the substrate surface. The most current method is to assure the high ionization degree of sputtered particles near the biased substrate. The ions are accelerated in the plasma sheath perpendicularly to the substrate surface and penetrate inside the trench or via. On the right part of Figure 5.13, there is schematically shown directionally non isotropic trench filling by positive ions accelerated by a negative bias applied on the substrate during the deposition. The experimentally obtained trench filling by a high power pulsed magnetron discharge where the ionization fraction of sputtered particle flux was ~ 70 percents is shown in Figure 5.15. This result was obtained by [18].

We wanted to try, if our system would be able to produce sufficiently high ionized fluxes of sputtered particles to fully fill the $2\,\mu$m trenches and vias with aspect
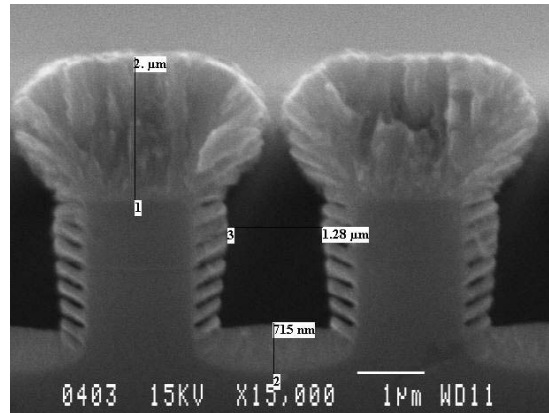
Figure 5.14: An example of typical trench filling by a DC magnetron discharge.
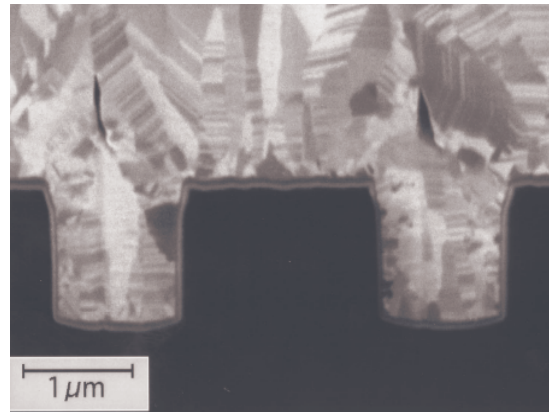

Figure 5.15: An example of trench filling performed by high power pulsed sputtering [18]. Ionization fraction of sputtered particle flux was ∼ 70 percents.

ratio 1 which we had at our disposal. The depositions in trench and via structures were performed in few experimental conditions. At almost all tested experimental conditions, the trench and via structure was well filled by a compact deposit. Any detailed or systematic study of the role of experimental conditions on the deposition quality, trench filling etc. has not been done. From the results, where the trench and via structure was well filled, we choose simply one to demonstrate the industrial potential of our system.

In the Figures 5.16–5.20, there are shown the results of a copper deposition in the trench and via structure. The experimental conditions were following - argon pressure 1.3 Pa, argon gas flow 7.7 sccm, repetition frequency 100 Hz, pulse duration 20 μs, voltage applied in pulse regime 1 kV, magnetron saturated current 40 A, magnetron current density 10 A/cm^2, deposition time 45 minuts, negative
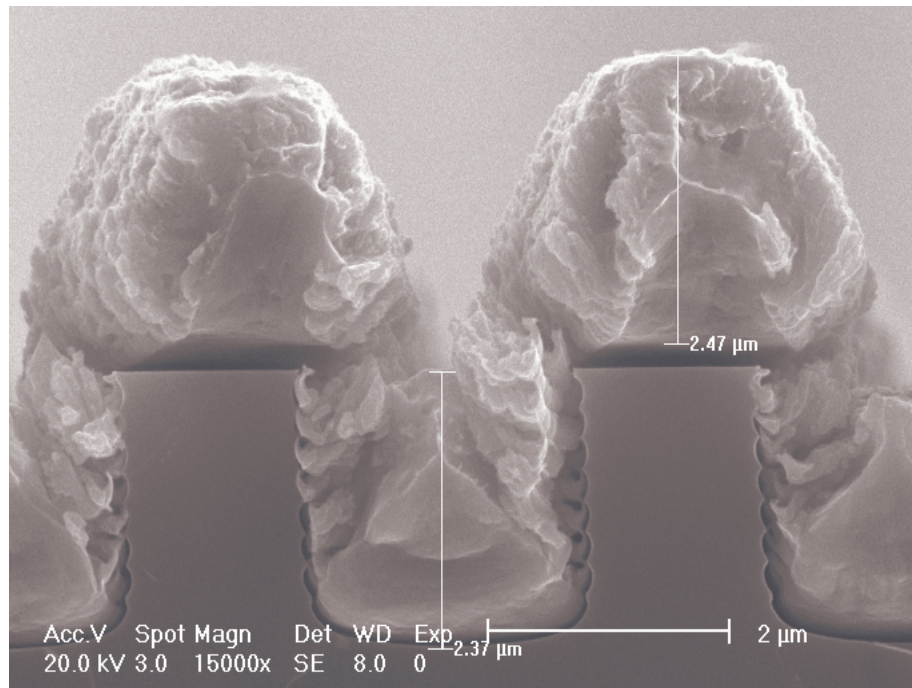
Figure 5.16: Compact copper deposition in trench structure performed by our preionized high power pulsed magnetron discharge at following experimental conditions: argon pressure 1.3 Pa, argon gas flow 7.7 sccm, repetition frequency 100 Hz, pulse duration 20 μs, voltage applied in pulse regime 1 kV, magnetron saturated current 40 A, magnetron current density 10 A/cm^2, deposition time 45 minuts, negative substrate holder bias 40 V, target to substrate holder distance 6 cm.

substrate holder bias 40 V, target to substrate holder distance 6 cm. The substrate was not treated neither before nor after deposition. After the deposition, the substrate was cut and pictures were obtained using scanning electron microscope FEI FEG XL30S.

In the Figures 5.16–5.17, there is shown a compact copper deposition in trench and via structure. Next Figure 5.18 demonstrates a good process reproductibility on six trenches compactly filled by the copper deposit. Figure 5.19 zooms in the trench structure and shows in detail the copper deposit inside. The last Figure 5.20 shows a detailed view on the top deposit outside from a trench structure.

The trench images show the volume of the cut deposit. Via images enable us to see the surface of the deposit, which was in contact with a wafer, because it was impossible to cut the $2 \times 2 \times 2$ μm deposit in the via. Always, the cut took place at the interface between the deposit and the wafer surface or somewhere in the volume of the wafer.
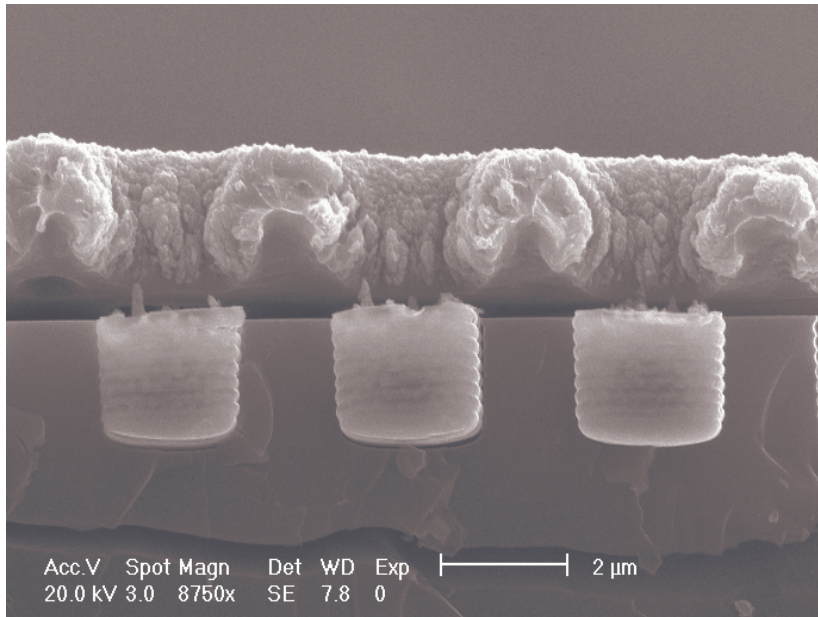
Figure 5.17: Compact copper deposition in via structure. Experimental conditions were same as in Figure 5.16.
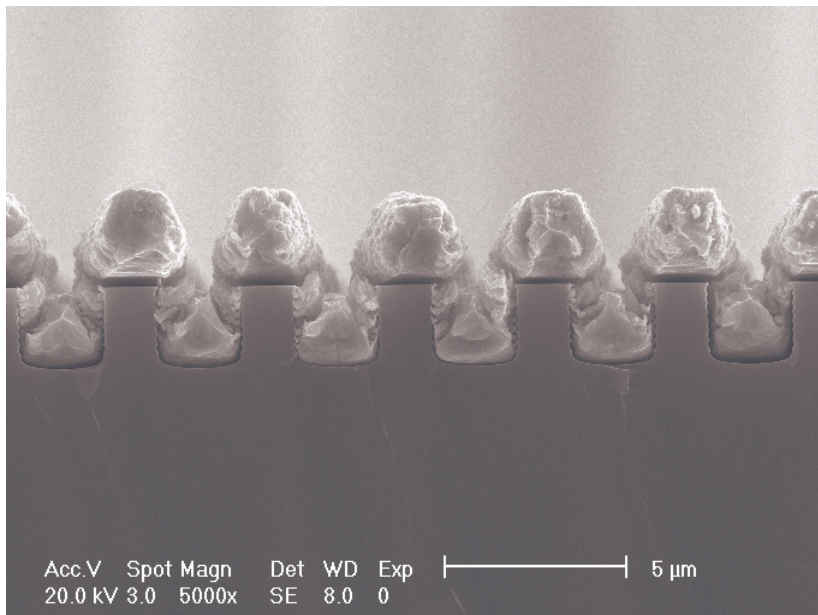

Figure 5.18: An example of six trenches compactly filled by copper deposit. One can observed a same deposit in all the trenches proving a good reproductibility of the deposition. Experimental conditions were same as in Figure 5.16.
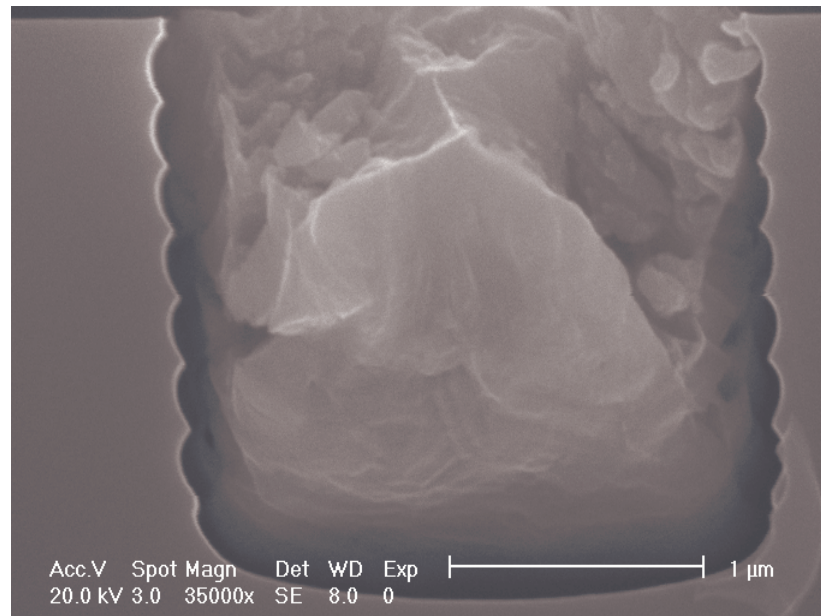
Figure 5.19: A detailed view on the compact deposit in the trench structure. Experimental conditions were same as in Figure 5.16.
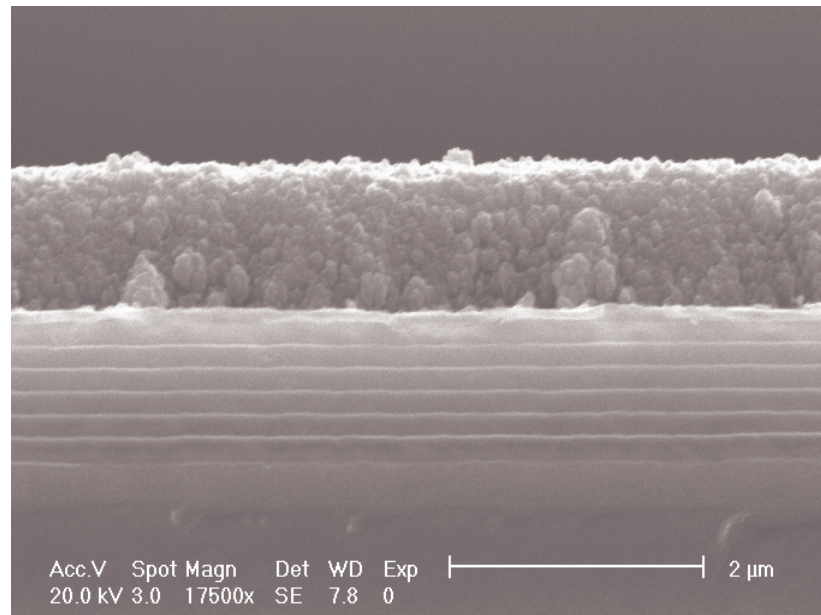

Figure 5.20: A detailed view on the top deposit outside from the trench structure. A non compact and porous deposit surface is observed. Experimental conditions were same as in Figure 5.16.

It is known [2], that without surface diffusion (migration) of deposited atoms, the predicted profiles are porous and non conformal. Increasing the surface diffusion improves the conformity. The bottom deposit becomes dense and fine-grained. The sidewall deposit tends to be more columnar and under dense. Usually, there is a very noticeable seam between these two deposits, which limits the rearrangement of the atoms on the surface by diffusion.

In our case, the compact deposit has been found at the bottom of the trench and it seems, that even the sidewall part of the trench is dense too. It can be seen from the trench cut in Figure 5.16 or in detail in Figure 5.19. The surface of the deposit in the via structure, which was in the contact with the wafer seems to be compact too, as can be seen in Figure 5.17. The Figure 5.20 shows porous and non conformal surface of the top deposit outside from the trench. This photo was taken, when the wafer was cut in a parallel way with the trench structure. However, volume of the top deposit is compact too, as can be seen in Figure 5.16.

The compact deposition inside the trench structure and even very remarkable at the sidewall and at the volume of the top deposit proves that the surface diffusion of deposited atoms was high. This surface diffusion is in our case probably due to very strong heating of growing film during the deposition process. The wafer removed from the deposition reactor immediately after the deposition was such hot that we were not able to touch it.

As was mentioned previously, the ionization fraction of the sputtered particle flux on the wafer is a critical factor in the trench filling. Formation of voids occurs when ionization fraction of metallic vapour flux is too low or aspect ratio of trench is too large. We succeeded to fill the trenches with aspect ratio 1. It has been determined [42], that the ionization fraction of the sputtered particle flux to successfully fill the trench of aspect ratio 1 has to be greater than ~ 0.7. We can conclude, that in our case, higher ionization fraction of sputtered particle flux than that ~ 0.7 was achieved. As an example, to fill the trenches and vias with aspect ratio 3, ionization fraction higher than ~ 0.85 is needed. We did few test depositions in order to fill deeper trenches and vias (with aspect ratio 4) but we did not succeed to fill them completely. Only ~ 20 percents filling was achieved before the top opening was totally blocked by deposited material. Since it has been only a test deposition, better results can be obtained after the optimization of the deposition process.

Without important re-sputtering, the overhang deposits grow faster than the bottom of the trench due to the larger solid angle and eventually seals the trench. It results into a void formation. When re-sputtering is allowed, the overhang deposit is progressively eroded to keep the opening clear. In IPVD reactors (with additional plasma between the target and the substrate), the species which do most of the re-sputtering are argon ions originated from the secondary plasma. In a typical IPVD reactor, Ar ions flux on the wafer may outnumber the copper ions flux

almost 10 times.

The deposition shown here was performed mainly in the self-sputtering regime and without presence of a secondary plasma. The process did not benefit from the re-sputtering by Ar ions such as in IPVD reactors with an additional plasma present. It means that with the same ionization fraction of the sputtered particle flux on the substrate, the trench structure of very high aspect ratio could be better filled by IPVD process with additional plasma than with high power pulsed magnetron sputtering. However, the thin films deposited by such an IPVD process could be contaminated by Ar ions, which bombard the growing film and penetrate inside. In our case, only very low Ar contamination in deposited layer can be expected. It should improve the electrical properties of the layer with respect to them deposited in IPVD reactors with additional plasma.

5.6 Conclusion

The very high magnetron current density operation met in our case can partially de-confine the magnetized plasma, enhance the plasma expansion providing high current densities onto the substrate.

It has been found, that even with very short pulses ($\sim 2\,\mu$s) we detect an important substrate holder current densities in the order of few tens of mA/cm^2. Increasing the magnetron pulse duration, the substrate holder current increases too. For magnetron pulse duration of 8 μs, substrate holder current reaches ~ 1 A, which corresponds to the substrate holder current density ~ 100 mA/cm^2. For 20 μs pulse, even higher maximum substrate holder current of about 6 A was reached, corresponding to extremely high substrate holder current density ~ 600 mA/cm^2.

Systematically prolonging of the magnetron pulse duration and recording the time evolutions of the substrate holder currents, the influence of the pulse duration on the ion saturated substrate holder current was studied. It has been found that for pulse duration lower than $\sim 4\,\mu$s, the integral of the substrate holder current increases less than linearly with the integral of the magnetron current. For pulse duration larger than $\sim 4\,\mu$s, it changes its behaviour and the dependence becomes linear. This linear dependence is explained by a simple model assuming a dynamic equilibrium between the copper ion fluxes leaving the magnetized region and the ionized fraction of the sputtered particle flux. This model is valid only in a stable self-sputtering regime. It allows us to place the transition time toward the stable self-sputtering regime to 4 μs. It is about the same transition time, as was estimated in previous chapter by optical emission spectroscopy and magnetron current measurement. A crude estimation gives a lower limit of the ionization fraction of the sputtered particle flux ~ 0.5.

Ion saturated current measured on the substrate is in the range of hundreds of

mA/cm^2 for a typical pulsed operation of our magnetron. Important ion current to the substrate requires the space charge compensation of the ions by the electrons in the area between the target and the substrate. We propose that during the high power pulsed operation, there are some regions of magnetized plasma, where the plasma density reaches value high enough that the plasma can not by anymore confined and may expand with the velocity driven by the ionized part of sputtered particles. It well correspond to velocity $\sim$ 6 km/s determined experimentally.

In the high power pulsed operation, we fully filled the 2 μm trenches and vias with the aspect ratio of 1 by a compact copper deposit. The first results make this sputtering process promising for industrial thin film deposition.

Chapter 6

Simultaneous Measurement of N and O Atom Density by Means of NO Titration

6.1 Introduction

One can observe growing interest in non-equilibrium kinetics of low pressure plasmas in nitrogen, oxygen and their mixtures. It is caused by the needs of various branches of science, e.g. physics of the upper atmosphere or plasma physics and technology (cleaning of pollutants, plasma processing, plasma sterilization).

In many studies various authors [43, 44, 45, 46, 47] observed that even a small admixture of oxygen into nitrogen (or inversely, nitrogen into oxygen) changes substantially the dissociation degree of the main gas. In order to achieve better understanding of this phenomenon it is necessary to know the absolute densities of both N and O.

There are also many other types of experiment, where the absolute concentration of atomic nitrogen and/or oxygen in a plasma afterglow is needed. As the atoms are radical species, their detection may be difficult. There are only few methods giving reliable absolute data, as for example two photon absorption laser induced fluorescence (TALIF) [48], nitrogen oxide titration [49, 50] or electron paramagnetic resonance (EPR) [51, 52]. Due to its simplicity, NO titration is most widely used. However, in most published works the experimental data are evaluated using the theory for an ideal case. In some circumstances, this can introduce substantial errors.

Recently a method using NO titration for simultaneous measurement of N and O concentrations was published [53] and then used [54, 55]. It is carried out in the region where [NO]$\geq$[N]. It is well suited for higher oxygen atom concentration

Reaction type		Value	Ref.
$N + O_2$	$\rightarrow$ products	$l_1 = 9.0 \times 10^{-17}$ cm^{3}s^{-1}	[61]
$N + N + (N_2)$	$\rightarrow$ products	$l_2 = 4.4 \times 10^{-33}$ cm^{6}s^{-1}	[62]
$N + NO_2$	$\rightarrow$ products	$l_3 = 3.9 \times 10^{-12}$ cm^{3}s^{-1}	[61]
$N + NO$	$\rightarrow$ products	$k_1 = 1.6 \times 10^{-10}$ cm^{3}s^{-1}	[63]
$N + O + (N_2, O_2)$	$\rightarrow$ products	$k_2 = 9.1 \times 10^{-33}$ cm^{6}s^{-1}	[64]

Table 6.1: Reaction channels of N atom destruction in the late afterglow of $N_2 - O_2$ discharge. For three body reactions we assumed the nitrogen pressure 400 Pa, which gives $l_2[N_2] = 4.4 \times 10^{-16}$cm^{3}s^{-1} and $k_2[N_2] = 9.1 \times 10^{-16}$cm^{3}s^{-1}.

but it is quite insensitive for lower O densities.

Unfortunately, exactly this low [O] region is very interesting for studying the increase of dissociation rate of nitrogen when very small molecular oxygen admixture (under 1%) is added [56, 57].

Especially for this range a NO titration variant was developed. It is based on fitting of data in [NO]≤[N] region by theoretical curve and gives absolute values of [N] and [O] at the same time rather easily.

As we wanted to test its correctness, the results from NO titration were confronted with other methods, such as electron paramagnetic resonance (EPR) or optical emission spectroscopy.

6.2   Titration by NO in pure nitrogen afterglow

Into the flow of partially dissociated nitrogen gas a small quantity of nitrogen oxide (NO) is added. It induces many new chemical reactions leading to creation of oxygen containing radicals and molecules. These reactive species will mutually react, which influences the N and O atom density evolution in the afterglow.
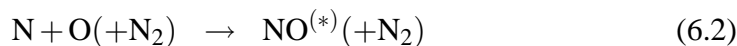
Recently, an article describing the $N_2 - O_2$ discharge and its afterglow was published [58]. There are described processes of N and O atom production and destruction in the active discharge, formation of so called pink or short lived afterglow [59, 60] and the processes in the late Lewis-Rayleigh afterglow. It was shown, that the O atom density decreases in the afterglow very slowly. It concludes, that the volume processes in the plasma afterglow does not lead to a significant decrease of the O atom density. It describes many channels of N atom destruction in the late afterglow. Because the NO titration is usually performed in the late afterglow, only that destruction processes of N atoms caused by ground state species are relevant. They are shown in Table 6.1 together with corespond-

Reaction	Value	Ref.
6.1	$k_1 = 1.6 \times 10^{-10}$ cm^{3}s^{-1}	[63]
6.2	$k_2 = 9.1 \times 10^{-33}$ cm^{6}s^{-1}	[64]
6.3	$k_3 = 6.4 \times 10^{-17}$ cm^{3}s^{-1}	[65]

Table 6.2: Values of rate constants of reactions 6.1 – 6.3 which were used in our calculations. For reaction (2) we assumed the nitrogen pressure 400 Pa, which gives $k_2[N_2] = 9.1 \times 10^{-16}$cm^{3}s^{-1}.

ing reaction coefficients [61, 62, 63, 64] computed for room temperature and gas pressure of 400 Pa. Since dissociation degrees of oxygen molecules are very high (tens of percents), the reaction with O will be more significant than the slower reaction with O_2 which was neglected for further consideration. NO_2 molecules are usually $\sim 10^{-8}$ of total gas density, which makes this channel of N atom destruction negligible too. Volume three body recombination was neglected too. This reaction has about two times lower reaction coefficient than reaction with O atoms and moreover, during the course of NO titration, N atoms are converted to O atoms. The main mechanisms of N atom destruction during a course of NO titration will be its mutual reaction with O atoms and NO molecules, introduced intentionally into N_2 afterglow.

Among the possible chemical reactions these are the most important in NO titration:

$$N + NO \quad \rightarrow \quad N_2 + O \tag{6.1}$$
$$N + O(+N_2) \quad \rightarrow \quad NO^{(*)}(+N_2) \tag{6.2}$$
$$NO + O \quad \rightarrow \quad NO_2^* \tag{6.3}$$

The reaction 6.1 is very fast and converts all available N atoms and NO molecules to O atoms. If there was more N atoms than NO molecules, reaction 6.2 follows and produces NO molecules. A part of them is excited. It then radiates in UV region as NO β system (B$^2\Pi$–X$^2\Pi$, λ$\sim$320 nm). On the other hand, if [NO]>[N] then reaction 6.3 produces NO_2^* which radiates as green-yellow continuum (A^{2}B$_1$–X^{2}A$_1$) around 570 nm.

This can be used to measure by NO titration the absolute concentration of N atoms. It is sufficient to slowly increase the flow of NO and record optical emission spectra of NO* beta system and NO_2^* green-yellow continuum. In the moment (so called dark point) when the NO* bands decreased to zero and NO_2^* continuum is just to appear, the densities of introduced NO and initial N are the same. As NO flow is easily measurable by flow controller, this method was used by many authors.
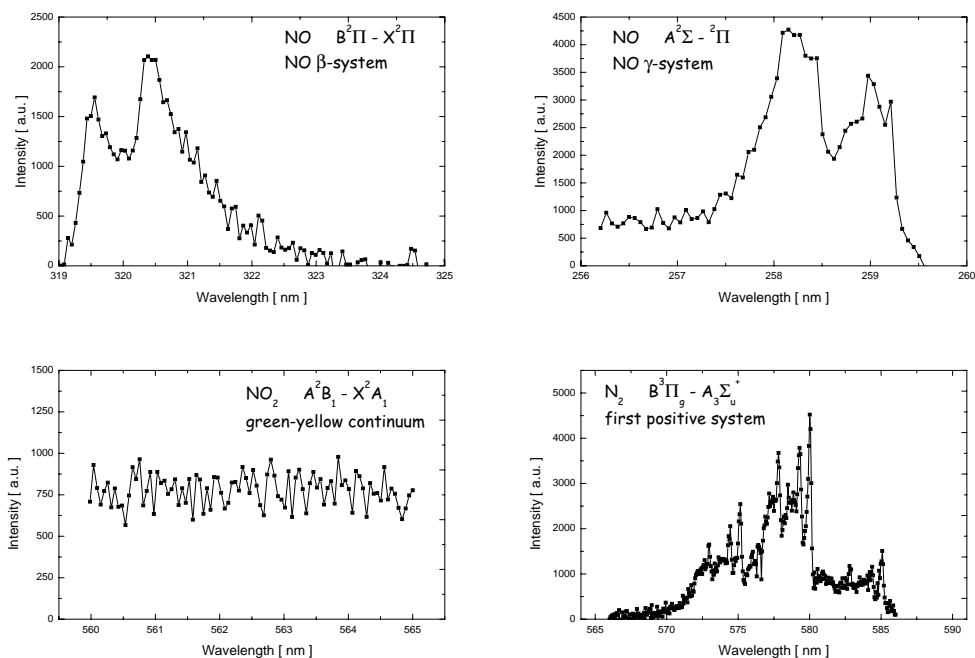
Figure 6.1: The example of four main systems detectable by optical emission spectroscopy in the $N_2 - O_2$ discharge afterglow.

Moreover the systems relevant in NO titration, other optical emission spectra may be recorded. Until the dark point is reached, the 11-7 transition of nitrogen first positive system is observed, as result of nitrogen atom three body volume recombination. The intensity of this transition is proportional for a given pressure to the square of nitrogen atom density and may be used to monitor the relative nitrogen atom density evolution.

In the UV-VIS range of spectra, there are not only NO β-system bands, but also very intense NO γ-system bands. They result in the $N_2 - O_2$ afterglow from reaction of NO molecule with nitrogen metastable molecules [66]. Because this system is not relevant in NO titration, it is necessary to make sure that really NO β system intensity is measured during the course of NO titration. Both systems are observed as double-headed. Fortunately NO β system degrades to red but NO γ system to shorter wavelengths [67], which makes them easy distinguishable. The example of these bands is shown in Figure 6.1.

To find the dark point with good accuracy in a classical way, one needs to carry out many measurements. However it is possible to achieve the same accuracy with less experimental points if the shape of a solution of 6.1 – 6.3 is considered. The intensity I_{NO} of NO β system radiation is proportional to the population of NO
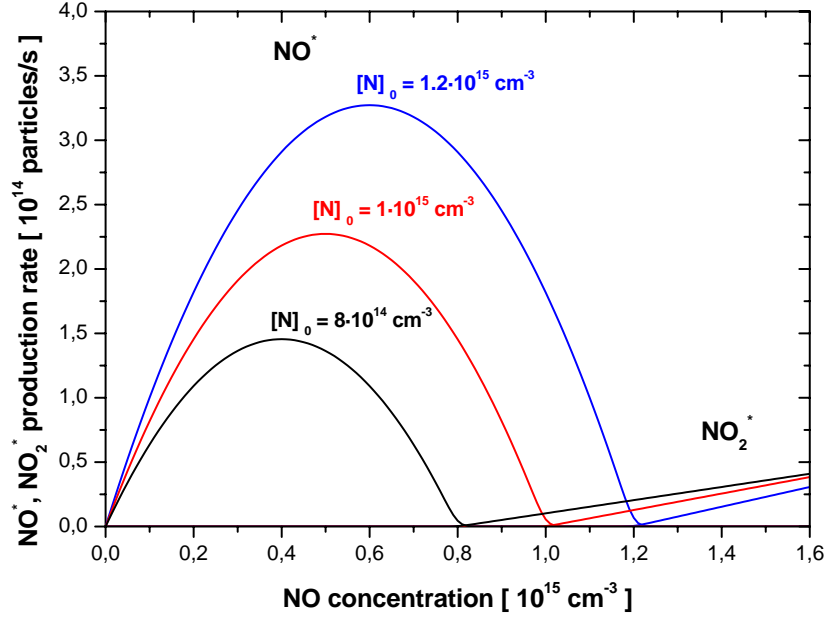
Figure 6.2: Production of excited molecules in the course of NO titration in nitrogen afterglow at pressure 400 Pa. Three curves correspond to different concentration of N atoms: 8, 10 and 12×10^{14} cm^{-3}.

B state, which is in the afterglow populated by reaction 6.2 and depopulated by spontaneous emission to lower energy levels.

$$\frac{d[NO(B)]}{dt} = k_2[N][O][N_2] - \sum_j A_{Bj}[NO(B)] \qquad (6.4)$$

In the steady state, population of the NO molecules in B state is proportional to actual values of [N] and [O]. Consequently the intensity of NO β system is proportional to actual values of [N] and [O] too.

$$I_{NO} \propto [NO(B)] = \frac{k_2[N][O][N_2]}{\sum_j A_{Bj}} \propto [N][O] \qquad (6.5)$$

As the result of reaction 6.1 each NO molecule produces one O atom and consumes one N atom. The dependence $I_{NO} = f([NO]_0)$ is then

$$I_{NO} \propto [N][O] = ([N]_0 - [NO]_0)[NO]_0 = [N]_0[NO]_0 - ([NO]_0)^2 \qquad (6.6)$$

where subscript 0 denotes the initial densities (without the influence of products of reactions 6.1 – 6.2). This is equation of parabola with one root at zero and
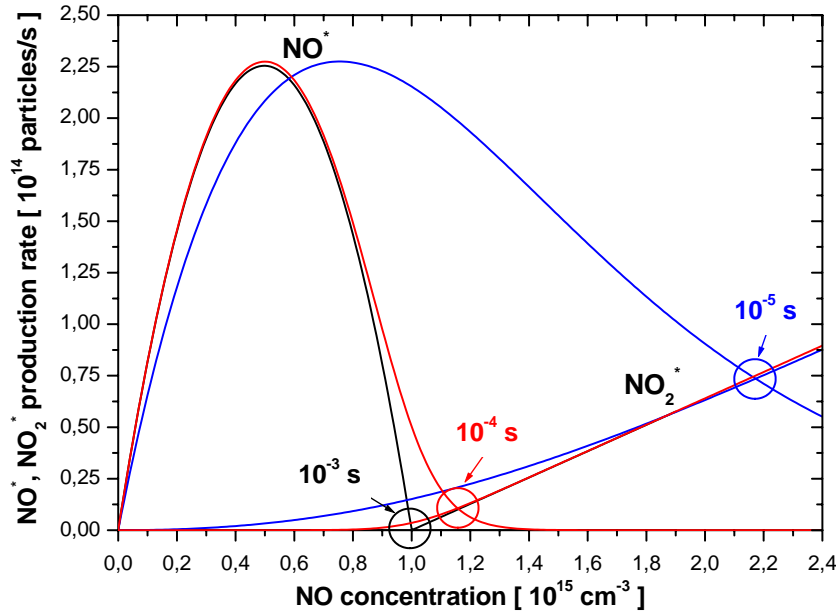
Figure 6.3: Distortion of ideal case due to insufficient reaction time. The intersection of NO^* and NO_2^* curves is moving away from the correct value of 1×10^{15} cm^{-3} for too short reaction times.

second root at dark point. Nice use of this fact is that by fitting of experimental data by parabola we can determine the position of dark point precisely even from sparse data.

In spite of the ease of use of NO titration method certain problems may arise. The 'ideal' behaviour (see figure 6.2) is observed only for limited range of reaction times. However, in many published works the authors recorded emission spectra from the region too close to NO inlet. In that case the main reaction 6.1 is not finished and observed results are distorted (see figure 6.3). The experimental evidence of this effect is shown in figure 6.10. It is clear that there is even no dark point any more. As a quick cure some authors [24] suggest to take the intersection of both lines as a dark point. Unfortunately this is not valid, because (i) the scaling of curves will influence the position of dark point and (ii) even for the same scale of both curves the position of intersection depends on the reaction time. In some cases the error of such quick estimation may be relatively important as is demonstrated in figure 6.3. Therefore it is necessary to either correct for insufficient reaction time or even better to avoid short reaction times altogether.

6.3 NO titration in N_2 – O_2 mixtures

When the afterglow of nitrogen – oxygen discharges is studied, the set of reactions 6.1 – 6.3 remains the same but initial conditions are different. The solution for sufficient reaction times (reaction 6.1 finished) has the form

$$I_{NO} \propto ([N]_0 - [NO]_0)([O]_0 + [NO]_0) = -([NO]_0)^2 + ([N]_0 - [O]_0)[NO]_0 + [N]_0[O]_0 \tag{6.7}$$

In comparison with the case of pure nitrogen a new factor appears – the initial concentration of O atoms. When concentration of O atom equals zero we get easily the Equation 6.6, which is valid in the case of pure nitrogen. Equation 6.7 is again an equation of parabola

$$I_{NO}(x) = ax^2 + bx + c \tag{6.8}$$

where the coefficients a, b and c follow b/a=$[O]_0$-$[N]_0$ and c/a=-$[N]_0[O]_0$.

So by fitting the experimental dependence $I_{NO} = f([NO])$ by parabola we obtain the results

$$[N]_0 = \frac{-b - \sqrt{b^2 - 4ac}}{2a} \tag{6.9}$$

$$[O]_0 = -\frac{-b + \sqrt{b^2 - 4ac}}{2a} \tag{6.10}$$

It is shown in figure 6.4 that one of the roots is moving with initial O concentration to the value -$[O]_0$ but the second one remains fixed at $[N]_0$ as it was in the case of NO titration in the pure nitrogen afterglow. Therefore the dark point does not shift and even in presence of O atoms the standard method of [N] measurement by NO titration works.

Measured data exhibiting these parabolic dependencies are shown in figure 6.11 in the experimental part of this chapter.

In the figure 6.5 there is shown the time evolution of important species densities during the course of NO titration. At the time t=0, the amount 2.5×10^{14} cm^{-3} of NO molecules was ideally mixed with concentration 1×10^{15} cm^{-3} of N and 1×10^{15} cm^{-3} of O atoms. We can see that for $t < 10^{-4}$ s the [N] and [NO] decrease due to reaction 6.1. At time t_{eq}, in this case around 1×10^{-4} s, an equilibrium between the NO loss due to reaction (1) and the production due to reaction (2) is established. For times higher than 1×10^{-4} s resulting [NO] value is

$$[NO] = \frac{k_2[N_2][N][O]}{k_1[N] + k_3[O]} \tag{6.11}$$

where [O] is total density of O atoms, which includes not only the initial O atoms but also those ones, produced by the reaction 6.1. Because $k_3[O] \ll k_1[N]$, the
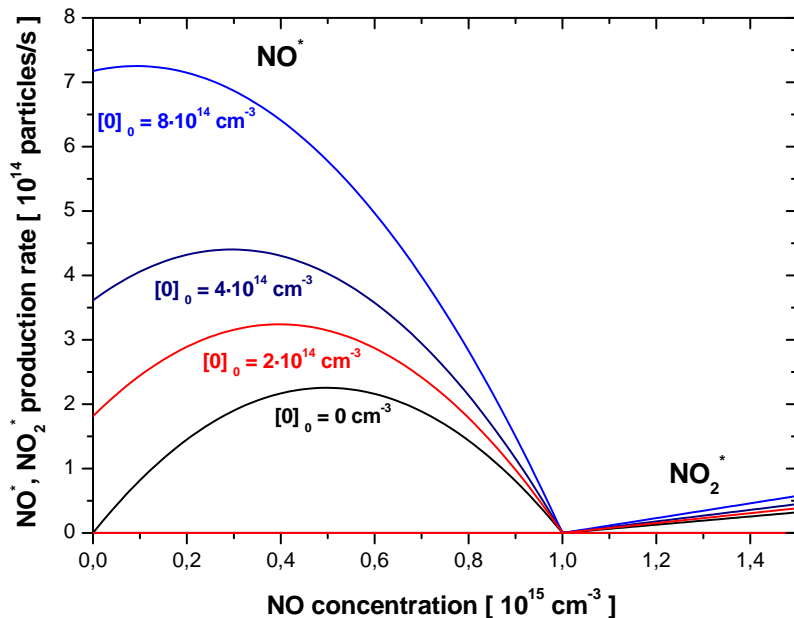
Figure 6.4: Production of excited molecules in the course of NO titration in nitrogen + oxygen afterglow for various oxygen atom concentration. The nitrogen atom concentration is fixed at 1×10^{15} cm^{-3} and the pressure is 400 Pa. It is seen that for rising oxygen content the dark point does not move but the shape of NO* curve changes.

previous equation reduces to

$$[\text{NO}] = \frac{k_2[\text{N}_2]}{k_1}[\text{O}] \tag{6.12}$$

Although the NO and O equilibrium is established, there is always continuous N atom loss due to reactions 6.1 and 6.2, which removes O and N and produces NO, which is in turn removed by another N and produces O and N_2. Time dependence of N atom density is given by

$$[\text{N}] = ([\text{N}]_0 - [\text{NO}]_0) \exp(-2k_2[\text{N}_2]([\text{O}]_0 + [\text{NO}]_0)(t - t_{\text{eq}})) \tag{6.13}$$

which is exponential decay. In the case of NO titration into pure nitrogen a prolongation of reaction time reduces the error of measurement (when only 6.1 – 6.3 are considered, of course).

However, in the case of N_2–O_2 mixture, the long reaction time is not optimal because it negatively affects the error of O concentration estimation. Dark
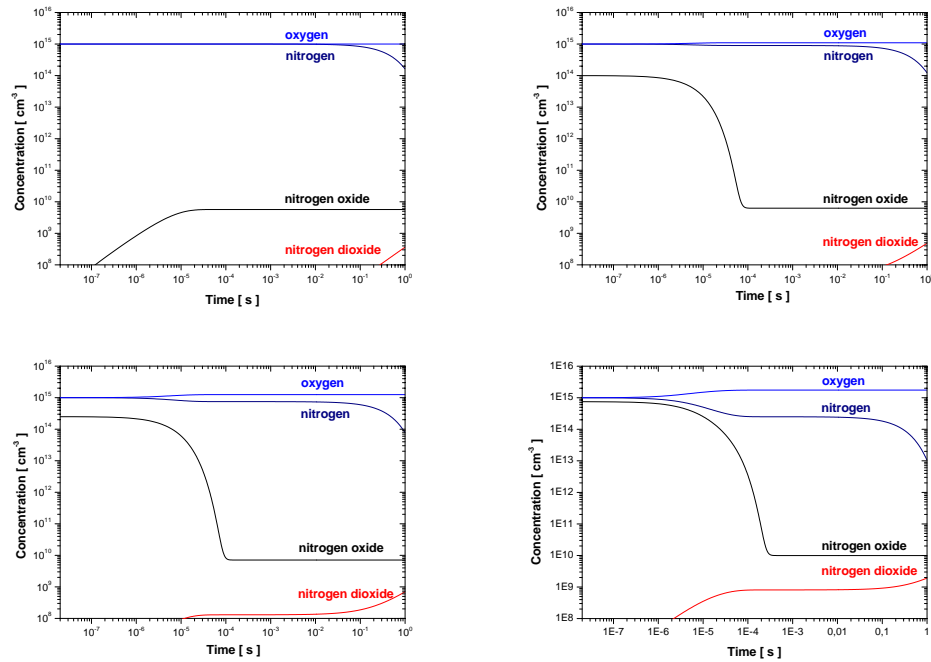
Figure 6.5: Time development of important species in the course of NO titration in nitrogen + oxygen afterglow. Curves were calculated for 400 Pa, $[N]_0 = 1 \times 10^{15}$ cm^{-3}, $[O]_0 = 1 \times 10^{14}$ cm^{-3} and $[NO]_0 = 0, 1.0, 2.5$ and 7.5×10^{14} cm^{-3}.

point position does not move with reaction time, as it is governed by fast reaction 6.1 and therefore N atom concentration is well determined for higher reaction times, too. However, NO* intensity is proportional to the concentration of oxygen atoms (which does not change with time) and to concentration of nitrogen atoms (which exponentially decreases) and thus longer reaction times deform the shape of parabola. This results in larger error in fitting procedure needed for calculation of [O]. In figure 6.6 it is shown how the relative error of [N] and [O] estimation depends on reaction time. The graph was calculated for pressure 400 Pa, $[N]_0 = 1 \times 10^{15}$ cm^{-3}, $[O]_0 = 5 \times 10^{14}$ cm^{-3}, density of N and O atoms was calculated from parabola fit of NO* curve and compared with initial values introduced into simulation.

From the analysis described here it might seem that we are able to calculate a correction to the measured value. However, the situation is more complicated due to the fact that the mixing of reactants is not immediate [68]. In fact, for short distances between NO inlet and photodetector it is nearly impossible to determine the value of the reaction time and as a consequence to calculate the correction factor. So the only solution is to increase the reaction time to a value when error of N and
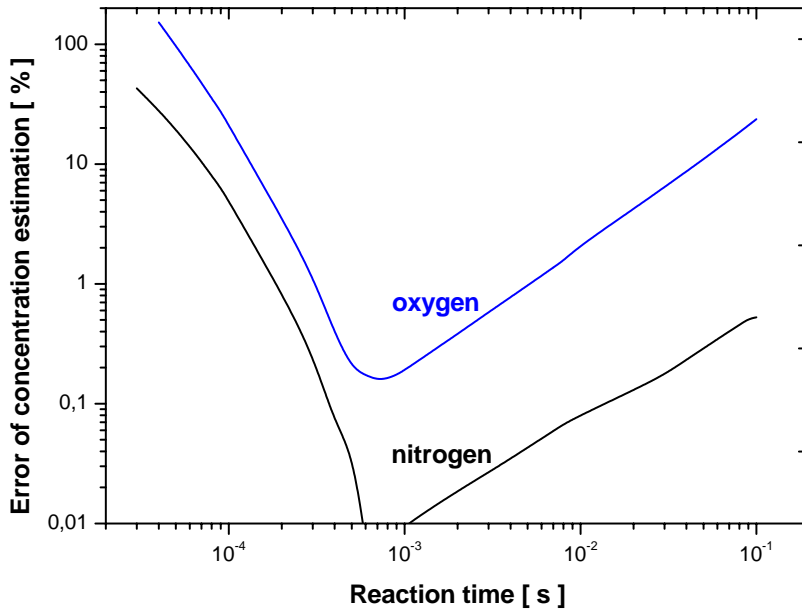
Figure 6.6: Relative error of [N] and [O] estimation as a function of the reaction time. Curves were calculated for 400 Pa, $[N]_0=1 \times 10^{15}$ cm^{-3} and $[O]_0=5 \times 10^{14}$ cm^{-3}.

O atom estimation is sufficiently low. For longer reaction times, [N] estimation is rather precise, with relative error under 1% which is much lower than error of [O] estimation. Increasing reaction time results in increase of relative error of O atom estimation, so it is necessary to choose the position of photodetector carefully.

In figure 6.7, there is shown how the error of [O] estimation depends on the density of [O] atoms for two reaction times. The loss of [N] with increasing [O] is due to the production of NO which in turn quickly reacts with another N, producing N_2. In figure 6.7 it is clearly seen that for ten times higher O atom density the relative error of [O] determination increases only twice.

Therefore on the basis of the presented analysis we conclude that the choice of correct reaction time is more important than the influence of O atom density on measurement errors.
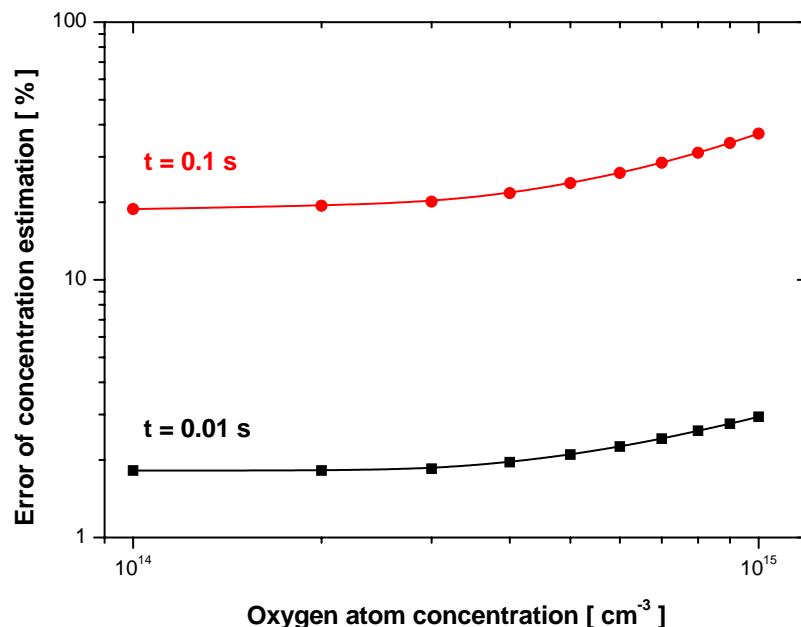
Figure 6.7: Relative error of [O] estimation for two reaction times. We used 400 Pa and $[N]_0=1 \times 10^{15}$ cm^{-3} for calculation.

6.4 Experimental set-up

Schematic drawing of the apparatus is shown in figure 6.8. A microwave discharge is produced in a quartz discharge tube with inner diameter of 13 mm by means of surfatron cavity, powered by 30 W magnetron working at 2.45 GHz. Our experiments is carried out in a flowing regime, afterglow is observed downstream in 1 m long quartz tube with inner diameter of 8 mm. Small amount of oxygen admixture is added to a main nitrogen gas before its going through the discharge. The gases are led from gas bottles through the mass flow controllers to a cold trap, which removes traces of unwanted impurities, like a water or hydrocarbons. The purities of N_2 and O_2 were better than 99.995% according to manufacturer's certificates. Flow rate of O_2 admixture was varied between 0 and 2.5 sccm, nitrogen flow rate being kept constant at 100 sccm. The pressure in the discharge was 480 Pa.

At the end of the afterglow tube the titration probe is mounted. Nitrogen oxide is introduced into the flowing gas containing N and O atoms. At certain distance (40 cm) the observing window is placed and through it the intensities of NO*(β system, $B^2\Pi$–$X^2\Pi$), NO_2^*(yellow-green continuum, A^2B_1–X^2A_1) and N_2^*(1st positive system, $B^3\Pi_g - A^3\Sigma_u^+$) are recorded. The tube is bended so the
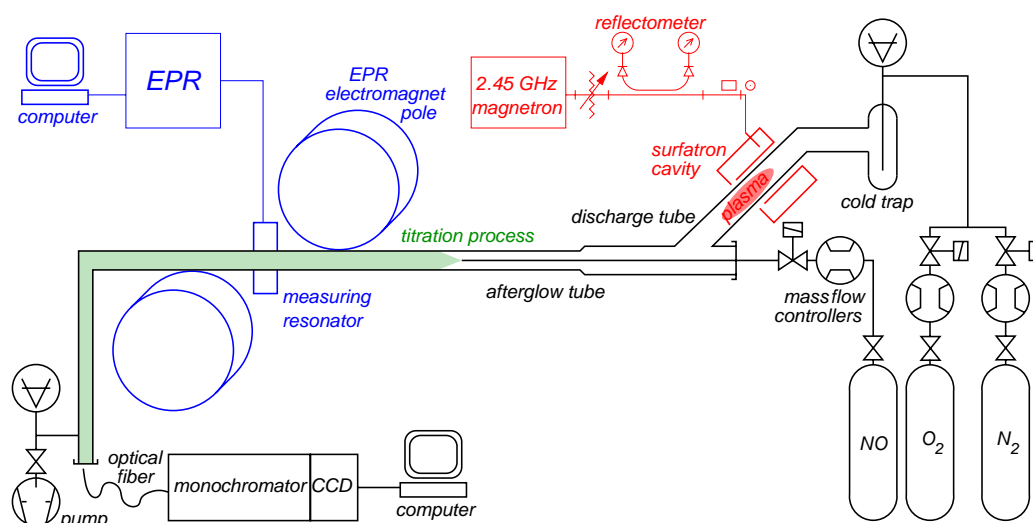
Figure 6.8: Experimental set-up. Plasma is produced by means of surfatron cavity, powered by 30 W, 2.45 GHz magnetron. Working gas is nitrogen with small oxygen admixture. NO is introduced into the flowing gas containing N and O atoms. Afterglow tube pass through the EPR resonator. OES is performed through quartz window.

radiation of the earlier stages does not enter into the collecting optical fibre.

For optical emission spectroscopy (OES) we used Jobin-Yvon TRIAX 320 monochromator equipped with 1200 grooves/mm grating and CCD camera. Meanwhile, the afterglow tube passes also through the measuring resonator of electron paramagnetic resonance spectrometer JEOL JES-3B operating in X-band to measure the concentration of atomic oxygen. This method is based on resonance absorption of microwave energy by the transitions between Zeeman split levels. In the case of oxygen, the ground levels $^3P_{1,2}$ have non-zero magnetic momentum and so they split in magnetic field. After a calibration of the EPR device by molecular oxygen [51], which is paramagnetic too, the absolute concentration of oxygen atoms was obtained. The advantage of such calibration is well defined fill factor, which is not easy to achieve with traditional DPPH (diphenylpicrylhydrazyl) standard. The use of EPR spectroscopy to determine the absolute concentrations of wide range of radical species is described in [69].

6.5   Experimental results and discussion

Here we apply the method described in the theoretical part of this chapter to measure N and O density in the plasma afterglow.
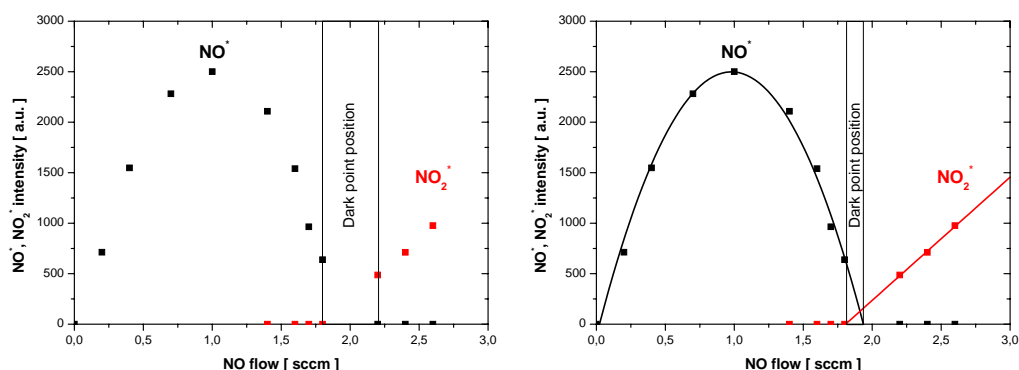
Figure 6.9: An example of measured NO^* and NO_2^* emission during a course of NO titration (left figure). On the right figure, measured data were regressed by theoretical parabolic and linear dependency.

First we want to show that using the fitting of experimental data by theoretical parabola for NO^* and line for NO_2^*, we can determine the position of dark point more precisely than by the classical method even from sparse data. It is shown in Figure 6.9, in the left figure, there are plotted the measured intensities of NO^* and NO_2^* as a function of the amount of NO added into the post-discharge. From the NO^*, we can conclude, that the dark point is somewhere between the last positive value and the first zero value of NO^*. Similarly, from NO_2^*, we can conclude that the dark point is somewhere between the last zero value and the first positive value of NO_2^*. It defines the interval, labelled by the vertical lines, where the dark point can be. On the right figure, the same data are plotted together with the theoretical fits. One can easily observed, that the interval labelled by the vertical lines is reduced. With more sparse data, this method will be even more accurate and less time consuming than the classical one.

We wish to emphasize the often neglected fact, that in order to get N atom concentration correctly, reaction between N and NO must be completed. In the figure 6.10 there are plotted typical examples of NO^* and NO_2^* intensities in the course of titration for two distances between NO inlet and optical fibre. In the case of shorter distance (1 cm) the reaction of N and NO in spite of being rather fast is not finished yet (also due to slow mixing of reactants [68]) and there is no well defined dark point any more. These curves are in good accordance to numerical calculations shown in figures 6.2 and 6.3.

The best way how to get correct N atom density in pure nitrogen afterglow is to avoid short reaction times altogether, i.e. to increase the distance between NO inlet and the point of optical measurement until well defined dark point is observed (the case for 40 cm distance in figure 6.10 is well beyond such distance).
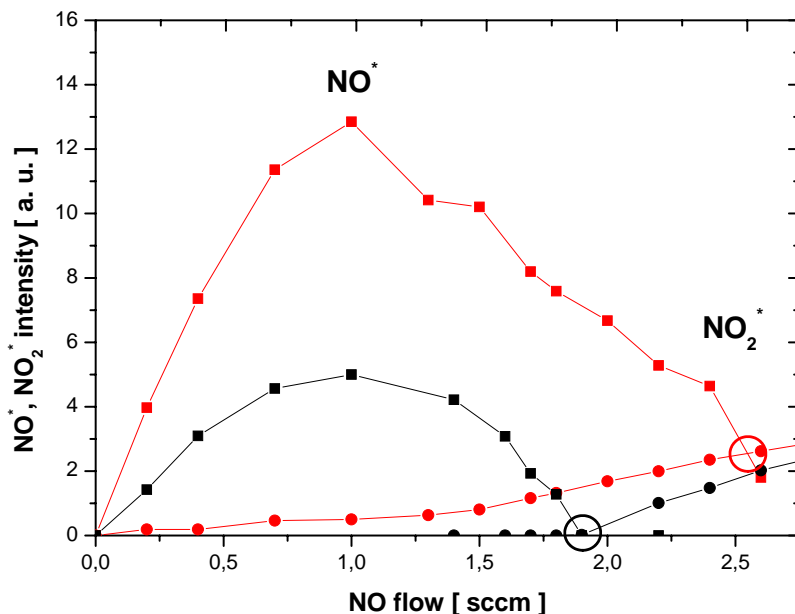
Figure 6.10: An example of recorded intensities of NO^* and NO_2^* emission during the course of titration for two distances (1 cm - red line and 40 cm - black line) between NO inlet and the optical fibre. The reaction time for shorter distance is clearly insufficient.

Recently a paper [55] describes the use of a method, which besides [N] permits to measure also [O] by means of comparing the slope of NO_2^* intensity after the dark point with and without oxygen admixture. That method is well suited for higher oxygen admixtures (in the order of several percents). However, for the very interesting region of low oxygen admixtures, where steep rise of nitrogen dissociation is observed, this method is not sensitive enough. Therefore we developed a method for simultaneous [N] and [O] measurement using NO titration suitable for low O densities, as was described in theoretical part. Another advantage of our method in comparison with [55] is that no calibration measurement with pure nitrogen is needed.

From the analysis shown before it follows that the density of nitrogen atoms can be obtained classically from the dark point as in the case of pure nitrogen post discharge. But quicker and more precise way is to fit the dependence of NO^* on [NO] by parabola, and from three fitting parameters calculate both [N] and [O].

In figure 6.11 there are plotted NO β system intensities during the course of titration for different amounts of oxygen admixture in nitrogen. One can see that
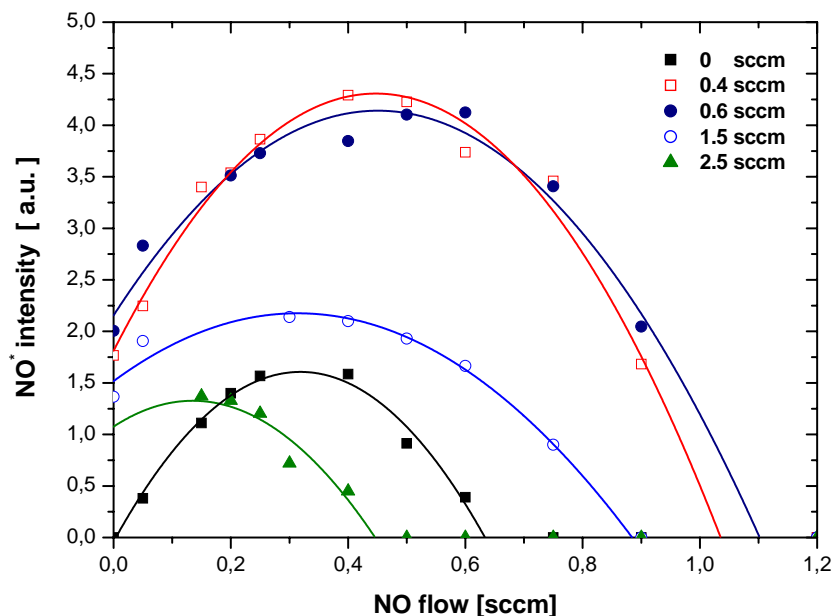
Figure 6.11: Intensities of NO*(β system, transition 0–8, $\lambda \approx 320$ nm) for varying NO flow. Five curves correspond to 0.4, 0.6, 0.8, 1.5 and 2.5 sccm of oxygen admixture into 100 sccm of nitrogen.

for zero NO flow, NO* is zero only for pure nitrogen, as the presence of oxygen leads to production of NO*. For different oxygen admixtures the position of dark point moves which indicates changing of [N]. Together with experimental points the fitted parabolas are shown, too. From the fitting parameters then [N] and [O] were calculated using relations (6.9) and (6.10).

In figure 6.12 there are shown the results of NO titration in the form of the dissociation degree $\eta = \frac{1}{2}$[X]/[X$_2$] of nitrogen and oxygen as a function of oxygen admixture. Notable is rather high oxygen dissociation degree (nearly 20%).

We compared the results of NO titration with two other methods, which were carried out simultaneously with the main measurements. The absolute density of oxygen atoms was measured by electron paramagnetic resonance. The density of N atoms was determined from OES. It is known that some vibration bands of nitrogen first positive system (e.g. N$_2$B$^3\Pi_g$ v=11 –N$_2$A$^3\Sigma_u^+$ v=7) are caused by recombination of atomic nitrogen and thus their intensities are proportional to [N] squared. This method gives only relative values but it is sufficient for our purposes.

From the figure 6.13 it is seen that all three methods are in very good accor-
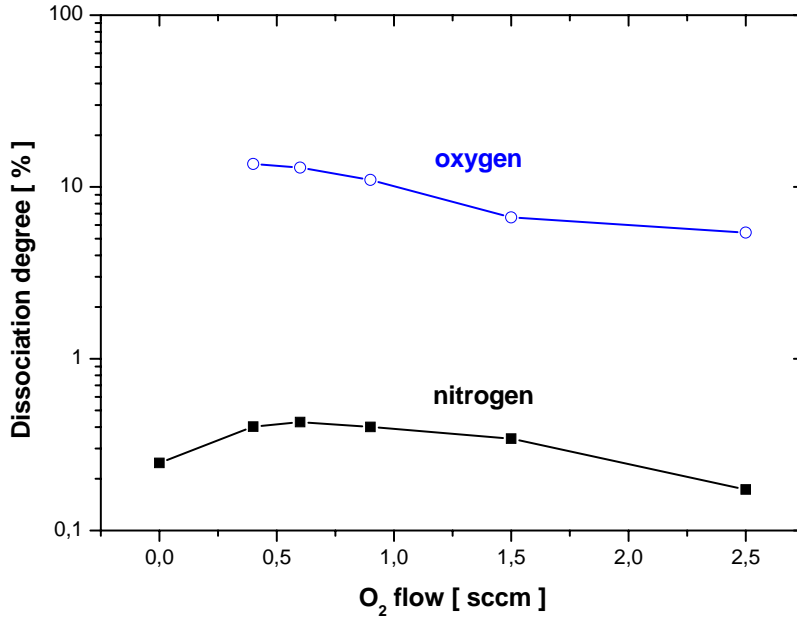
Figure 6.12: Dissociation degree of nitrogen and oxygen as a function of oxygen admixture.

dance. Absolute values of [O] given by EPR and by NO titration as well as absolute values of [N] from titration and scaled [N] from the square root of nitrogen 1st positive system intensity coincide very well.

The variation of the concentration of nitrogen atoms versus the O_2 percentage was previously measured by e.g. [56] and the same behaviour as published in this paper (i.e. steep increase of N_2 dissociation followed by slow decrease for increasing O_2 admixture) was observed. Often, the increase of N atom concentration for small O_2 percentage is explained by change of the reduced electric field E/N [56], by various homogeneous reactions [56] or by decrease of the wall recombination coefficient [70]. Depending on a purity [71] of the nitrogen gas, the [N] can be increased even by the factor 50 [57]. The decrease of [N] for larger O_2 percentage can be attributed to the homogeneous destruction processes. In the paper [72] the dissociation degree in the afterglow was increased even by adding the admixture directly to the pure nitrogen afterglow. However, all the above mentioned hypotheses are based on a presence of the admixture in the active discharge. It follows that these theories can not be complete.
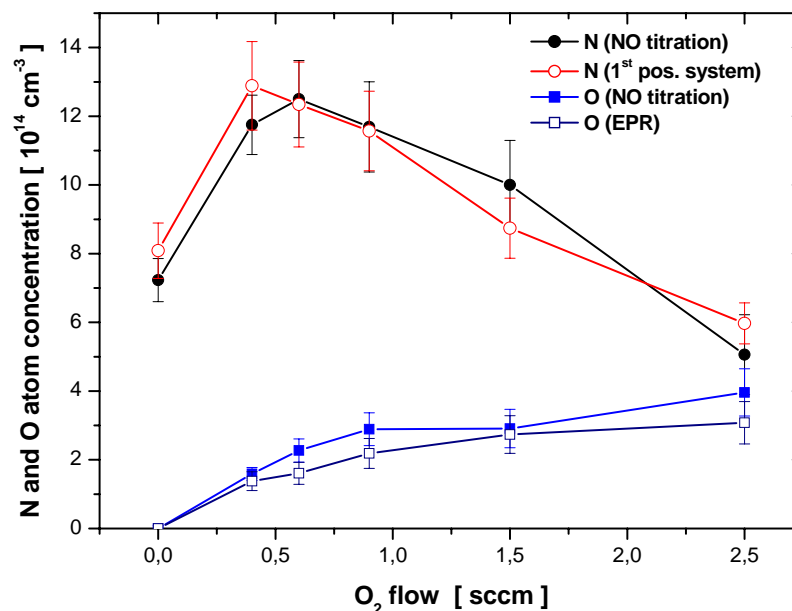
Figure 6.13: Concentrations of N and O atoms in the afterglow as the function of oxygen admixture in 100 sccm of nitrogen. The values obtained from intensities of nitrogen $1^{st}+$ system are relative and so they were scaled.

6.6 Conclusion

A method to obtain simultaneous N and O atom concentrations in N_2 and N_2-O_2 post discharges by NO titration from NO β system UV radiation was described and influence of reaction time on the accuracy of such measurement was discussed.

Presented method is based on a fitting of the measured data points by a theoretical parabolic curve (equation 6.7) and it is suitable for estimation of low O atom densities. It was shown, that for short reaction times (for our typical values of [N], [O] and [N_2] it is bellow 10^{-4} s) there are the problems with estimation of dark point. Increasing the reaction time improves the accuracy of N atom density estimation in pure nitrogen afterglow. In the case of $N_2 - O_2$ post discharge, there is a range of times, $10^{-4} - 10^{-2}$ s (again, numerical values depend on given experimental conditions), where accuracy on N and O atom concentration is sufficient. For higher reaction times, mutual reactions between N, O and NO species affect the shape of NO* parabola and the error of estimation becomes too high for practical purposes. To obtain accurate values, it is necessary to choose the position of photodetector carefully.

The correctness of the measurement procedure can be verified in the pure nitrogen even without any calculation. The reaction time is sufficient if (i) dark point exists, i.e. both NO^* and NO_2^* intensities are zero and/or (ii) NO^* curve is parabola and/or (iii) after the dark point NO_2^* increases linearly. In other cases more careful approach is necessary and reaction time should be increased. We successfully deployed the method of simultaneous [N] and [O] measurement in the plasma afterglow based on a titration by nitrogen oxide. It consists of fitting the NO^* intensities for increasing NO flow by a theoretical curve. We found that the calculated values and trends are in very good agreement with the results of other methods like EPR or OES. The measured steep increase of nitrogen dissociation, when small oxygen admixture is added, was observed also by other authors. Up to now, the full explanation of this phenomenon is not available. Therefore this relatively cheap and simple absolute method, which is sensitive enough even for low oxygen atom densities, can help to understanding of complex processes involved.

Chapter 7

Summary

The main subject of this thesis is the study of two IPVD techniques - microwave assisted PVD and high power pulsed PVD operating with a preionization.

The microwave assisted PVD reactor consists of a titanium magnetron cathode excited by a direct current and two microwave coaxial antennas located perpendicularly to the magnetron substrate holder axis. While a sputtered particle difusses toward the substrate, it can be ionized anywhere between the magnetron cathode and the substrate. In this case, it is suitable to perform the spatially resolved plasma diagnostics. The main diagnostics method was modified absorption spectroscopy which permitted to obtain simultaneously the spatial evolution of titanium atom temperature and the spatial evolutions of titanium ground state atom, metastable atom and ion densities. An increase of ionization degree by factor 4 near the substrate and an increase of ion flux to the substrate by factor 30 was observed, when microwaves were turned on. The total flux of sputtered particles was independent on applied microwave power. Titanium temperature was found a key parameter to explain the titanium densities evolution. The titanium ground state atom density decreases in microwave area mainly due to gas heating. Titanium metastable atom and ion densities are almost independent on applied microwave power, probably due to creation processes (electron impact and Penning ionization) which balance losses induced by gas heating. The increase of ionization degree near the substrate is due to a decrease in titanium ground state atom density keeping the titanium ion density almost unchanged. Furthermore, the knowledge of the temperature variation allowed us to understand the evolution of argon emission intensity. This effect can be explained by the cooling of the gas on the substrate holder, which increases the local argon density. Both, argon and titanium ground state densities are governed by the heating and by the cooling of the buffer gas. For small magnetron cathodes, inductively coupled RF plasma increases ionization degree of sputtered particles more than the microwave plasma. The advantage of using the microwave coaxial antennas as a plasma source is

that it allows to support long industrial magnetron cathodes by the additional and homogeneous plasma, which is impossible to deal with usually used RF coil.

We advanced currently used high power pulsed magnetron sputtering technique by using a low current DC preionization to significantly reduce the breakdown delay and to accelerate the discharge dynamics. This preionization maintains stable low magnetron current before each high power pulse. It provides very good process stability and reproductibility. The preionization current comes from a stable, low density plasma near the magnetron cathode. It ensures a plasma sheath already establish before each high power pulse. When high voltage is applied, high power pulsed operation is reached only in few μs. It allows to adapt the pulse duration in order to avoid an arc formation even at extremely high cathode load. The average power set by repetition frequency is kept in a value compatible with classical DC magnetron device. The high cathode load in pulse regime was accompanied by the presence of spectral lines of two times ionized copper atoms indicating very high ionization degree of sputtered particles. Time resolved studies show very fast transition to stable self-sputtering regime which can be attended within few μs. This transition starts with fast cooling of electrons by a huge amount of sputtered atoms, which negatively affect Ar ionization in favour of copper ionization. Moreover, gas rarefaction accelerates this transition too. It was shown, that an arc free self sputtering at extremely high cathode load is possible to maintain. The high current density operation met in our case could partially de-confine the magnetized plasma, enhances plasma expansion providing high ion current density onto the substrate. The first results of trench filling using described preionized process make it promising for industrial thin film deposition.

We have improved currently used NO titration method in order to obtain simultaneous N and O atom density in $N_2 - O_2$ post discharges from NO β radiation. This method is based on a fitting of measured data points by a parabolic curve. From fitted parameters of the parabola, the N and O density can by estimated without any calibration. To obtain accurate values, it is necessary to choose the position of a photo detector carefully. There is a wide range of reaction times, where this method gives accurate values, as was shown by comparing it with EPR and optical emission spectroscopy results.

Bibliography

[1] W. R. Grove, *Phil. Trans. R. Soc.* **142** (1852) 87

[2] R. A. Powell, S. M. Rossnagel: *PVD for Microelectronics: Sputter Deposition Applied to Semiconductor Manufacturing*, Boston: Accademic Press, Boston, 1998

[3] P. J. Kelly, R. D. Arnell, *Vacuum* **56** (2000) 159

[4] J. Hopwood, *Physics of plasma* **5 (5)** (1998) 1624

[5] W. M. Posadowski, Z. J. Radzimski, *J. Vac. Sci. Technol. A* **11 (6)** (1993) 2980

[6] D. W. Hoffman, *J. Vac. Sci. Tech. A* **12** (1984) 953

[7] B. Window, *J. Vac. Sci. Tech. A* **11** (1993) 1522

[8] R. S. Robinson, *J. Vac. Sci. Tech.* **16** (1979) 185

[9] J. Lu and M. Kushner, internet site
`http://uigelz.ece.uiuc.edu/pub/presentations/`
`jlu_avs99.pdf`

[10] D. W. Hoffman, *J. Vac. Sci. Tech. A* **6** (1988) 19

[11] W. D. Sproul, P. J. Rudnick, C. A. Gogol and R. A. Mueller, *Surf. Coat. Technol.* **39/40** (1989) 499

[12] P. J. Kelly, R. D. Arnell, *Surf. Coat. Technol.* **97** (1997) 595

[13] J. Hopwood, internet site
`http://www.ece.neu.edu/edsnu/hopwood/ipvd-fig.html`

[14] M. Dickson, J. Hopwood, *J. Vac. Sci. Technol. A* **15(4)** (1997) 2307

[15] J. Hopwood, internet site
     `http://www.ece.neu.edu/edsnu/hopwood/ipvd-lab.html`

[16] M. Rossnagel, J. Hopwood, *J. Vac. Sci. Technol. B* **12** (1994) 449

[17] I. Safi, *Surf. Coat. Technol.* **127 (2/3)** (2000) 203

[18] V. Kouznetsov, K. Macak, J. M. Schneider, U. Helmerson, I. Petrov, *Surf. Coat. Technol.* **122** (1999) 290

[19] J. Vlček, A. D. Pajdarová, J. Musil, *Contrib. Plasma Phys.* **44 (5/6)** (2004) 426

[20] M. Moisan, Z. Zakrzewski, *J. Phys. D: Appl. Phys.* **24** (1991) 1025

[21] O. Leroy, L. de Poucques, C. Boisse-Laporte, M. Ganciu, L. Teulé-Gay, M. Touzeau *J. Vac. Sci. Technol. A* **22(1)** (2004) 192

[22] A. C. G. Mitchell, M. W. Zemanski: *Resonance radiation and excited atoms*, Cambridge University Press, Cambridge, 1934

[23] S.Gurlui, L. De Poucques, O. Leroy, C. Boisse-Laporte, M. Touzeau, *Proceedings of 16th ISPC* (2003)

[24] A. Ricard: *Reactive plasmas* SFV Paris 1996.

[25] R. d'Agostino, V. Calaprio, F. Cramarrosa, *Plasma Chem. and Plasma Process.* **1** (1984) 365

[26] C. Fourrier, *Thesis*, Universite de Nantes, 1981

[27] J. Lu, M. J. Kushner, *J. Appl. Phys* **87(10)** (2000) 7198

[28] S. Konstantinidis, A. Ricard, M. Ganciu, J. P. Dauchot, C. Ranea, M. Hecq *J. Appl. Phys* **95(5)** (2004) 2900

[29] Y. Yamamura, H. Tawara, *Atomic Data and Nuclear Tables* **62(2)** (1996) 150

[30] M. Yamashita, Y. Setsuhara, S. Miyake, M. Kumagai, T. Shoji, J. Musil, *Jpn. J. Appl. Phys.* **38** (1999) 4291

[31] J. E. Foster, W. Wang, A. E. Wendt, J. Brooshe, *J. Vac. Sci. Technol. B* **16(2)** (1998) 532

[32] K. Macak, V. Kouznetsov, J. Schneider, U. Helmerson, I. Petrov, *J. Vac. Sci. Technol. A* **18(4)** (2000) 1533

[33] J. Bohlmark, U. Helmersson, M. VanZeelend, I. Axnas, J. Alami, N. Brenning, *Plasma Source Sci. Technol.* **13(4)** (2004) 654

[34] A. P. Ehiasarian, W. D. Munz, L. Hultman, U. Helmersson, I Petrov, *Surf. Coat. Technol.* **163** (2005) 267

[35] C. Nouvellon, S. Konstantinidis, J. P. Dauchot, M. Wautelet, P. Y. Jouan, A. Ricard, M. Hecq, *J. Appl. Phys.* **92(1)** (2002) 32

[36] S. M. Rossnagel, *J. Vac. Sci. Technol. A* **6** (1998) 19

[37] R. Kukla, T. Krug., R. Ludwig, K. Wilmes, *Vacuum* **41** (1990) 1968

[38] W. M. Posadowski, *Vacuum* **46** (1995) 1017

[39] A. Anders, *Surf. Coat. Technol.* **183** (2004) 301

[40] D. J. Christie, *J. Vac. Sci. Technol. A* **23(2)** (2005) 330

[41] J. A. Bittencourt: *Fundamentals of plasma physics*, Pergamon Press, Oxford, 1986

[42] J. Lu, M. J. Kuschner, *J. Vac. Sci. Technol. A* **19(5)** (2001) 2652

[43] R. A. Young, R. L. Sharpless, R. Stringham, *J. Chem. Phys.* **40** (1964) 117

[44] A. R. De Souza , C. M. Mahlmann , J. L. Muzarl, C. V. Speller, *J. Phys. D: Appl. Phys.* **26** (1993) 2164

[45] A. Granier , D. Chereau , K. Henda , R. Safari, P. Leprince, *J. Appl. Phys.* **75(1)** (1994) 104

[46] V. Zvoníček, *Thesis,* Masaryk University in Brno, 1997

[47] G. Cartry, *Thesis*, Universite Paris Sud, 1999

[48] A. Repsilber, M. Baeva, J. Uhlenbusch, *Plasma Sources Sci. Technol.* **13** (2004) 58

[49] J. T. Herron , J. L. Franklin , P. Bradt, V. H. Dibeler, *J. Chem. Phys.* **30** (1959) 879

[50] P. Harteck, R.R. Reeves, G. Mannela, *J. Chem. Phys.* **29** (1958) 608

[51] S. Krongelb, M. W. P. Strandberg, *J. Chem. Phys.* **31** (1959) 1196

[52] A. A. Westenberg, N. De Haas, *J. Chem. Phys.* **40** (1964) 3087

[53] A. Ricard, A. Moisan and S. Moreau, *J. Phys. D: Appl. Phys* **34** (2001) 1203

[54] A. Ricard, M. Gaillard, V. Monna, A. Vesel, A. Mozetic, *Surf. Coat. Technol.* **142-144** (2001) 333

[55] A. Ricard, V. Monna, M. Mozetic, *Surf. Coat. Technol.* **174/175** (2003) 905

[56] J. Nahorny J, C. M. Ferreira, B. Gordiets, D. Pagnon, M. Touzeau, M. Vialle, *J. Phys. D: Appl. Phys* **28** (1995) 738

[57] V. Kudrle, A. Tálský, A. Kudláč, V. Křápek and J. Janča, *Czech. J. Phys.* **50-D** (2000) 305

[58] C. D. Pintassilgo, J. Loureiro, V. Guerra, *J. Phys. D: Appl. Phys.* **38** (2005) 417

[59] J. Loureiro, P. A. Sá, V. Guerra, *J. Phys. D: Appl. Phys.* **34** (2001) 1769

[60] P. Soupiot, O. Dessaux, P. Goudmand, *J. Phys. D: Appl. Phys.* **28** (1995) 1826

[61] I. A. Kossyi, A. Yu. Kostinsky, A. A. Matveyev, V. P. Silakoc, *Plasma Sources Sci. Technol.* **1** (2002) 207

[62] M. Capitelli, C. M. Ferreira, B. F. Gordiets, A. I. Osipov: *Plasma kinetics in atmospheric gases*, Springer, 2000

[63] A. N. Wright, C. A. Winkler: *Active nitrogen* (New York: Academic Press), New York, 1968

[64] C. B. Kretschmer, H. L. Peterson, *J. Chem. Phys.* **39** (1963) 1772

[65] A. Fontijn, C.B. Meyer, H. I. Schiff, *J. Chem. Phys.* **40** (1964) 64

[66] L. G. Piper, L. M. Cowles and W. T. Rawling, J. Chem. Phys., 85(6), 3369, 1986

[67] R. W. B. Pearse and A. G. Gaydon: *The identification of molecular spectra*, Chapman and Hall Ltd., London, 1950

[68] T. Belmonte, T. Czerwiec, A. Ricard, H. Michel, *Proceedings of XXIII ICPIG* (1997)

[69] A. A. Westenberg, *Prog. React. Kinet.* **7** (1973) 23

[70] B. Gordiets, C. M. Ferreira, J. Nahorny, D. Pagnon, M. Touzeau, M. Vialle, *J. Phys. D: Appl. Phys.* **29** (1996) 1021

[71] K. M. Evenson, D. S. Burch, *J. Chem. Phys.* **45** (1966) 2450

[72] V. Kudrle, P. Vašina, A. Tálský, J. Janča, *Proceedings of ESCAMPIG 16* (2002)

Curriculum Vitae

1979	born in Brno, Czech Republic
1997 – 2002	study at Masaryk University in Brno
1999	invited by Assoc. Prof. A. Tálský to participate at the research activity of Department of Physical Electronics
2001	3 months stay in LPGP in the group of Dr. C. Boisse-Laporte
2002	Master degree in Physics, Masaryk University in Brno master thesis: Study of elementary processes in pulsed excited microwave discharge
2002 – 2005	PhD student Masaryk University in Brno & Université Paris - Sud, Orsay thesis: Plasma diagnostics focused on new magnetron sputtering devices for thin film deposition
2003	awarded by Director of Physical Section of Masaryk University in Brno for creative attitude in scientific research

Related Publications

Reduction of transient regime in fast preionized high power pulsed magnetron discharge
P. Vašina, M. Meško, M. Ganciu, J. Bretagne, C. Boisse-Laporte, L. de Poucques, M. Touzeau
Europhysics Letters **72(3)** (2005) 390

Spectroscopic analysis of a pulsed magnetron discharge
P. Vašina, M. Meško, J. C. Imbert, L. de Poucques, L. Teule-Gay,
C. Boisse-Laporte, J. Bretagne, D. Pagnon, M.Touzeau, M. Ganciu
Journal of Optoelectronics and Advanced Materials **7(5)** (2005) 2421

Preionised pulsed magnetron discharges for ionised physical vapour deposition
M. Ganciu, S. Konstantinidis, Y. Paint, J.P.Dauchot, M. Hecq, L. de Poucques,
P. Vašina, M. Meško, J.C. Imbert, J. Bretagne, M.Touzeau
Journal of Optoelectronics and Advanced Materials **7(5)** (2005) 2481

Comparison of the ionization efficiency in a microwave and a radio-frequency assisted magnetron discharge
L. de Poucques, J.-C. Imbert, P. Vašina, C. Boisse-Laporte, L. Teulé-Gay,
J. Bretagne, M. Touzeau
Plasma Sources Science and Technology **14(2)** (2005) 321

Spatial characterization of an IPVD reactor: neutral gas temperature and interpretation of optical spectroscopy measurements
L. de Poucques, J.-C. Imbert, C. Boisse-Laporte, P. Vašina, J. Bretagne,
L. Teulé-Gay, M. Touzeau
Surface & Coating Technology **200** (2005) 800

Theoretical study of pulsed microwave discharge in nitrogen
Z. Bonaventura, D. Trunec, M. Meško, P. Vašina, V. Kudrle
Plasma Sources Science and Technology **14** (2005) 751

Simultaneous measurement of N and O densities in plasma afterglow by means of NO titration
P. Vašina, V. Kudrle, A. Tálský, P. Botoš, M. Mrázková, M. Meško
Plasma Sources Science and Technology **13(4)** (2004) 668

Electron density measurements in afterglow of high power pulsed microwave discharge
M. Meško, Z. Bonaventura, P. Vašina, A. Tálský, Z. Frgala, V. Kudrle, J. Janča
Plasma Sources Science and Technology **13(4)** (2004) 562

Measurement of concentration of N atoms in afterglow
V. Kudrle, P. Vašina, A. Tálský, J. Janča
Czechoslovac Journal of Physics **52-D** (2002) 589